Performance of the High Level Trigger γ-conversion reconstruction chain in the ALICE central tracking detectors

Master Thesis in Experimental Nuclear Physics

by
Thomas Christopher Solem

Department of Physics and Technology
University of Bergen

June 2011

Acknowledgements

There are many people who contributed, both indirectly and directly, to the completion of this thesis. First, I would like to thank my supervisor Dieter Rörich for the encouragement and opportunity to do this work, and for all his help and guidance throughout these past years.

I owe a great deal of thanks to Kalliopi Kanaki, who helped me on countless occasions, with everything from physics and presentations, to my many Aliroot related misconceptions and software issues. I could not have done this without your help. In the same vain, I would also like to thank Kenneth Aamodt and Matthias Richter, who's input and assistance has been invaluable. Thank you all for your help, guidance, and of course your patience.

I would also like to thank Artur, Eivind, Andreas, Per Ivar, Øystein D., Øystein H., Hege, Camilla, Christian, Boris, Dana, Henrik, Timur, Martin, Are, and everyone else in the Heavy-Ion group at Bergen.

I would like to thank my family for all the encouragement and support they've given me throughout my life. Thank you also for helping me maintain my pursuits on the occasional overwhelming days. And thank you to my friends, especially Lars Ole, Teo, Jhon, and Eirik.

Last, and most certainly not least, I would like thank the love of my life Lisa Samnøy, and our beautiful daughter Sienna. Thank you, Lisa, for your infinite understanding and support throughout this process. Thank you for working all the long hours and extra shifts so I could focus on my work. And Sienna, thank you for being the most perfect daughter a father could ever ask for. You have been a constant source of motivation.

A humble apology to everyone I have forgotten to thank, I did not do so intentionally.

Abstract

Photons are produced through various processes in the particle and nuclei collisions at the LHC, and pose as useful probes of the formation of a Qaurk-Gluon Plasma. The probability of a photon converting within the central tracking detectors of ALICE has been found to be approximately 8–9 % [53]. The thesis explores the performance of the photon reconstruction through the conversion method, for the High Level Trigger using the central tracking detectors of ALICE.

The photon reconstruction method through its conversion will compliment the photon detection performed by the calorimeters. However, due to the large acceptance of the central tracking detectors, the method has proved equally beneficial through the off-line event reconstruction, even though the conversion probability is low. It has therefore been a goal to map the potential performance of an on-line reconstruction of the photons through the conversion method.

The performance of the photon reconstruction has been analyzed through the simulation, and subsequent High Level Trigger reconstruction, of highly contrived events and minimum bias p-p collisions at $\sqrt{s} = 14\ TeV$ per nucleon pair. The events were embedded with additional γs in the central pseudo-rapidity range to provide higher statistics.

The analysis led to the optimization and further development of the existing code in the High Level Trigger, dedicated to the on-line reconstruction of neutral particles through the detection of their decay products. An overview of the reconstruction algorithm and potential future upgrades is provided. The results obtained for the simulated data is presented along side the optimal off-line results. The final results obtained for the γ embedded minimum bias p-p collisions for the on-line reconstruction, yielded an average photon conversion reconstruction efficiency of 41.7 %, with an average purity of the reconstructed sample of 74.2 %.

Contents

List of Figures

List of Tables

Chapter 1

Introduction

Nuclear physics is a field of physics which studies the buliding blocks and interactions of atomic nuclei and their constituents. The field began with the discovery of radioactivity by Henri Becquerel in 1886 and has seen a rapid development over the past 100 years. A wide range of topics is covered by nuclear physics, such as Experimental Nuclear Physics, Nuclear Medicine, and Nuclear Energy to name a few. Experimental relativistic nuclear physics is mainly concerned with studying the properties of nuclear matter at high energy densities and temperatures. In essence, this is predominantly done by accelerating and colliding particles and nuclei in either fixed target experiments or collider experiments. This allows for the testing of the physical theories, i.e., the The Standard Model (see section 1.1), and searching for previously unseen effects and phenomena. Advances in accelerator technology has lead to the design and implementation of larger and more energetic accelerators, allowing the collisions of particles and nuclei at higher energies.

1.1 The Standard Model

The Standard Model (SM) is a theoretical model describing the interaction of the elementary particles through the elementary forces of nature, namely the strong, electromagnetic and weak forces (where we have excluded the gravitational force due to its negligible impact). SM is based on Quantum Mechanics and Quantum Field Theory. SM has proven a valuable tool for nuclear and particle physicists as many of its predictions have been verified empirically through experiments. One such experiment discovered the Tau particle in the 1970s at the SLAC National Accelerator Laboratory in Stanford, USA. The electromagnetic and weak forces have been proven to be two different manifestations of the same force, which only becomes visible at high energies. It has been proposed that the strong force may also be merged with the electro-weak force in the duly named Grand-Unifying-Theories (GUTs). The energy where this has been proposed to occur is of the order of 10^{18}

GeV, well beyond the range of any of today's experiments. Two major subdivisions of SM are QED (Quantum Electrodynamics) and QCD (Quantum Chromodynamics). QED describes the interactions between charged particles and photons due to the electromagnetic force, and QCD describes the interactions of color charged particles due to the strong force. One typically divides the elementary particles into fermions and bosons, and they are considered point-like particles, i.e., all of their mass and energy is contained within a single point in space and time.

Fermions

Fermions are half-integer spin particles that obey the Pauli-exclusion principle, i.e., no two fermions may occupy the same state at any given time. In large numbers, fermions are well described by Fermi-Dirac statistics. The fermions are typically divided into two groups, namely leptons and quarks. Each of these groups are further separated into three generations of particles, each containing two different particles along with their respective anti-particles.[1] The first generation refers to the stable particles that in part comprise the matter we see around us. Typically, one may say that particles belonging to higher generations will have larger masses, be more unstable, and have shorter lifetimes than the particles in the generation(s) below. For instance, a particle in the third generation will have a larger mass and a shorter lifetime than a particle belonging to the first generation. Table 1.1 shows the various fundamental particles grouped by generations, though not depicted, all listed particles also have an antiparticle that belongs to the same generation.

	1.Generation	2.Generation	3.Generation
leptons	e, $\bar{\nu}_e$	μ, $\bar{\nu}_\mu$	τ, $\bar{\nu}_\tau$
quarks	u, d	s, c	t, b

Table 1.1: Fundamental particles

The leptons may carry integer value electric charge and may interact through the electro-weak force. The electron, muon, and tau with their respective neutrinos and anti-particles comprise the lepton family. The neutrinos are believed to be almost massless particles (experimentally proven

[1] There are theories that allow for two or four generations but experimental results favor three generations.

to be smaller then 1 eV for the three aforementioned neutrinos) and depict an interesting quality not observed for any of the other particles.[2] The neutrino may oscillate its existence between the different generations, i.e. an electron-neutrino may transform itself into a tau-neutrino or muon-neutrino and vice versa. This is known as neutrino oscillations, and evidence for which has been observed by studying the neutrino spectra originating from the Sun [1].

The quarks carry fractional electric charge and also interact through the electro-weak force. Contrary to the leptons, quarks also carry a color-charge, which allows them to interact through the strong force as well. The quark-family consists of the up, down, strange, charm, top, and bottom(beauty) quarks. The up and down quarks make up the proton and the neutron. The proton is comprised of two up quarks and one down quark, and the neutron of one up quark and two down quarks.

Bosons

The bosons are the force carriers of the elementary forces. The photon is mass-less and carries no electric charge, and mediates the electromagnetic force. The W^-, W^+ and the Z^0 mediate the weak force, with masses of $80.376 \pm 0.033\ GeV/c^2$ and $91.1876 \pm 0.0021\ GeV/c^2$ respectively [2]. The gluon mediates the strong force and is thought to be mass-less or close to mass-less. Gluons carry no electric charge, but they do however carry a color charge. This allows the gluons to interact with the quarks and also with each other.

Compound Systems

Fermions and bosons may combine and form compound systems. For instance two up quarks and one down quark are bound by the strong force and form a nucleon, i.e., the proton. The nucleon may further combine with other nucleons to make up a nucleus, which then in turn can interact and bind with electrons to form an atom.[3] Atoms bind together to form molecules, which makes up everything we see around us.

A compound system may typically be classified as either stable, metastable or unstable. Unstable systems are radioactive and may decay or fragment through a series of different channels. The stability of a system is described by its respective lifetime. Lifetimes observed in nature and experiments show a wide range of values varying over many orders of magnitude. Typically, if a system doesn't exude a measurable level of radioactive emittance, or fission, it will be considered stable.

[2] Theories have shown that there may exist massive neutrinos, but these have never been observed in experiments.

[3] The hydrogen atom only has one nucleon in its nucleus, namely the proton.

Hadrons are compound systems comprised of two or three quarks, namely mesons and baryons. Mesons, which are comprised of a quark and an anti-quark, are typically unstable and short lived compounds. The lightest baryon, the proton, is stable. The neutron, however, is unstable when not bound in a nucleus and has a lifetime of approximately 15 minutes. As was with the aforementioned fermions, compounds consisting of particles from higher generations are generally more unstable than compounds comprised of lower generation particles.

Compound systems consisting of a large number of protons and neutrons exude another form of instability. Due to the Coulomb repulsion between the protons in a nucleus containing a large and equal amount of protons and neutrons, it will be energetically favorable for the proton to decay to a neutron via β-decay. This leads to the fact that the heavy atoms found in nature have a higher ratio of neutrons to protons, than what is observed for the lighter atoms, where the ratio is approximately equal to 1.

1.1.1 Quantum Chromodynamics - QCD

Quantum Chromodynamics (QCD) describes the interaction of the color-charged particles through the interaction of the strong force, namely quarks and gluons. QCD inflicts a series of conditions with respect to the formation of bound systems, one being that all bound systems must be color neutral, also referred to as white. The different color charges are classified as red, blue, and green, and anti-red, anti-blue, and anti-green. In order for a meson to form, one of the quarks must carry the anti-color to the color carried by the other quark, i.e., if one of the quarks of the meson pair has the color red, the other must have the color anti-red. In order for baryons to be color neutral, one quark must be red(anti-red), another must be blue(anti-blue) and the last must be green(anti-green). The term color doesn't mean that the quarks and gluons have a color as we use the term in everyday life, but it was simply chosen to help illustrate the fact that all bound systems of quarks and gluons must be neutral.

The strong force as described by QCD is termed to have a running coupling constant, α_s. This means that the coupling constant is in fact not a constant, but that its strength varies with the energy and the distance between the two interacting particles. The running coupling constant leads to a strong attraction at large distances or low energies, and a weak attraction at high energies and small distances. This leads to two important aspects of QCD, namely asymptotic-freedom and confinement.

Asymptotic freedom , as mentioned, is a consequence of the running coupling constant. As the separation distance between the two particles decreases or their energy increases, the interaction due to the strong force will get weaker. At asymptotic values for the distance and en-

ergy, the quarks and gluons will cease to interact through the strong force entirely, and the system will be governed by the electro-weak interactions.

Confinement is also a consequence of the running coupling constant, but with an opposite notion. At large distances or low energies the coupling grows logarithmically and prevents any quarks and gluons from existing freely in nature, i.e., they are confined in bound states. If one were to pull two quarks apart, their internal energy would increase as the distance between them grew, leading to the creation of another quark-pair between them. If one continued to pull them apart, more quark-antiquark pairs would be created and it's this process that's responsible for the creation of jets in subatomic collisions.

The theory of QCD predicts that at high energy densities and temperatures above ∼170 MeV, hadronic matter will undergo a phase-transition, see figure 1.2. In this new phase, the quarks and gluons will behave as a liquid or plasma of deconfined quarks and gluons. This phase is generally known as the Quark-Gluon-Plasma (QGP). For heavy ion collisions in ALICE the temperature is estimated to reach up to ∼1 GeV, thereby allowing the formation of a QGP.

Interactions occurring at short distances, where the strong coupling constant is sufficiently weak may be described by perturbative QCD (pQCD), such as the initial hard scattering of colliding partons. However, due to the running coupling constant, pQCD breaks down for interactions at large distances and finite temperatures, where we define large distances to be of the order of fm/c and above. It is therefore not a viable approach in the description of a QGP, and in response, an analytical approach has been developed known as lattice QCD. In this approach the quarks may only inhabit discrete positions in a space-time lattice, as opposed to the continuum description in pQCD. The quarks are bound via gluons aligned with the lattice links, analogous to that of atoms in a crystal lattice known from solid state physics, see figure 1.1.

1.1.2 Quark-Gluon-Plasma

In heavy ion collisions, as that of ALICE, one may divide a collision into different stages. One has the initial-hard-partonic stage, where the interactions are typically governed by the hard scattering of the quarks and gluons in the colliding nuclei. The initial-hard-partonic stage is followed by the formation and thermalisation of the QGP, where the energy densities and temperatures are high enough that the wave functions of the quarks and gluons overlap with each other, thereby deconfining the quarks and gluons from their original nucleon and allowing them to roam the medium. The thermalised QGP is followed by a rapid expansion and cooling of the medium, resulting in the

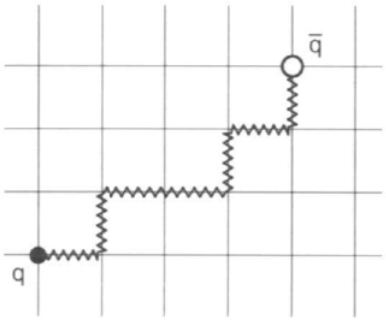

Figure 1.1: Schematic illustration of lattice QCD depicting the discretization of the space-time distribution of the quarks and gluons. The figure was taken from [3].

recombination of quarks and gluons into bound states (mesons, baryons). This is known as the hadronic-gas stage. Finally, the energy density and the temperature is low enough that the inelastic and elastic collisions cease, due to their low cross sections. This is known as the freeze-out stage. In the freeze-out stage, the interactions are typically dominated by nuclear decays, such as the decay of a π^0 to two γs.

In cosmology the theory of the Big Bang states that the universe started with all its energy confined to a singularity in space and time, followed by a rapid expansion and cooling. If this is the case, then one would expect the energy density and the temperature to be high enough for a QGP to be present at the early stages of the expansion. It's been estimated the universe was in state of QGP in the early phases after the Big Bang when the temperature and energy density was sufficiently large. It's thought that universe underwent a QCD phase transition from a QGP at a temperature $T_{QCD} \approx 170\ MeV$ corresponding to a time $t \approx 10^{-5}$–$10^{-4}s$ after the Big Bang [3]. Neutron stars are also believed to house a form of cold quark matter in their core. Under the gravitational force of such a dense star, the pressure in the center should be high enough for the QGP to form, see figure 1.2. By creating a QGP in an experiment, such as ALICE, one may essentially recreate some of the initial conditions in the formation of the universe. Thereby gaining further insight into the elementary forces and processes that governed the early formation of the universe and matter as we know it today.

1.2 Probing the QGP

A QGP's high temperature and energy density leads to the deconfinement of the quarks and gluons within the medium. The interactions of the quarks and gluons inside the QGP are governed by their quark and gluon distri-

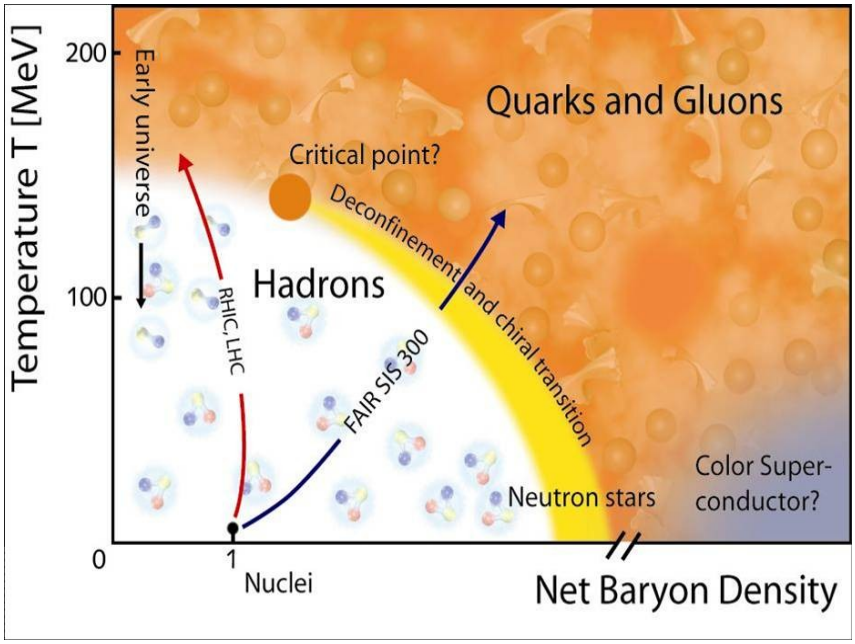

Figure 1.2: Schematic diagram showing the phase transition of nuclear matter as a function of density and temperature. The figure was taken from [4].

butions. A variety of different effects may be used to probe the existence of a QGP, such as the flow in non-central collisions, jet-suppression, direct-photons, and di-lepton emission to name a few. This section will present a few of them, and list the results obtained with these methods in heavy ion experiments. The motivation and results for the direct photon method of probing the QGP will be discussed in chapter 2.

Mainly the results obtained from the RHIC collider will be presented in the present section, along with a few results from the ALICE experiment operating in conjunction with the LHC. A description of the LHC and the ALICE experiment will be given in chapter 3.

The Relativistic Heavy Ion Collider (RHIC) at the Brookhaven National Laboratory (BNL) started colliding gold ions in the year 2000 and is still in operation as of this writing. RHIC inhabits a tunnel of 3.8 km circumference and embodies six collision detectors. Four of them were dedicated to the investigation of the medium formed in heavy ion collisions, namely the PHENIX, PHOBOS, STAR and BRAHMS experiments. The goal of the experiment is to probe the the existence and characteristics of the strongly interacting medium formed in ultra-relativistic heavy ion collisions, the aforementioned QGP.

In addition to colliding gold, the experiment also collides p-p, d-Au, and Cu-Cu. RHIC collides Au-Au and p-p with a maximum center of mass en-

ergy of 200 GeV per nucleon pair and 500 GeV per nucleon pair respectively, and operates at a nominal luminosity of $2 \times 10^{26} cm^{-2} s^{-1}$ for Au-Au [5]. A vast amount of information has been extracted from the recorded data and a few of the key results will be presented below.

Azimuthal flow coefficient - v_2

In ultra-relativistic heavy ion collisions, the nuclear matter is compressed in the early stages of an collision. If there are processes with large cross sections in this compressed medium, the density gradients will translate into an outward pressure resulting in a velocity boost of the particles in the medium. This effect is often collectively termed *flow*. The stronger the interactions in the medium are, the greater this translation is expected to be.

For non-central collisions the overlapping region of the colliding nuclei has the shape of an ellipsoid, reminiscent of an almond. This spatial azimuthal anisotropy will translate into a momentum anisotropy of the particles emerging from the almond shaped region. The largest boost is given in the direction parallel to the interaction plane, where the interaction plane is defined as the plane formed by the beam axis and its perpendicular vector parallel to the impact parameter of the colliding nuclei. The azimuthal distribution of the particles may be expressed through a Fourier decomposition given by [5] as (1.1), where we note that the v_2 coefficient represents the flow in the interaction plane, often termed the elliptic flow, and where N is the particle yield, p_t the transverse momentum, y the rapidity, b the impact parameter of the colliding nuclei, and ϕ is the angle between the particle and the reaction plane.

$$\frac{dN}{p_t dp_t dy d\phi\,(p_t, y, \phi; b)} = \frac{dN}{p_t dp_t dy}\left[1 + 2v_2\,(p_T, y; b)\,cos\,(2\phi) + \cdots\right]. \quad (1.1)$$

The geometric azimuthal anisotropy is short lived in non-central collisions. Since the particles closer to the interaction plane receive a larger velocity boost the medium will expand more rapidly in the direction parallel to the interaction plane than it will in the perpendicular direction. This will limit the lifetime of a geometrical azimuthal anisotropy as the flow of the medium will steer it towards an isotropic distribution. Therefore a large contribution to the flow must be generated in the early interactions of the collision, typically, within 2 fm/c [5]. The momentum anisotropy is, however, preserved throughout the evolution of the collision and may be observed in the end state azimuthal hadron distributions.

RHIC, colliding gold ions at a center of mass energy (C.M.) of 200 GeV per nucleon pair, observed that the elliptic flow reached a maximum of 0.2 near a transverse momentum of 3 GeV/c, see figure 1.3. The ALICE

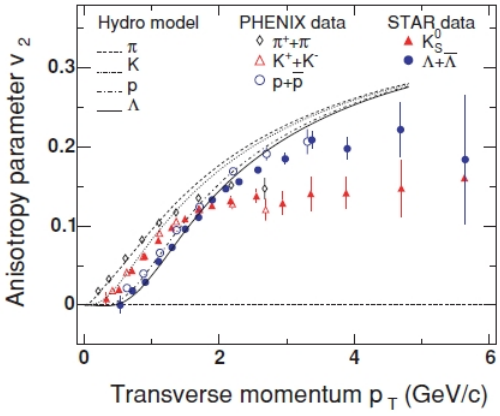

Figure 1.3: v_2 measurements plotted as a function of p_t from minimum bias Au-Au collisions with a center of mass energy of 200 GeV per nucleon pair. The dashed lines indicate the expected values from hydrodynamic calculations for different particle species. The shapes depict the results observed with the STAR and PHENIX detectors at RHIC. The figure was taken from [5].

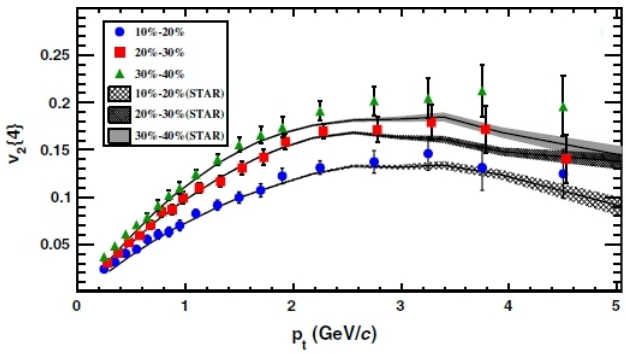

Figure 1.4: ALICE measurement of $v_2\{4\}$ as function of p_t from Pb-Pb collisions at $\sqrt{s_{NN}} = 2.76\ TeV$ per nucleon pair, shown for 40–50 % centrality. The v_2 was determined using a 4-particle cumulant method and is denoted $v_2\{4\}$. The $v_2\{4\}$ measurement from STAR at $\sqrt{s_{NN}} = 200\ GeV$ for the same centrality is shown for comparison. The figure was taken from [6].

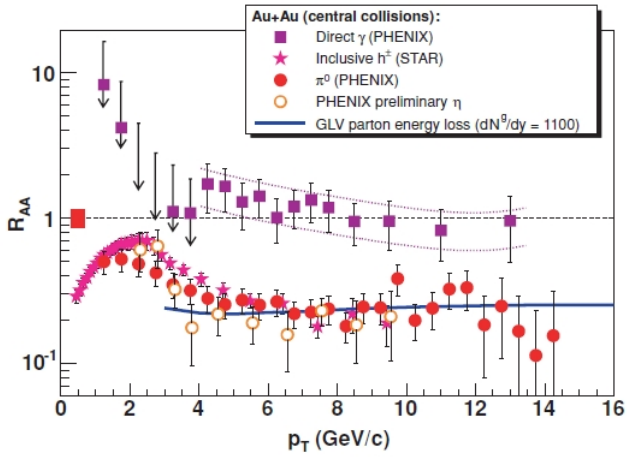

Figure 1.5: R_{AA} for γs, πs, and ηs plotted as a function of their transverse momentum. The πs and ηs indicate a suppression of a factor 5 for $p_t > 4\ GeV/c$. For γs the $R_{AA} \approx 1$, indicating that the γs are unaffected by the strongly interacting medium. The figure was taken from [5].

experiment at the LHC started colliding Pb-Pb with a C.M. of 2.76 TeV per nucleon pair in 2010, and observed an elliptic flow 30 % larger than that observed at RHIC. Previous estimates predicted an enhancement of the elliptic flow in the range of 10-30 % for LHC relative to RHIC, depending on the different hydrodynamic models used in the calculation, see figure 1.4. [6]

Jet suppression and the nuclear modification factor R_{AA}

The experiments at RHIC observed another feature previously unseen in other collision experiments, namely the suppression of high p_t hadrons emerging from the collision. Since the incident parton flux is larger in Au-Au than in p-p, one would expect that the relative yields would scale as the ratio of the incident parton flux of the two colliding nuclei for Au-Au and p-p. This is known as binary collision scaling. However, RHIC observed that the hadronic yield from Au-Au was approximately 5 times lower than one would expect if one only considered the binary collision scaling of the measured p-p yields [5]. This is shown in figure 1.5 and is known as the nuclear modification factor R_{AA}.

ALICE also measured a significant suppression at high p_t, however, they observed a higher rate of suppression at $p_t = 6$–$7\ GeV/c$ indicating that the medium formed at the LHC was denser than that formed and observed at the RHIC collider [7]. ALICE measured the suppression factor at different centralities and noted that for less central events the nuclear modification factor approaches the value 1. The higher rate of suppression could re-

flect that the medium formed at LHC is denser than that formed at RHIC, however, it could also be due to different initial conditions. Until the data from the future p-A collisions at the LHC is analyzed, one cannot with certainty tell whether the increased suppression is due to the formation of a denser medium or not. This strongly suggests that the suppression is due to the partons interactions with the medium, as the density of the medium is expected to scale with the centrality of the collision. See figure 1.6 for the measured R_{AA} at ALICE from Pb-Pb collisions at $\sqrt{s} = 2.76\ TeV$ per nucleon pair.

The hadronic suppression is clearly visible if one plots the azimuthal momentum distribution of back-to-back jets for Au-Au and p-p, see figure 1.7. In p-p collisions the particles show no signs of suppression since the parton densities aren't high enough to form an extended, strongly interacting medium. In Au-Au however, the densities are high enough for a QGP to form, and the particles traversing this medium will scatter off its constituents and experience an energy loss. This is why there is no signal at $\phi = \pi$ for the Au-Au distribution. It was also shown that if one were to substantially lower the p_t threshold the signal would be retrieved, but the average momentum around $\phi = \pi$ would be significantly lower and distributed nearly isotropically in the lower hemisphere of the azimuthal distribution [5].

Enhanced strange particle production

It has been proposed that an enhanced production of strangeness may indicate the formation of a QGP in heavy ion collisions. There is a large amount of $q\bar{q}$ pairs produced in these collisions, where the production of the heavy flavors are suppressed due to their large masses. Typically, one would expect a relative yield of 10–20 % for $s\bar{s}$ compared to the yields of $u\bar{u}$ and $d\bar{d}$ [3]. However, at approximate temperatures corresponding to 200 MeV, the production of additional strange particles becomes possible through the gluon-fusion process, namely $gg \rightarrow s\bar{s}$. Therefore, an enhanced yield in the strange and multi-strange particle spectra may indicate that the characteristics of the medium formed in the collision are compliant with that of a QGP.

An enhancement of the yields in strange particle production was observed at RHIC while colliding Au-Au at a C.M. of 200 GeV per nucleon pair. A measurement of the relative yields for Au-Au with respect to p-p signaled an enhancement in the Ξ^- production rate of up to to a factor $\sim$7–10, see figure 1.8 [8].

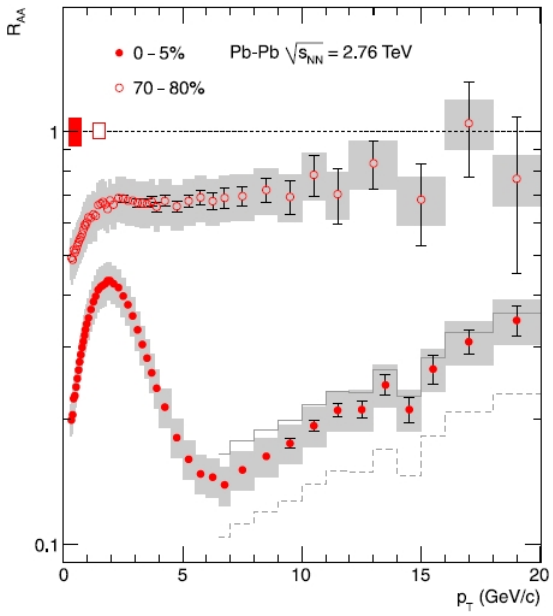

Figure 1.6: ALICE measurement of R_{AA} for charged particles plotted as a function of their transverse momentum, from Pb-Pb collisions at $\sqrt{s} = 2.76$ TeV per nucleon pair. At a $p_t = 6$–7 GeV/c, ALICE measured a lower value compared to RHIC, indicating that the medium formed at ALICE could be denser than that formed at RHIC. The figure was taken from [7].

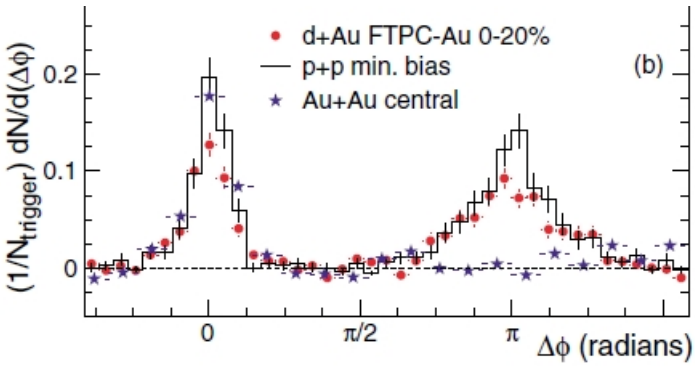

Figure 1.7: Back-to-back correlated jets plotted as a function of ϕ. In p-p and d-Au the peak at $\phi = \pi$ is clearly visible, where as in Au-Au there is no substantial signal at $\phi = \pi$. This indicates that the medium formed in heavy ion collisions at RHIC (Au-Au) was in fact a strongly interacting medium. The figure was adapted from [9].

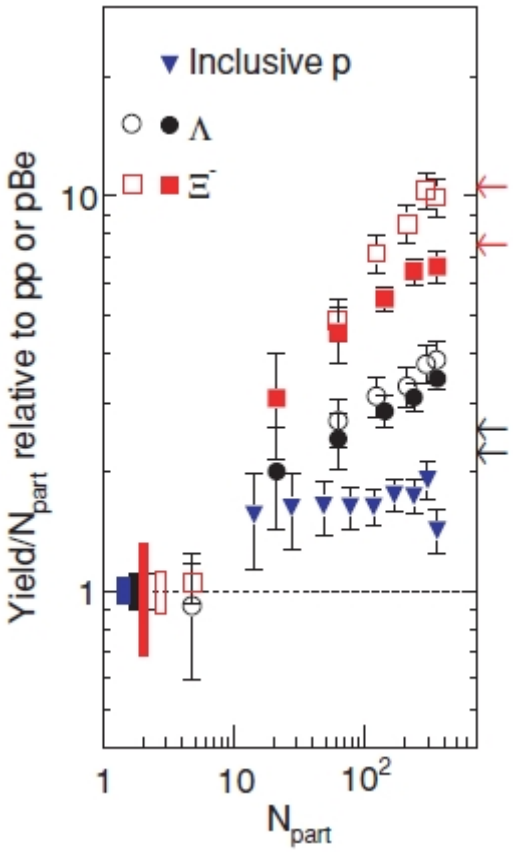

Figure 1.8: The figure shows the yields for the strange particles produced at RHIC from colliding ions (A-A), with respect to binary scaling (from p-p or p-Be) and plotted against number of collision participants $\langle N_{part} \rangle$. Solid shapes represent Au-Au collisions at $\sqrt{S_{NN}} = 200\ GeV$, and open shapes represent Pb-Pb collisions at $\sqrt{S_{NN}} = 17.3\ GeV$. The figure was adapted from [8].

Chapter 2

Photon physics

2.1 Probing the QGP - Direct photons

Using photons to probe the formation and existence of the QGP was proposed already in 1976 by Feinberg [10]. Photons carry no color charge and will therefore not interact strongly with the medium formed in a collision. The typical interaction length of a photon is larger then the size of the fireball formed in a collision, and may therefore escape the medium nearly unscathed. In addition, photons are emitted throughout the different stages of the collision process, such as the initial-hard-partonic scattering, thermalised QGP, hadronic gas, and freeze-out stage. By detecting the emitted photons, one may then follow the evolution of the collision and extract valuable information about the characteristics, and processes, that underwent during the collision and the possible formation of a QGP. By deciphering these photons and determining the produced spectra from the various processes and stages, one may use this information to determine if in fact a QGP was formed in the collision.

Apart from the hadronic decays, there are three main process that will lead to the emission of a photon in a heavy ion collision. The processes are the Compton-like scattering of a gluon off a quark, the annihilation of a quark and antiquark, and the bremsstrahlung radiation from a quark passing through the medium. The Feynman diagrams for the Compton-like scattering and annihilation processes are depicted in figure 2.1. All three process contribute to the inclusive photon spectra originating from the different stages of the collision, apart form the freeze-out stage where the spectra is dominated by the hadronic decays.

As mentioned above, direct photons may originate from a variety of sources and one needs to further classify them. Typically, one defines direct photons to include all photons that originate from primary processes, namely all photons that don't come from hadronic decays such as that of π^0s. Direct photons may be further classified as either thermal or prompt.

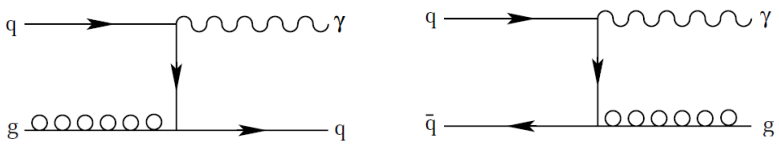

(a) Compton scattering of a qluon off a quark.

(b) Annihilation of a quark and an antiquark.

Figure 2.1: Figure showing two of the diagrams resulting in a photon from Compton scattering and annihilation. Though not explicitly depicted, the same processes are valid for the quark's and qluon's respective antiparticles. The figures were obtained from [11].

- **Thermal photons** entail those originating from the thermalised QGP or the hadronic gas stage. In Pb-Pb collisions at the LHC, both of these stages are proposed to have sufficient lifetimes for the medium to reach thermal equilibrium. Upon reaching equilibrium the system will have lost all knowledge of the initial conditions of the colliding nuclei, and the quark and qluon distributions will be governed by the temperature and energy density of the system, described by the equation of state (EOS). However, since the cross sections of the photon emissions are directly dependent on the quark and gluon distributions, the photons are termed thermal when originating from a thermalised medium.

- **Prompt photons** represent those which come from an immediate interaction, such as those from the hard partonic scattering in the initial stage of a collision. The processes that lead to the photon emissions are the same as those in a QGP and hadronic gas, but in this case the quark and gluon distributions are governed by the energy of the colliding nuclei, due to the gluon saturation described below. Photons from hadronic decays are also often denoted prompt, however, they are not direct.

In ultra-relativistic heavy ion collisions the nuclei will undergo a Lorentz contraction which results in small Bjorken x values. The Bjorken x represents the fraction of momentum carried by the valence quarks, sea quarks, and gluons in the nuclei. It has been shown that the production of gluons will increase substantially as the value of x decreases. At the energies available at the LHC, it has been proposed that the gluon production may be of such an order that the nuclei will be occupied by such a vast amount of gluons, that they will effectively overlap and saturate the colliding nuclei [3]. This configuration is often denoted as the Color Glass Condensate (CGC). If the colliding nuclei are in a state of CGC, it should reveal itself in the initial hard partonic scattering, and may therefore be a candidate to be studied though the prompt photon spectra.

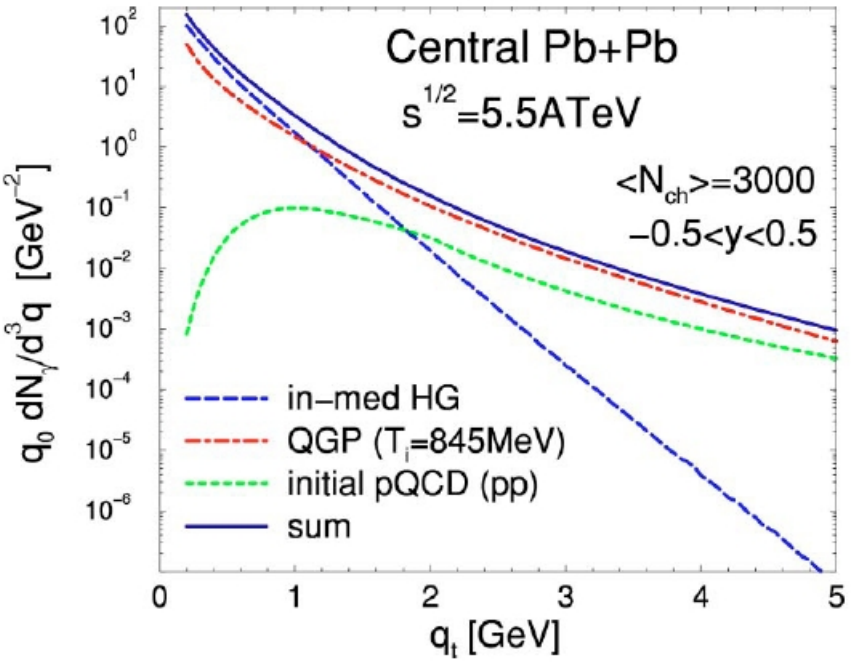

Figure 2.2: The figure shows the anticipated photon spectra from Pb-Pb collisions at $\sqrt{s} = 5.5\ TeV$ per nucleon pair. The figure was taken from [12].

The expected inclusive spectra from direct photons in Pb-Pb collisions with a C.M. of 5.5 TeV per nucleon pair at the LHC, along with the relative prompt and thermal contributions, are shown in figure 2.2. The spectra is clearly dominated by the thermal photons for $p_t < 5\ GeV/c$ and they are expected to contribute up to 10 GeV/c. However, since the thermal and prompt photons are indistinguishable from each other, one can not simply measure the thermal yields directly. Instead, one measures the inclusive photon yield and later subtracts the yields originating from the various background sources. The average inclusive photon yield at the LHC in nominal Pb-Pb collisions is expected to be approximately 50 γs per event [13]. The dominant source of photons arise from the hadronic decays in the freeze-out stage, the most significant being $\pi^0 \rightarrow \gamma\gamma$, accounting for 85–90 % of the yield originating from decay photons (η^0 accounts for 5–10 %) [14]. In addition to the hadronic decays, the resonance decays present in the hadronic gas stage will also contribute to the total yield, for instance $\pi + \rho \rightarrow \pi + \gamma$, all though at a much lesser rate than the π^0 and η^0.

ALICE will collide p-p, p-A, and A-A, and by measuring the inclusive photon spectra from these runs allows one to build up an ensemble of reference spectra. With the reference spectra at hand, one can essentially deter-

mine which part of the measured yield in Pb-Pb originates from the prompt photons and which part is due to the thermal contribution. The reference spectra from collisions with other nuclei are vital for the thermal spectrum extraction. However, the largest source of background, the hadronic decays, may be subtracted by calculating the invariant mass of the mesons and subtracting the calculated background via the *Statistical subtraction technique* resulting in the yield of photons produced from hadronic decays. This yield may then in turn be subtracted from the measured inclusive yield, leaving only the direct photons [14].

The statistical subtraction technique entails first calculating and plotting the invariant mass of two photons for all possible combinations of the identified photons within the event, divided into successive p_t bins. One then identifies similar events, i.e., similar centralities, inclusive yields, etc., and further calculates the invariant mass from the photons in the mixed similar events. This mixed yield must then be normalized to the number of events used in the event cocktail and will then represent the background. One then subtracts the calculated combinatorial background from the respective invariant mass plots, which should result in a peak at $\sim$139 MeV/c^2 and a smaller peak around $\sim$549 MeV/c^2 representing the π^0 and η^0 respectively. By accumulating the number of counts at the peaks will give an approximate yield of the meson decays, which may then be subtracted from the inclusive measured photon yield, resulting in the direct photon yield [14, 15].

The PHENIX experiment at RHIC successfully measured the direct photon spectra from Au-Au collisions at $\sqrt{s} = 200\ GeV$ per nucleon pair. The measured yield for different centralities are shown in figure 2.3. The results are in good agreement with the measured yields from p-p at the same C.M. energy and the pQCD calculated predictions, both after binary collision scaling [16]. This confirms the postulation that the photons may escape the medium nearly unaffected, and may thus be well suited as probes of the QGP, see also figure 1.5. The direct photon yield was expected to be dominated by thermal photons at $1 < p_t < 3\ GeV/c$, however, due to experimental uncertainties and a large background from hadronic decays, no conclusive results with respect to the thermal spectrum was obtained [17].

2.2 Passage of Photons through matter

Photons may interact with matter resulting in various different effects from the ejection of neutrons to the creation of electrons and positrons. This section will focus on the three main processes that lead to a detectable end-state electron. These processes are the Photoelectric effect, Compton scattering and the Pair-production processes. In the photoelectric effect and the pair-production processes the photon energy will be completely absorbed, whereas in the case of Compton scattering the photon may also

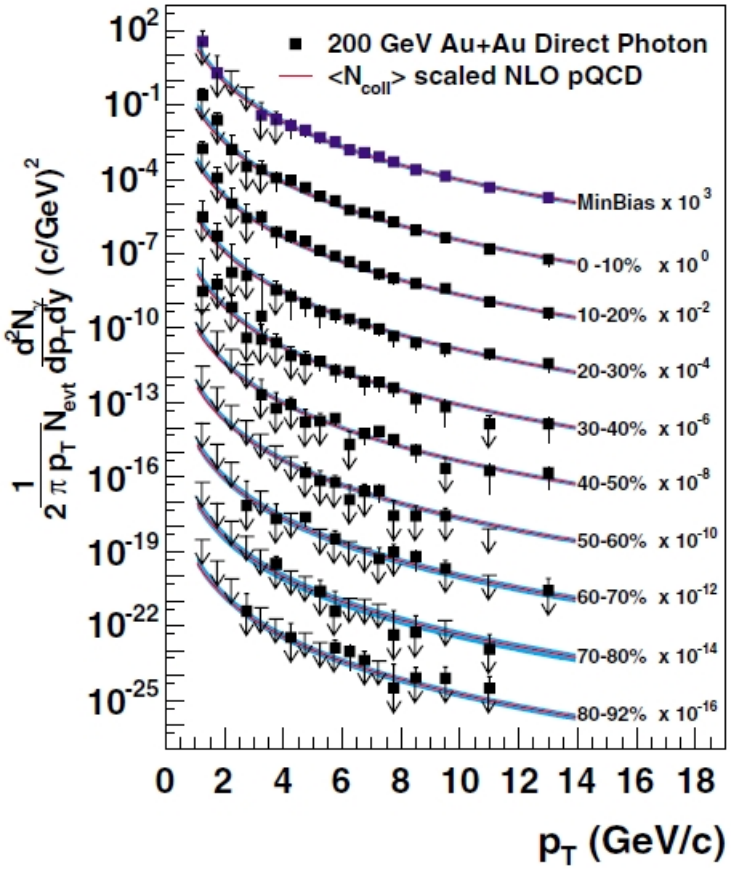

Figure 2.3: The measured direct photon yields with PHENIX for Au-Au collision at $\sqrt{s} = 200\ GeV$ per nucleon pair. The yields are plotted for different centralities, along with binary scaled pQCD calculations. The figure was taken from [16].

transfer fractions of its energy.

Photoelectric effect

The photoelectric effect is the dominant process at low photon energies, typically below a few hundred keV. When an incident photon interacts with an atom, the photon's energy may be absorbed, leading to the subsequent ejection of an inner-shell electron. A portion of the photon's energy will be used to liberate the electron, some energy will be transferred to the atom in terms of recoil, and the remaining energy will be carried as momentum by the electron. Now that there's an empty spot in one the inner-shells of the atom, an outer-shell electron may now transcend to the vacant lower state by emitting an photon with an energy matching that of the energy

difference between the two states. Different types of atoms have different spacing between their discretized electron energy states and the emitted photons will carry with them this energy difference. The radiation process described by the photon emission is termed Characteristic radiation, since the emitted photon energy is a characteristic of the atom.

Compton Scattering

Compton scattering is the the dominant process in the approximate energy interval between a few 100s keV and a few MeV. This process may occur between a photon and an outer-shell electron. An outer-shell electron will be loosely bound to the atom and the interaction with the photon may be considered to occur directly with the electron instead of the atom as a whole, contrary to the photoelectric effect. As an incident photon interacts with an electron, it may transfer a portion of its energy to the electron. This will result in the electron's subsequent liberation and the ionization of the atom. Due to conservation laws the photon will now leave the atom in a different direction then it entered and with a lower energy.

Pair production

The pair-production process is the dominant process above a few MeV. An incident photon in close proximity to a nucleus of an atom may convert to an electron and a positron through the pair-production process. A photon may also convert though the pair-production process by interacting with the atomic electrons, but this process is rare in comparison to that of the nucleus. The photon will cease to exist, and create an electron and positron pair. Due to energy conservation the photons must have an energy above 1.022 MeV/c^2 to undergo pair-production, since the mass of both the electrons and the positrons are 0.511 MeV/c^2. In reality the photons must have an energy slightly above that value for the process to occur, because some energy will be transfered to the nucleus in the form of recoil.

The mean free path expresses the average distance a photon must travel before it will suffer an interaction. The mean free path, λ_{pair}, of a photon for pair production is related to the radiation length given by [18] as (2.1). See figure 2.4 for a depiction of the photons cross sections plotted against its energy, in lead $Z = 82$.

$$\lambda_{pair} = \frac{9}{7} L_{rad} \tag{2.1}$$

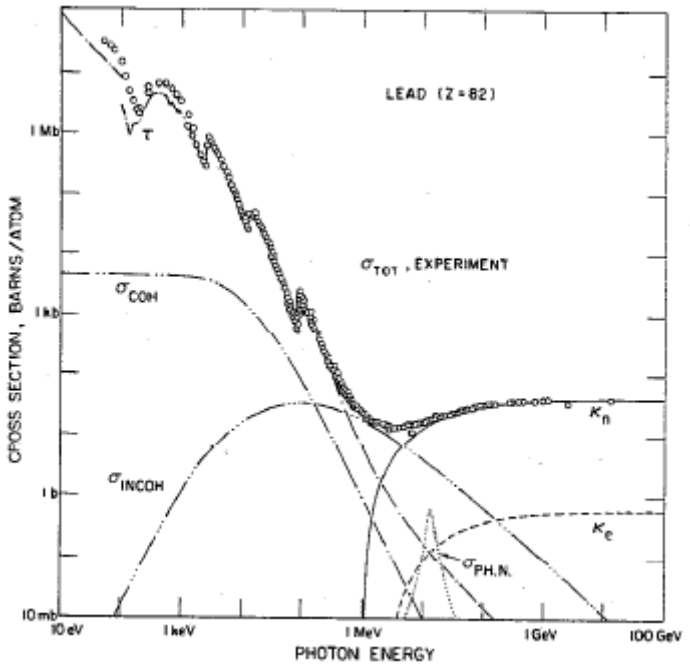

Figure 2.4: The figure shows the cross sections for the photon interactions plotted against the energy of the photon, in lead $Z = 82$. κ_n and κ_e represent the cross section of the pair production process of a photon in the electric field produced by the nucleus and electrons respectively. The figure was taken from [19].

Chapter 3

LHC - ALICE

The Large Hadron Collider (LHC) is a particle collider at the European Organization for Nuclear Research (CERN) near Geneva, Switzerland. The LHC is currently the largest and most energetic particle collider in the world. With a circumference of approximately 26.7 km the LHC inhabits the tunnel inherited from the LEP experiment approximately 100-150 meters underground, see figure 3.1.

The LHC has been designed to collide protons and heavy ions with center of mass (CM) energies never before reached by any other experiment(s). Along the beam line there are a number of detector experiments. The four main collision experiments are ALICE, ATLAS, CMS and LHCb, with ALICE being the detector that this thesis will focus upon.

ALICE is a general purpose heavy ion detector with a main focus on the strong interactions of nuclear matter. ALICE intends to probe the phase transitions of nuclear matter and the formation of a QGP at extreme temperatures and energy densities [20].

ATLAS is a general purpose detector designed to record data from p-p collisions. Among other subjects, ATLAS will search for the Higgs boson, supersymmetric particles, and heavy gauge bosons [21].

CMS will utilize high quality muon reconstruction to search for the Higgs boson, supersymmetric particles, and undiscovered heavy gauge bosons [22].

LHCb is dedicated to the investigation of hadrons comprised of at least one bottom (beauty) quark. Among its main goals, is the investigation of CP-violation and other rare processes occurring in the decays involving bottom-quarks [23].

In addition, there a two forward directed experiments, namely the TOTEM and LHCf. The LHCf will study particles in the very forward direction in

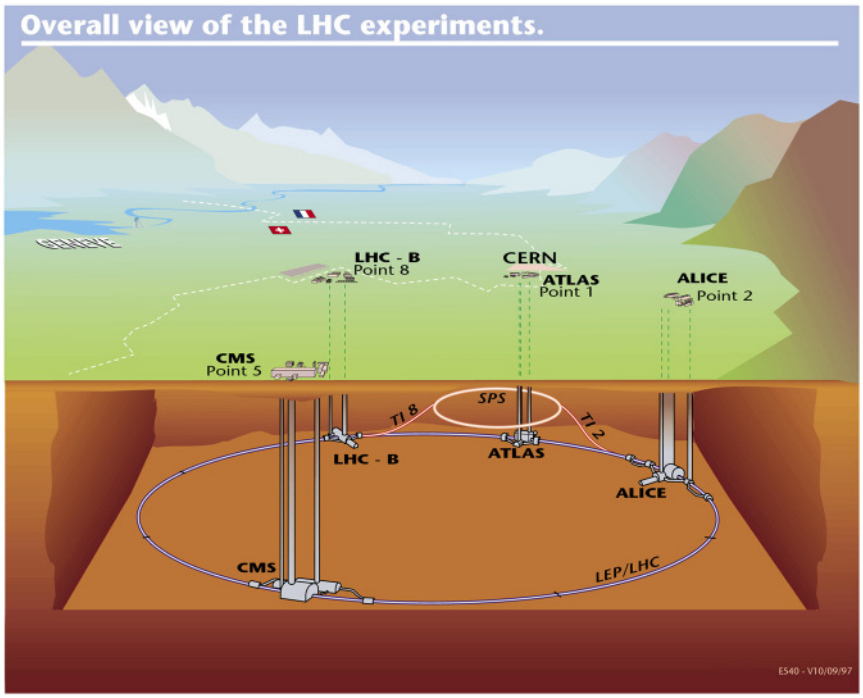

Figure 3.1: Drawing of the LHC beam tunnel situated ∼100–150 m underground. Four of the main detector experiments are depicted and labeled. The figure was taken from [26].

order to shed light on cosmic ray phenomena [24]. TOTEM will measure elastic and inelastic cross sections, and the diffractive dissociation for p-p collisions in the very forward region adjacent to CMS [25].

3.1 LHC - The Large Hadron Collider

The LHC will accelerate and collide protons and heavy ions at CM energies up to $\sqrt{s} = 14$ TeV and $\sqrt{s} = 5.5$ TeV per nucleon pair respectively. This will break the record for the previously highest CM energy for a collider held by RHIC, which collided gold ions at $\sqrt{s} = 200$ GeV per nucleon pair. The LHC will mainly collide p-p, with a few weeks set aside for Pb-Pb at the end of each year. Though ALICE is optimized for Pb-Pb, it will also record data from p-p, thereby allowing for detector calibration and providing reference material for when it records data from Pb-Pb. In addition, ALICE will provide increased statistics for the other dedicated p-p experiments. The reference data is needed to be able to determine which characteristics result from the initial hard partonic scattering of the quarks and gluons, and which originate from a strongly interacting medium.

During nominal operation the LHC will collide protons with a CM energy of $\sqrt{s} = 14\ TeV$ per nucleon pair with a luminosity of $L = 10^{34} cm^2 s^{-1}$, and lead (Pb) ions with a CM energy of $\sqrt{s} = 5.5\ TeV$ per nucleon pair with a luminosity of $L = 10^{27} cm^2 s^{-1}$ [27, 28]. As will be further discussed later in this chapter, ALICE will operate at lower luminosities for p-p collisions due to the formation of pile-up from mixed events in the main tracking detector. Currently, as of May 2011, the LHC has achieved peak luminosities of $\sim 1.1 \times 10^{33} cm^2 s^{-1}$ and $\sim 2.7\text{–}3.0 \times 10^{24} cm^2 s^{-1}$ for protons and lead respectively [29]. It will be steadily ramped up until it reaches its nominal target luminosities and collision energies, apart from in the shutdown periods set aside for detector upgrade and maintenance.

3.2 ALICE - A Large Ion Collider Experiment

A Large Ion Collision Experiment (ALICE) is a general purpose detector with its main focus on investigating the strongly interacting part of SM, namely QCD. It will investigate the formation and characteristics of the strongly interacting medium formed in heavy ion collisions through the analysis of the various probes and signals, which are characteristic of the different phases of nuclear matter. Due to the high particle multiplicities projected in Pb-Pb collisions, ALICE has been designed to handle a charged particle multiplicity of up to 8000 per unit rapidity at mid rapidity. Later estimates based on the extrapolations from RHIC measurements put the range for expected multiplicity at approximately 1500-4000 [20]. At the end of 2010, ALICE measured a charge particle multiplicity of $dN/d\eta = 1584 \pm 80$ at mid-rapidity while colliding Pb-Pb at a C.M. of 2.76 TeV per nucleon pair [30].

Eighteen subdetectors comprise the ALICE detector, see figure 3.2. The z-axis is defined to be parallel to the beam direction, where the positive axis points opposite that of the muon spectrometer. The x-axis is horizontally perpendicular to the beam direction with its positive axis pointing towards the right, while facing the muon spectrometer from the inside of the central barrel. The y-axis is vertically perpendicular to the beam direction with its positive axis pointing upwards. Typically, the detectors are classified as either central-barrel detectors or forward-directed detectors. This thesis will focus on a relevant selection of the central-barrel detectors and only briefly mention some of the others. For a description of all the subdetectors of ALICE the reader is referred to [20] and their respective technical design reports, such as [31, 32, 33].

3.2.1 Tracking detectors

As charged particles pass through matter they will deposit portions of their energy in the material, which may lead to the subsequent ionization of the

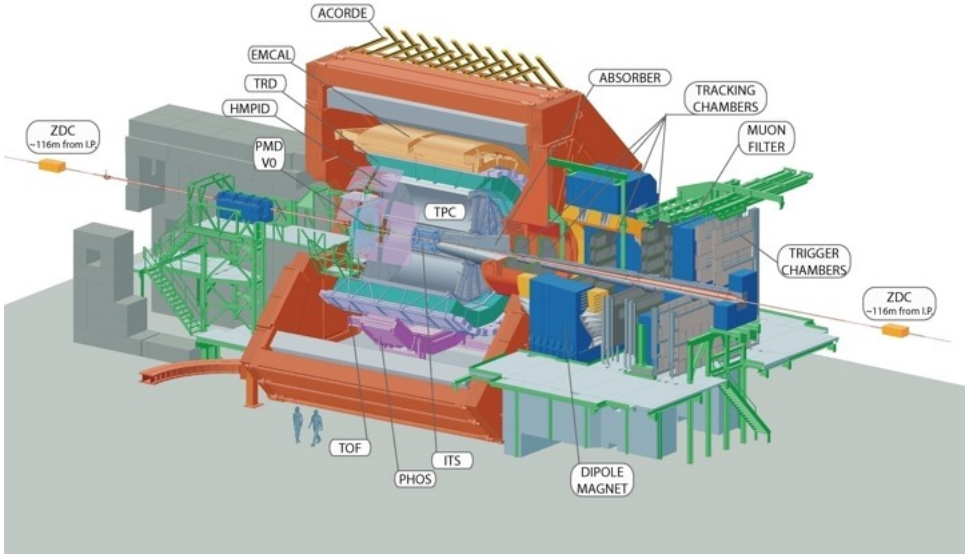

Figure 3.2: An illustration showing the subdetectors of ALICE, taken from [34].

atoms in the material, see chapter 4. An applied electric field will cause the liberated electron and ion to drift apart, which then in turn may be further read-out electronically. There are two general types of tracking detectors, namely compact solid-state detectors and gaseous detectors.

The central barrel tracking detectors consist of the ITS, TPC and the TRD. The ITS and TPC will be discussed in chapter 4 and will only be briefly presented in the current section.

The Inner Tracking System (ITS) is a six layer silicon solid-state tracking detector designed to pinpoint the primary and secondary vertices of the collisions. The 3–dimensional position of the primary vertex is determined with a resolution better than 100μm. The ITS will also provide particle identification (PID) for particles with low momenta, see section 4.2.

The Time Projection Chamber (TPC) is considered the main tracking detector of ALICE. The TPC is a time projection chamber consisting of a large drift region with a large number of MWPCs located at its endcaps, see section 4.3. The TPC can provide PID of electrons in an wide momentum range of 0.1 GeV/c to 100 GeV/c.

The Transition Radiation Detector's (TRD) main purpose is to provide electron identification for momenta above 1 GeV/c. It will also provide additional tracking information to improve the overall tracking and momentum resolutions in conjunction with the ITS and TPC. The TRD is comprised of 18 super modules each containing 30 detector modules arranged

in 6 layers. Each of the layers are comprised of 5 stacks of elements arranged parallel to the z-axis. Each element is made up of a radiator, a drift region, and a multi wire proportional chamber (MWPC) for read-out [20].

3.2.2 Particle identification

There are a number of detectors either dedicated or capable of PID in ALICE, such as the TOF, HMPID, and the aforementioned tracking detectors. PID over a large phase space and momentum range is an important design feature of ALICE, that has required the adoption of various different detector principles.

The Time Of Flight detector (TOF) is designed to provide PID in the intermediate momentum range: below 2.5 GeV/c for pions and kaons and up to 4 GeV/c for protons, with a separation for π/K and K/p better than 3σ. TOF will in conjunction with the ITS and TPC provide event-by-event identification of large samples of kaons, pions, and protons in the momentum range below 1 GeV/c [20, 35]. The detector is comprised of a series of Multi-gap Resistive-Plate Chambers (MRPC) arranged in 18 sectors along ϕ, and divided into 5 partitions along the z-axis, analogous to the TRD set up. TOF covers the region of $|\eta| < 0.9$ and $0 \leq \phi \leq 2\pi$. Some of the benefits of the MRPCs include the possibility to operate at atmospheric pressure, thereby eliminating the need for complex pressure systems and avoiding an increase in material budget. They may also be operated at high voltages allowing for high gains without the risk of electric discharge [20].

The High Momentum Particle Identification (HMPID) detector is comprised of 7 modules of Ring Imaging Cherenkov Counters (RICH), which are read out by Multi-Wire Pad Chambers (MWPC). The active area of the combined modules is approximately 10 m^2. The HMPID allows for PID of hadrons with higher momenta than the other detectors. It effectively raises the threshold for π/K and K/p separation up to 3 GeV/c and 5 GeV/c respectively [20]. The HMPID covers the range $|\eta| < 0.6$ with an azimuthal acceptance of $\triangle\phi = 57.61\,^\circ$ [31].

3.2.3 Electromagnetic calorimeters

Electromagnetic calorimeters are designed to measure the energy of electrons and photons. The incoming particles will interact with the material through the electromagnetic processes causing the particle to deposit its energy in the calorimeter, see section 4.1.2. The calorimeters are built large enough to completely absorb the entire energy of the incoming particle, i.e., measure the particle's energy. Heavier particles, such as hadrons, will not be completely absorbed in an electromagnetic calorimeter. For their energy measurement one would have to use a different kind of detector, duly named a hadronic calorimeter.

The central electromagnetic calorimeters of ALICE are the EMcal and PHOS detectors. One of the main goals of the calorimeters are the detection of photons with a wide range of momenta.

The ElectroMagnetic calorimeter (EMcal) is a Pb-scintillator sampling calorimeter that covers an approximate geometric range of $\eta < |0.7|$ and $\triangle\phi = 107\,^{\circ}$. It is positioned approximately opposite that of PHOS, enabling measurements of the correlated jets and photon-tagged jets in both calorimeters. The read out of EMcal is done with the combination of light shifting fibers and avalanche photodiodes [20].

The PHOton Spectrometer (PHOS) is a high resolution photon spectrometer that covers the range of $|\eta| < 0.12$ and $220\,^{\circ} < \phi < 320\,^{\circ}$. It consists of an arm of five detector modules, each containing an array of scintillator crystals. Due to the large particle density in Pb-Pb collisions, the scintillator material was chosen to be $PbWO_4$, since it has both a small Moliere radius and a sufficient light output, thereby enabling the measurement of the lowest energies of interest with a sufficient resolution [20].

3.2.4 Trigger detectors

ALICE has implemented a series of different trigger detectors. This allows for event selection on a detector level and also the ability to signal when a collision has occurred. The T0 detector is situated around the beam-pipe and measures the event time with a precision better than 25 ps. The V0 detector consists of scintillator counters and acts as the minimum bias trigger and enables the rejection of beam gas interactions. Minimum bias means the detection of all of the inelastic collisions of the colliding nuclei.

The ACORDE sits on top of the L3 magnet and is designed to trigger on cosmic rays. The ACORDE is vital for the alignment of the central barrel detectors after their installation and will also record data for cosmic ray physics. The Forward Multiplicity Detector (FMD) measures the multiplicity of a collision in the range $-3.4 < \eta < -1.7$ and $1.7 < \eta < 5$. The photon multiplicity detector (PMD) covers the range of $2.3 < \eta < 3.7$ and is designed to measure the multiplicity and spatial distribution of photons emerging from a collision. The Zero Degree Calorimeters (ZDC) is a set of neutron and proton calorimeters, which are situated at 116 m along the beam pipe at either side of the interaction point (IP). The ZDC is designed to measure the number of contributors in a collision, allowing for a trigger on central and ultra-peripheral events. For instance, a simplified example could be measuring the proton and neutron yields in the ZDC, thereby, signaling the centrality of the collisions, i.e., the lower the yields are the more central a collision is. The ZEM is a electromagnetic calorimeter designed to improve the centrality measurements of the ZDC [20].

3.2.5 Trigger Scheme

In ALICE, the trigger scheme is divided into a hierarchy of levels which are governed by the Central Trigger Processor (CTP). The levels consist of the L0, L1, L2 and the HLT. Levels 0–2 receive and relay trigger information to the CTP. In addition, some detectors require a pre-trigger that wakes up the detector from its stand-by state and signifies that the detector should prepare for data-taking, one such detector is the TRD.

One important task of the trigger system of ALICE is the past-future protection of the read-out of data with respect to pile-up events. Due to the interaction rate of 8 kHz for Pb-Pb, the detectors may be occupied by particles originating from different events. As a solution, ALICE has implemented a past-future protection system that enables the discrimination of pile-up events and non-pile-up events. For Pb-Pb, the requirement is that no other central collision and only a few ultra-peripheral collisions may occur within a time frame of $\pm$ 88μs, where the time is decided by the maximum drift time of the TPC, the slowest detector in ALICE. Due to the large multiplicities in Pb-Pb collisions and with the additional information from the LHC, such as the bunch spacing and crossing frequencies, one may use the different primary vertex positions to distinguish between the pile-up and non-pile-up events. For example, particle tracks originating from different collisions will point towards different primary vertices as the ionization-liberated electrons from the earlier event will already have begun to drift a distance towards the endplates of the TPC, when the particles from the later collisions begin to ionize the gas. After the removal of pile-up, ALICE will record data at a rate of $\sim$1 kHz for p-p collisions and $\sim$200 Hz for clean and central Pb-Pb collisions [20, 10].

Trigger hierarchy

Only the fastest detectors have the ability to send a L0 trigger signal to the CTP. Once the detector registers a signal above threshold, it immediately checks the signals against its relevant trigger conditions and if deemed adequate, it sends a L0 signal to the CTP. The CTP collects and combines all L0s from the different detectors, and if the events show the wanted characteristics it issues the L0 signal to all, or to a relevant subsection, of the detectors in ALICE. The L0 trigger is issued by the CTP 1.2 μs after a collision has occurred.

Upon the acceptance of a L0 from the CTP, the detectors continue collecting data and process the information they've stored in their data buffers. If the event still shows the wanted characteristics, the detectors issue a L1 signal to the CTP containing the relevant information needed by the CTP. Once the CTP has received all the relevant L1 trigger signals, it further processes the signals and issues a global L1 trigger signal to all of the detectors

at a time of 6.5μs after a collision.

The CTP can issue two L2 signals, namely the L2a (accept) and the L2r (reject). The L2a signifies that the event fulfills the trigger conditions and that the detectors should read-out their data for further processing and storage. The L2r is issued if the event does not hold up against the applied trigger conditions, and signals the detectors to clear their buffers so that they're ready for the data-taking of the next event. Since the CTP must wait for all of the detectors to collect the data from the event before issuing the final L2 signal, it may only be issued after a time of 88μs corresponding to the maximum drift time of the TPC. After a L2a is issued the DAQ begins the subsequent readout of data.

3.2.6 DAQ - Data Acquisition System

The Data Acquisition System (DAQ) is responsible for the read-out, transport, and subsequent storage of the data from the detectors after receiving a signal from the CTP that all, or a portion, of the detectors should be read-out. The data is buffered in the Front End Read Out cards (FEROs) of each detector, and the FEROs are connected via optical fiber cables called detector data links (DDLs). An important component of the DAQ is the read-out and receiver cards (D-RORCs). They receive and transmit the data to further processing components of the DAQ. A key characteristic of ALICE is that all of the 18 subdetectors are readout in the same way, via DDLs and connected to their respective D-RORCs [20, 36].

The DAQs design bandwidth of 1.25 GB/s was far surpassed by the recent upgrade of the D-RORCs. The on-board PCI-X bus was replaced by the newer and faster PCI-Express resulting in improved bandwidth capabilities [37], particularly for large event sizes, see table 3.1. As a reference, note that typical event sizes for p-p and Pb-Pb are 2.5 Mb and 86.5 Mb respectively. With the aforementioned upgrade, along with others, the bandwidth capability of the DAQ has increased to handle up to 4 GB/s [38].

Rare and common trigger handling

The Data Acquisition and Testing Environment (DATE) is the software framework responsible for the DAQ operation and control. Implemented in

Event size (bytes)	PCI-X (MB/s)	PCI-ex (MB/s)
10 000	300.88	401.18
100 000	367.15	815.89

Table 3.1: Table showing the increased through put of data before and after DAQ upgrade, taken from [37].

DATE is the ability to set values for the amount of data to be read-out of specific events. Generally, the buffers of the FEROs are divided into two parts, one part for events originating from common triggers (Centrality, etc.) and the other for rare triggers (Di-muon, D0, etc.). If the rare-trigger buffers are above a maximum level when the DAQ receives information that a rare-event has occurred from the CTP, it may temporarily commandeer a portion of the common-buffer for the rare-events as they have a higher priority since they occur with a lower frequency. When the rare-buffer returns to a value below the set value, the commandeered portion of the buffer is returned to the common section.

Data flow and Event building

Upon receiving information from the detectors, the CTP may issue a L2a trigger signal, which is passed on to the Local Trigger Units (LTUs) for each relevant detector signaling that they should prepare their buffers for read-out. The LTUs send a signal via the Timing and Trigger Control system (TTC) indicating that the detector has received a L2a from the CTP and that it is ready for read-out. With the information from the TTC, the DAQ begins the read-out from the FEROs. As mentioned above, all data from the detectors are transported via DDLs to their respective D-RORCs. The D-RORCs may connect to two DDLs. For the detectors commissioned for HLT one of the DDLs sends a copy of the raw data to the HLT processing farm for on-line reconstruction and event selection or rejection (as of this writing only the rejection option is applicable). The DDLs from the D-RORCs are interfaced to the HLT network through the HLT Read-out and Receiver Cards (H-RORCs). These in turn pass on the data to the Front End Processors nodes (FEPs) of the HLT computing farm, where the on-line reconstruction and event rejection is implemented. From the FEPs the data is again returned to another set of D-RORCs. The HLT also provides data compression needed for Pb-Pb collisions, and on-line calibration of the subdetectors. The HLT will be further discussed later in this section.

All of the D-RORCs are interfaced with Local Data Concentrators (LDCs), that are responsible for sub-event building, e.g., one LDC may be responsible for the data-building from one portion of a subdetector, such as a the inner section of one of the 36 sectors of the TPC. The LDCs pass on their finished sub-event to the Global Data Collectors (GDCs), which builds a complete event from all the sub-events. The Event Distribution Manager system (EDM) acts as the mediator between the LDCs and GDCs. The EDM ensures that the work load is evenly distributed over the GDCs, and that a GDC receives all the relevant sub-events from the different LDCs, in order to accurately and efficiently build an entire event originating from the same trigger. The GDCs publish the completed events to their respective local Transient Data Storage network (TDS), from which it is further

transported to the Permanent data Storage (PDS), where it is written to tape and ready for off-line reconstruction and analysis. See figure 3.3 for a schematic overview of the data flow in ALICE [20, 36].

3.2.7 HLT - High Level Trigger

The *High Level Trigger* (HLT) system is comprised of both an extensive hardware application consisting of a computer farm of 135 FEP nodes and 109 computing nodes (October 2010) [39], and a logical software based level operating above the L2 trigger level. The main goal of the HLT is to trigger on rare and interesting events and reduce the data flow to permanent storage. It is designed to handle a data rate of 25 GBytes/s and reduce it to 1.25 GBytes/s, the design rate of the DAQ. The HLT operates with a *Publisher-Subscriber* framework, that entails that the data is stored in a large portion of memory allocated as shared memory. This memory may then in turn either be accessed, or written to, by the relevant processes, thereby limiting the need for timely and large data transfers. The HLT ultimately reduces the data rate through event-by-event triggering on the on-line reconstructed events, through region of interest read-out from the detectors, and through a subsequent data compression. These processes are briefly described below.

The FEP nodes in the HLT computer farm receive a copy of the raw data from the D-RORCs via DDLs. The HLT implements the on-line reconstruction via time efficient reconstruction algorithms and processing schemes. It operates under a parallel processing hierarchy, where events are reconstructed simultaneously on the different processing nodes and merged into complete events. A schematic diagram of the data flow is shown in figure 3.4. It also utilizes pipelined processing, where the goal is to minimize the latency in merging the outputs of many processes operating on different nodes. In pipeline data processing, the finished tasks are stored in a buffer where they await the completion of the other relevant tasks before they may be merged. Temporarily storing the finished processes in the buffers will free up local resources so the CPU can begin processing the next event. After the complete reconstruction has finished, the HLT system checks the event against a series of trigger conditions checking for favorable rare signals. If the desired characteristic was only observed in a portion of the detectors, the HLT may signal the DAQ to only read out these specific section(s) of the relevant detector(s). This is called the *Region Of Interest* feature, it basically sends a list of the DDLs to the DAQ telling it which of them it should read out data from, and subsequently record. The HLT compression capabilities include both a lossy and a loss-less compression of data, the latter allows for the complete off-line reconstruction of the original event, whereas the former will not. Although, the lossy compression does forward the needed information such as tracks, momentum, PID, etc., allowing for the subsequent off-line analysis of the data.

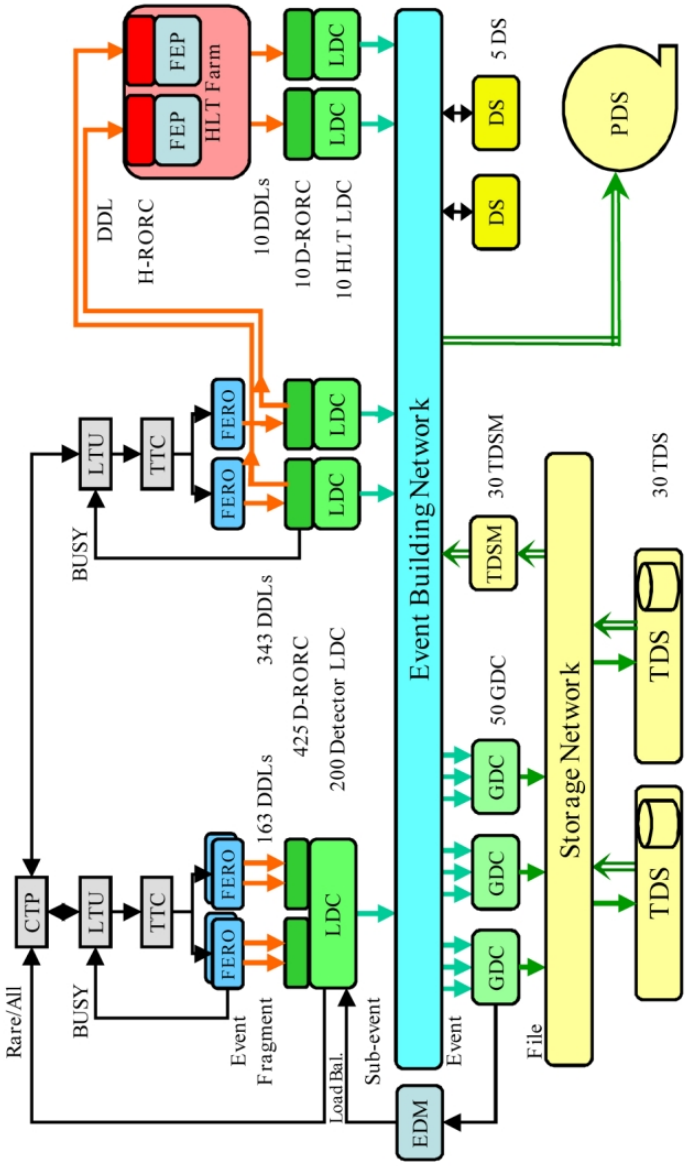

Figure 3.3: A schematic diagram showing the data flow of ALICE. The figure was taken from [36].

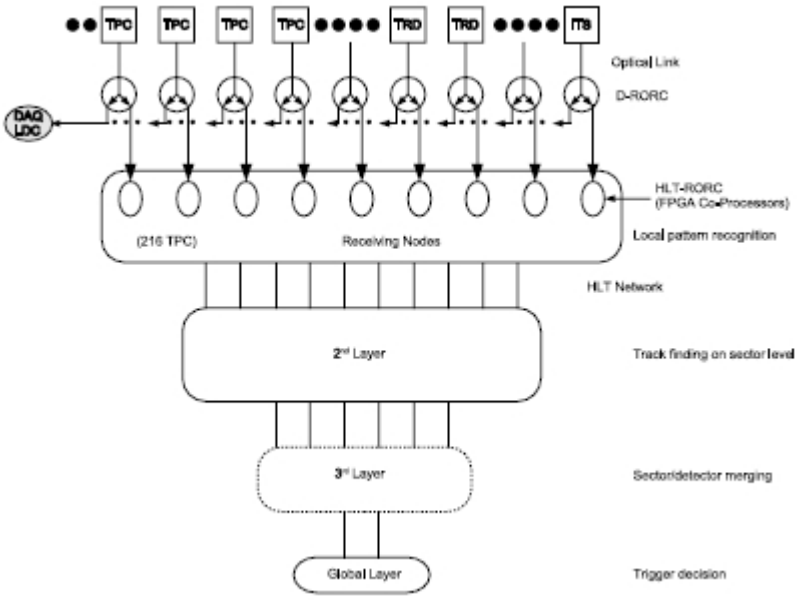

Figure 3.4: A schematic diagram showing the data flow of the HLT parallel processing scheme and merging. The figure was taken from [40].

Chapter 4

ALICE tracking detectors - The ITS and TPC

This chapter will focus on the two inner-most central barrel tracking detectors, namely the ITS and the TPC. In order for a particle to be detected, it needs to deposit energy in the material comprising the active region of the detector. The first section will be dedicated to the fundamental physical processes that lead to the energy loss of charged particles in matter. The subsequent sections will deal with the working principles, layout, and performance of the ITS and the TPC. For a more detailed description of the ITS and TPC, the reader is referred to their respective technical design reports [32, 33].

4.1 Passage of charged particles through matter

Since the cross sections of the different processes generally depend on the mass of the particle, we will treat the heavy and the light charged particles separately. We define heavy particles as those particles having a mass in the range of 0.1 m_p to a few m_p, where m_p denotes the rest-mass of the proton. The light particles include the electrons, the positrons, and the photons.

4.1.1 Heavy charged particles

There are two main features one may observe from a heavy charged particle passing through material: (1) energy transfer from the particle to the material, (2) a deflection of the particle from its incident direction [18]. These features are primarily the result of two processes:

- inelastic collisions with the atomic electrons of the material
- elastic scattering from the nuclei

There are other process that may contribute to the energy loss and deflection of heavy charged particles, however, they are typically rare in comparison with the ones mentioned above. Some of the possible interactions are:

- emission of Cherenkov radiation
- nuclear reactions
- bremsstrahlung

For heavy charged particles the majority of the energy loss is due to the inelastic collisions with atomic electrons. Energy loss through a collision is a statistical process, governed by the probabilities derived from quantum mechanics. Even though statistical nature is present, there are typically a large number of collisions per macroscopic unit path length and a small variation in the energy lost per collision. This permits the meaningful definition of an average energy loss per unit path length, often denoted the stopping power or dE/dx. The equation for energy loss via inelastic collisions of heavy charged particles is well described by the Bethe-Bloch equation with two corrections implemented, given by [18] as (4.1). The Bethe-Bloch is valid for velocities ranging from the relativistic region down to $\beta \approx 0.1$.

$$-\frac{dE}{dx} = 2\pi N_a r_e^2 m_e c^2 \rho \frac{Z}{A}\frac{z^2}{\beta^2}\left[ln\left(\frac{2m_e\gamma^2 v^2 W_{max}}{I^2}\right) - 2\beta^2 - \delta - 2\frac{C}{Z}\right] \quad (4.1)$$

with

r_e:	classical electron radius $= 2.817x10^{13}$cm
m_e:	electron mass
N_a:	Avogadro's number $= 6.022 \times 10^{23} mol^{-1}$
I:	mean excitation potential
Z:	atomic number of absorbing material
A:	atomic weight of absorbing material
ρ:	density of absorbing material
z:	charge of incident particle in units of e
$\beta =$	v/c of the incident particle
$\gamma =$	$1/\sqrt{1-\beta^2}$
δ:	density correction
C:	shell correction
W_{max}:	maximum energy transfer in a single collision

The two last terms in (4.1) are the shell and density corrections. The density effect arises from the fact that the electric field of an incident charged particle tends to polarize the atoms along its path through a material. The polarization shields the outer lying electrons, limiting their interactions with the incoming particle and thereby reducing its average energy loss. This density effect is small for low energies and grows with increasing energy. The shell correction corrects for the effects when the projectile particle has a velocity comparable to, or smaller than, that of the orbital velocity of the bound electrons in the atom. The assumption made by the Bethe-Bloch that the atomic electron is approximately stationary with respect to the incident particle will no longer be valid and the formula's validity will break down [18].

Some key features of the Bethe-Bloch can be seen by figure 4.1. At an approximate velocity of v = 0.96 c the particle will experience a minimal energy loss. The energy at which the minimum energy loss occurs is almost the same for all particles with the same charge, regardless of their mass. Particles with this approximate energy are referred to as minimum ionizing. For energies below the minimum ionizing value energy loss is dominated by the $1/\beta$ term. At these energies most particles show a different dE/dx curve then other particles, see figure 4.1. These distinct curves may then be used to identify the different particles, a principle which is frequently exploited in particle detectors. At relativistic energies the $1/\beta$ term approaches a constant value and the logarithmic term dominates. This leads to a rise in the average energy loss, known as the relativistic rise. As mentioned above, the relativistic rise is partially cancelled by the density effect.

4.1.2 Light charged Particle

Light charged particles, i.e., electrons and positrons, also lose energy through inelastic collisions with the atomic electrons of a medium. However, due to their small masses an additional effect may contribute to, and at high energies even dominate, their energy loss. At high energies an electron radiates photons as it is de-accelerated in the electric field of a nucleus, and to a lesser extent, due to the lower charge densities, the surrounding electrons. This effect is called bremsstrahlung. Bremsstrahlung is strongly dependent on the energy and mass of the particle and is typically dominant at large energies, typically at energies of the order of tens of MeV and above for electrons.

$$\left(\frac{dE}{dx}\right)_{tot} = \left(\frac{dE}{dx}\right)_{rad} + \left(\frac{dE}{dx}\right)_{coll} \tag{4.2}$$

The total average energy loss of electrons is given by two terms, one from the radiation of photons and the other from the collisions with atomic electrons (4.2). Since electrons and positrons are fermions and carry a small

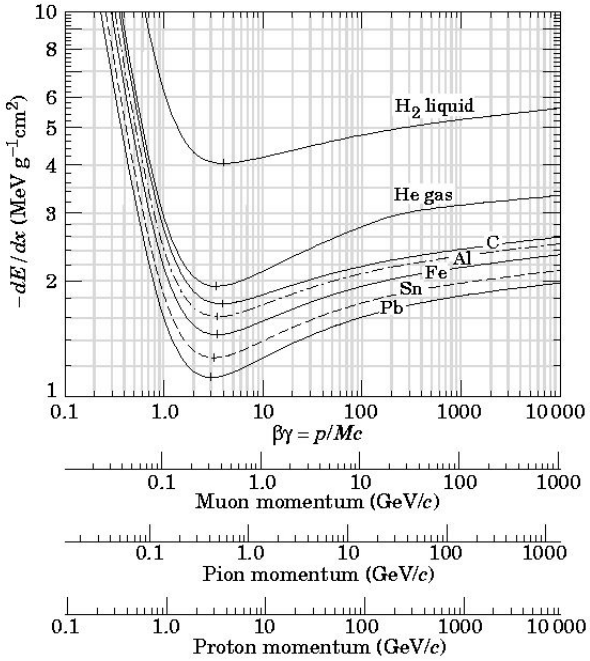

Figure 4.1: The average energy loss due to collisions is plotted for a variety of different particles. The figure was taken from [41].

mass the Bethe-Bloch must be modified to accurately describe their energy loss through collisions. Their small mass may lead to strong deflections from their original paths, something not accounted for by the original Bethe-Bloch (4.1). Since the collisions are now between identical particles, their indistinguishability must also be considered. These corrections lead to a new dE/dx valid for electrons and positrons given by [18] as (4.3), where τ is the kinetic energy of the particle in units of $m_e c^2$, where $F(\tau)$ is given for electrons as (4.4) and positrons as (4.5). The remaining quantities are described by (4.1). We will also define two important quantities related to the energy loss, namely the critical energy and the radiation length.

$$-\frac{dE}{dx} = 2\pi N_a r_e^2 m_e c^2 \rho \frac{Z}{A}\frac{1}{\beta^2}\left[ln\left(\frac{\tau^2(\tau+2)}{2(I/m_e c^2)}\right) + F(\tau) - \delta - 2\frac{C}{Z}\right] \tag{4.3}$$

$$F(\tau) = 1 - \beta^2 + \frac{\frac{\tau^2}{8} - (2\tau+1)ln2}{(\tau+1)^2} \tag{4.4}$$

$$F(\tau) = 2ln2 - \frac{\beta^2}{12}\left(23\frac{14}{\tau+2}\frac{10}{(\tau+2)^2} + \frac{4}{(\tau+2)^3}\right) \tag{4.5}$$

Critical Energy As the energy loss by radiation depends on the type of material, we may define a critical energy for each material at which the energy loss through radiation is equal to that through collisions. Below this critical energy, the energy loss will be dominated by collisions and above the contribution from radiation will dominate. An approximate formula for E_c is given by [18] as (4.6), where Z is the atomic number of the material.

$$E_c = \frac{800MeV}{Z + 1.2} \tag{4.6}$$

Radiation Length The radiation length is defined as the distance over which the electron energy is reduced by a factor $1/e$ solely due to radiation loss. An equation for the radiation length is given by [18] as (4.7), where α is the electromagnetic coupling constant, $\alpha = 1/137$, $f(Z)$ is a small correction to the born approximation given by equation (4.8), with $a = Z/\alpha$, and the remaining quantities are described in equation (4.1).

$$\frac{1}{L_{rad}} = [4Z(Z+1)\frac{\rho N_a}{A}]r_e^2\alpha\left[ln(183Z^{-\frac{1}{3}} - f(Z)\right] \tag{4.7}$$

$$f(Z) \simeq a^2\left[\left(1+a^2\right)^{-1} + 0.20206 - 0.0369a^2 + 0.0083a^4 - 0.002a^6\right] \tag{4.8}$$

Electromagnetic Showers

An electromagnetic shower arises from the combination of two effects, namely bremsstrahlung from a high energy electron and the subsequent conversion of the photon through the pair-production process. The process may be initiated by the electron and photon alike, given that they have a high enough energy to interact through the relevant processes. For instance, a high energy electron enters a dense material and radiates a photon. The radiated photon converts to an electron and a positron, which have enough energy to undergo bremsstrahlung and further emit a photon each. These photons in turn convert to additional electron-positron pairs. The process continues in this fashion until the energy of the electrons and photons reaches a threshold where other interactions dominate their respective energy loss, or in the case of the photon where the pair-production process is forbidden due to energy conservation. The EMcal and PHOS detectors are designed to fully absorb the electromagnetic showers produced by light particles traversing their active regions. An important quantity when discussing electromagnetic showers is the *Moliere radius* given by [42] to be (4.9). The importance may be

understood from the fact that 99 % of the energy of a shower is contained within $3\times R_M$.

$$R_M = 21MeV \times \frac{L_{rad}}{E_c} \tag{4.9}$$

4.2 ITS - The Inner Tracking System

The x and y coordinates of the interaction point in a collision are fixed by the small sizes of the colliding bunches at the LHC, which have a r.m.s. width of approximately $\sigma_x = \sigma_y = 15\ \mu m$ [32]. In the beam direction, however, the bunches have a spread of approximately 7.5 cm, corresponding to a r.m.s. of $\sigma_z = 5.3\ cm$ [32]. The Inner Tracking System is located symmetrically around the beam pipe, and one of its main goals is to locate the position of the primary vertex with a high spatial resolution. Prior to track reconstruction, resolutions of 10 μm and 90 μm in the beam direction are obtainable for Pb-Pb and p-p collisions respectively. The vertex is determined through a two-hit correlation algorithm operating with the two inner-most layers of the ITS. The lower vertex resolutions for p-p collisions are due to their lower multiplicities, which in turn provide less hits in the ITS layers than that produced in the Pb-Pb collisions [32].[1]

The ITS is also charged with the task of locating the secondary vertices from particles decaying close to the primary vertex, such as hyperons and heavy mesons. The ITS will improve the tracking and momentum resolutions obtained with the TPC and TRD, and through dE/dx measurements it may act as a stand-alone particle spectrometer for particles with low momenta.

The Inner Tracking System (ITS) is comprised of six layers of silicon solid-state detectors. Three different types of detectors are used in the various layers, namely silicon pixel detectors, silicon drift detectors and silicon strip detectors. All of the detectors in the ITS are based on the characteristics of doped semiconductors. This section will outline the working principles of semiconductors used in detectors, and later describe the performance and specifications of each of the different detectors comprising the ITS.

4.2.1 Working principle - Solid state detectors

Semiconductors are solid-state crystalline materials where the valence electrons in their outer atomic shells form covalent bonds with their neighboring atoms in a crystal lattice. The large number of atoms equally spaced in a crystal lattice lead to an inherent degeneracy of the electron energy levels. The electrons, being fermions, must obey the Pauli exclusion principle which

[1] A *hit*, as used in this context, corresponds to localized energy depositions from the traversing particles in the detector material.

breaks the degeneracy by splitting the energy levels. Due to the large number of atoms in a crystal, the levels will be closely spaced as the spacing of the energy levels in the recipricol lattice is proportional to $1/N_a$, where N_a is the number of atoms in the crystal. Thus the large number of closely spaced discrete energy states may be well approximated by a continuum, and are often classified as energy bands. When all of the atoms are in their ground state the electrons will reside in the energy levels comprising the *valence band*. If energy is absorbed by an atom, an electron may be liberated from the atom and excited to the *conduction band*, where it will be free to roam the crystal. Depending on the energy gap between the valence and conduction band a material may be classified as either a *metal*, an *insulator*, or a *semiconductor*. A metal is a material with adjoint valence and conduction bands, and exhibits a high conductivity. Insulators have low conductivities, and large energy gaps between their valence and conduction bands. Semiconductors have relatively small gaps between their valence and conduction bands, typical of the order of a few eV [18]. They have a higher conductivity than insulators, but lower than metals.

If enough energy is absorbed by a semiconductor, an electron from the valence band may be excited to the conduction band, leaving behind a hole in the valence band with an apparent positive charge. Both the electrons and the holes are effectively charge carriers and contribute to the net current flowing through a semiconductor when subjected to an electric field.

A semiconductor made entirely of a pure homogeneous crystalline material is denoted an *intrinsic semiconductor*. However, a perfect intrinsic semiconductor will never truely exist as a certain amount of impurities will always be present in its production, therefore, the term as more commonly used refers to a semiconductor with a high level of purity. Impurities may result in the addition of localized energy levels in the forbidden energy region between the valence and conduction band. Depending on the depth of the additional levels, they may change the characteristics of the semiconductor in a favorable or dis-favorable manor. Energy levels deep in the energy gap midway between the bands are often denoted trapping or recombination centers, as they may trap the conducting charge carriers, or lead to an increased rate of annihilation between the electrons and holes. Depending on the interaction rate of the two processes, both types may lead to a decrease in energy resolution as a portion of the liberated charge from the incident ionization will be undetectable.

It may often be advantages to introduce a controlled level of a impurities to an intrinsic semiconductor, these are referred to as doped or extrinsic semiconductors. Intrinsic semiconductors are commonly made of either Silicon (Si) or Germanium (Ge), both of which are tetravalent atoms with four electrons in their outer atomic shell. If a low level of pentevalent atoms, typically P, As, or Sb, are introduced in an intrinsic semiconductor (Si,Ge), then only four of its valence electrons may reside in the same atomic levels

as the rest of the atoms. The fifth will be forced to the next shell resulting in displaced energy levels in the forbidden region close to the conduction band. The energy required to excite an electron from one of these levels is substantially less than that required to excite an electron from the valence band. Therefore, incident radiation depositing energy in the material may excite a larger number of electrons, resulting in a larger detectable signal than in an intrinsic semiconductor. The same principles holds for trivalent doping of an intinsic semiconductor, but in contrast to the pentevalent case this leads to additional hole-levels near the valence band where the holes may be excited to the valence band. Pentevalent doped semiconductors are denoted n-type as they lead to an addition of negative charge carriers, and in the same fashion trivalent doped semiconductors are called p-type. Extrinsic semiconductors with a high level of doping are denoted by a plus sign (n^+ and p^+), they are commonly used as an intermediate coupling between the semiconductor and the metal leads of an electrical circuit. Semiconductors with an equal amount of oppositely charged charge carriers are called composite semiconductors and denoted by i. Though they share many characteristics with intrinsic semiconductors they are by definition not intrinsic.

The semiconductors used in modern particle detectors are often made in such a way that one side of the semiconductor is p-type and other is n-type. Due to the abundance of negative and positive charge carriers on either side of the semiconductor, diffusion will cause the holes to migrate towards the n-side and the electrons towards the p-side, resulting in a current flowing through the semiconductor. However, since the semiconductor is comprised of neutral atoms the diffusion process will result in the build-up of a net negative charge at the p-side and a net positive charge at the n-side. The charge differences on either side leads to an electric field in the semiconductor, which causes the electrons and holes to drift back towards their original sides. When the current produced by the electric field is equal and opposite to that produced by the diffusion process, the semiconductor is said to be in a state of equilibrium. Any free charge carriers in the region between the n-side and p-side are swept away by the electric field, thereby leaving the junction between the n-side and p-side void of any free charge carriers. This region is called the depletion zone and its size is governed by the concentration of charge carriers [18, 43].

Incident radiation traversing the depletion zone will ionize the material producing electron-holes pairs. The electric field will subsequently sweep the charge carriers towards either side of the semiconductor. If connected in a closed electrical circuit, the drifting charges will induce a current at the connected electrodes, where the amplitude of the signal will be proportional to the energy deposited by the incident particle. If one further applies a reversed bias voltage to the semiconductor by connecting the p-side to the positive lead and the n-side to the negative lead, one will effectively increase the magnitude of the electric field in the semiconductor resulting in the

expansion of the depletion zone. By increasing the external potential, the depletion zone may be made to extend the entire volume of the semiconductors. A further increase in the bias voltage will lead to a quicker rise time of the induced signal as the drift speeds of the charge carriers are proportional to the magnitude of the electric field. The maximum operating voltage is given by the resistance of the semiconductor. If operated with higher voltages the semiconductor will start conducting, as the electrons will be given enough energy to overcome the inherent $\vec{E}$-field across the depletion zone, which was produced by the different concentrations of the charge carriers at the ends of the semiconductor.

One of the benefits of solid-state detectors over that of gaseous detectors is that the energy required to produce an electron-hole pair is typically an order of magnitude smaller than that required to ionize a gas molecule [18]. In addition, a solid has a higher density than a gas which results in a higher stopping power. Solid state detectors may be made to extend small areas, where the minimum size of the active area facing the incident radiation is typically governed by the read-out electronics used in the detector. These effects lead to higher achievable granularities and energy resolutions than its gaseous detector counter parts. As will be described in more detail later in this section, the semiconductors typically require a cooling system to limit noise in the detector. The additional read-out electronics and cryogenic systems result in a higher cost and a more complicated installation process.

Solid-state detectors

Figure 4.2 illustrates three main types of solid-state detectors, namely the pixel detector, the drift detector, and the strip detector. As mentioned above, the detectors utilize heavily doped semiconductors as a intermediate coupling to the metal leads of an electric circuit. These n^+ and p^+ materials may be considered the anode and cathode of the semiconductor based detectors.

The pixel detector (fig 4.2a) is comprised of small separate semiconductor detectors arranged and coupled in a 2-dimensional array capable of tracking with a high spatial resolution. As mentioned above, the minimum size of the pixel is typically limited by the read-out electronics of the detector. The drift detectors (fig 4.2c) have p^+ strips on both the top and bottom of a n-type semiconductor, and a single n^+ strip is positioned at one of the sides and acts as the anode. As the incident radiation liberates electron-hole pairs in the semiconductor, the electrons will drift longitudinaly along the silicon wafer and towards the anode strip, and the holes will drift latitudinaly towards the p^+ strips. The double-sided strip detector (fig 4.2b) may consist of a n-type semiconductor with parallell p^+ strips runnng on the top of the wafer, and n^+ strips running orthagonal to p^+ strips on the bottom. As the incident radiation liberates the charge carriers, the electrons and holes will

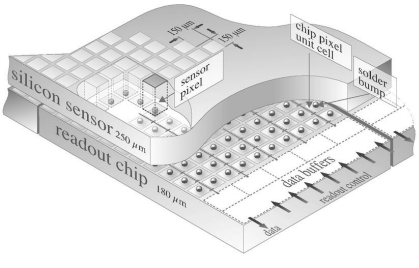

(a) Pixel detector

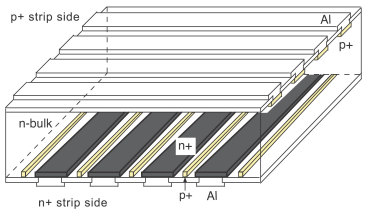

(b) Double-sided strip detector

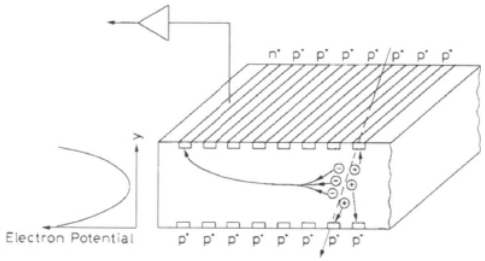

(c) Drift detector

Figure 4.2: Illustrations of semiconductors used as detectors. Figure (a) shows a pixel detector, (b) shows the double-sided strip detector, and (c) shows the drift detector along with the vertical component of the potential. The figures (a, b, c) were taken from [44, 45, 18] respectively.

then drift towards the n^+ strips and p^+ strips respectively. In the case of the drift and strip detectors, the two dimensional position may be calculated by *the center of gravity method* as described in [18], whereas with the pixel detectors, the position may be given directly by the noting the position of the pixel which registered a signal above its set threshold.

There will always be some current flowing through a solid-state detector, even without incident particles ionizing the active region. This is known as the noise, or leakage current, and is largely influenced by its external operating conditions. Thermaly excited lattice vibrations may produce electron-hole pairs through the scattering of phonons off the electrons in a crystal lattice [2]. A phonon may transfer portions of its energy to an electron in a collision, which may lead to the subsequent excitation of the electron to the conduction band. Light contamination may also largely contribute to the leakage current as the energy of visual light is approxiamtely 3 eV, which is larger than the energy gaps of silicon and germanium semiconductors under normal operating conditions. These contributions may be reduced by the

[2]Phonons are quasiparticles representing the quanta of vibrational energy in a crystal lattice. The phonon representation of vibrational energy is often utilized in the quantum mechanical description of the crystal lattice's modes of vibration, analageous to the photon representation as a quantum of electromagnetic energy in QED.

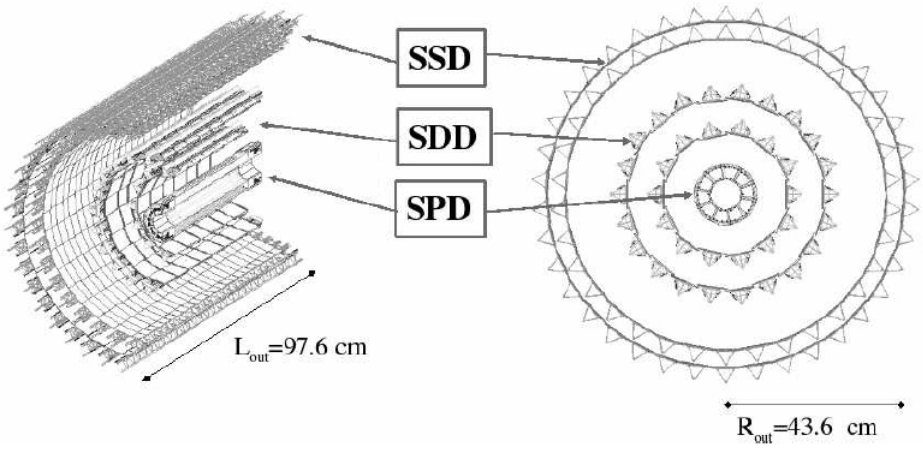

Figure 4.3: Figure showing a schematic diagram of the ITS with different layers labeled. The ITS layers of the illustration were produced with Geant-3. The figure was taken from [20].

application of the appropriate cooling and shielding of the detectors.

4.2.2 Specifications and performance

The ITS is comprised of three subdetector modules, the *Silicon Pixel Detector* (SPD), the *Silicon Drift Detector* (SDD), and the *Silicon Strip Detector* (SSD). The two inner layers comprise the SPD, the two next layers the SDD, and the two outer layers the SSD. The ITS covers the entire azimuthal range and $|\eta| < 0.9$ for all vertices within the interaction diamond ($\pm 5.3\ cm$ in z). The inner most layer of the SPD covers an extended range of $|\eta| < 1.98$ so as to provide continous coverage for the charge particle multiplicities in conjunction with the FMD. The radii values for the different layers, along with the number of read-out channels, are given in table 4.1. See figure 4.3 for an illustration of the configuration of the ITS layers in ALICE [20].

The material budget of the ITS was kept low to ensure accurate measurements in the calorimeters, and as not to impend a significant deflection of the particles emerging from the IP. A measurement of the material budget was done and found to be approximately 7.26 % X_{rad}. The thickness of the sensors in each layer ranges from 200-300 μm, and was chosen based on the need to both limit the multiple scattering of the incident particles and ensure a good signal to noise ratio. The SDD and the SSD have analogue read-out allowing for PID of particles with momenta below 200 MeV/c [20].

The spatial resolutions of each of the subdetectors of the ITS are given in table 4.2. The momentum resolutions measured by the ITS was found to be better than 2%, for pions with momenta in a range of 0.1–3 GeV/c.

Layer	Type	r(cm)	$\pm z$(cm)	Area(m^2)	Channels
1	pixel	3.9	14.1	0.07	3 276 800
2	pixel	7.6	14.1	0.14	6 553 600
3	drift	15.0	22.2	0.42	43 008
4	drift	23.9	29.7	0.89	90 112
5	strip	38.0	43.1	2.20	1 148 928
6	strip	43.0	48.9	2.8	1 459 200

Table 4.1: Table listing a few geometrical specifications of the ALICE ITS detector layers, including the number of read-out channels. The table was adapted from [20].

Parameter		SPD	SDD	SSD
Spatial resolution $r\phi$	(μm)	12	35	20
Spatial resolution z	(μm)	100	25	830
Two track resolution $r\phi$	(μm)	100	200	300
Two track resolution z	(μm)	850	600	2400

Table 4.2: Table listing spatial resolutions of the subdetectors of the ALICE ITS. The table was adapted from [20].

4.3 TPC - The Time Projection Chamber

The TPC is the main tracking chamber of the ALICE experiment. Its goal is to provide high resolution tracks with a good two track separation over a large volume. It is designed to operate with a charged particle multiplicity of up to 8000 per unit rapidity at mid-rapidity. The TPC's capabilities also include PID by utilizing the dE/dx measurements in conjunction with the momentum measurements obtained from the curvature of the trajectory, due to the applied magnetic field. The working principle and a few key characteristics and resolutions pertaining to the TPC will be outlined below.

4.3.1 Working principle - Gaseous detectors

The TPC is comprised of a large gas-filled drift volume, where the projected positions of the traversing particles are determined by the Multi-Wire Proportional Chambers located in its end-caps. This, along with the measured drift time of the ionization-liberated electrons, yields the 3–dimensional position where the incident particle ionized the gas. We will first present the physical principles of the Multi-Wire Proportional Chamber, before we discuss the Time Projection Chamber as a whole.

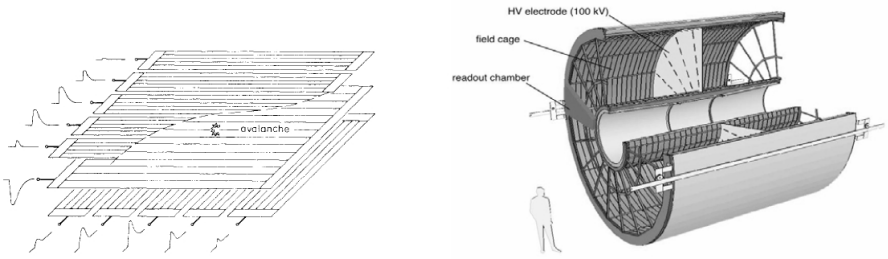

(a) (b)

Figure 4.4: Figure showing illustrations of; (a) the signals induced in a MWPC, (b) the layout of the ALICE TPC. The figures were taken from [46, 35] respectively.

MWPC - The Multi-Wire Proportional Chamber

The Multi-Wire Proportional Chamber (MWPC) is a hermetically sealed gas filled chamber, with numerous anode wires arranged in either a grid or a parallel configuration between two cathode planes. An elecric field is produced in the detector by grounding the cathodes and operating the anodes at positive potentials. The MWPCs were originally designed to cover large areas, with typicall values for the intermediate spacing of 2 mm between anodes and approximately 7–8 mm between the anodes and cathode planes respectively [18]. This arrangement will lead to a nearly homogeneous electric field throughout the detector, apart from in the near vicinity of the anodes wires, where the 1/r dependence of the nearest anode's contribution to the electric field will dominate over that from the neighboring anodes.

An incident charged particle will ionize the gas, as described in section 4.1, and the electrons and ions will drift towards their closest anode and cathode respectively. Due to the radial dependence of the electric field near an anode, the electron will be increasingly accelerated as it approaches its closest anode wire. If the operating potential is high enough, the electron may gain enough energy to ionize the gas further, resulting in additional electron-ion pairs. These subsequent electrons will also drift towards the anode gaining enough energy so that they too may cause further ionizations of the gas molecules around the anode. This electron multiplication process is often termed an avalanche, and the formation zone of the electron-ion pairs will have a drop-like shape as the ions have a lower mobility, and therefore a slower drift velocity than the electrons. The avalanche will only occur in the near vicinity of the anode wires, typically within a few radii of the anode wire [18]. The drifting electrons and ions will in turn induce an electrical current in the anode wire, where the amplitude of the signal will be directly proportional to the energy deposited in the detector by the incident particle. It is shown in [18] that the main contribution to the induced signal

on the cathode is due to the drifting ions.

The electrons liberated in an avalanche are rapidly collected at the anode, leaving behind a slow drifting ion cloud. The ions will thereafter induce an electrical current on the cathode planes, where the spatial position may be determined through the application of *the center of gravity method* on the observed current amplitudes [18]. To obtain high spatial resolutions, the cathode planes may be divided into pads resulting in a higher granularity of the spatial read-out.

The multiplication factor, or gain of a MWPC, is largely dependent on the choice of fill gas and the radii of the anode wires, along with the anode-cathode geometry. Typically, the choice of fill gas falls on a noble gas, or a noble gas-mixture, due in part to their low electron affinities and their ability to operate at high gains without suffering an electric discharge. The electron affinity and purity of the fill gas is particularly important when the ionized particles must drift a long distance before reaching the anodes. The mean-free path of the liberated electrons in the gas must be kept above the maximum drift distance, to ensure a sufficient detection efficiency and maintain its proportionality to the energy deposited by the incident particle.

The Time Projection Chamber

A TPC is a large hermetically sealed cylinder located symmetrically around the IP. The ALICE TPC is approximately 5 m in length with a diameter of 5 m. The inner radius of the active region is 85 cm and the outer radius is 250 cm. The TPC is essentially a large, gas filled, drift volume where the spatial position of the traversing particles are read out by the MWPCs located in its end-caps. A central electrode operating at a high potential relative to the end-caps results in a strong electric field in the direction parallel to the beam axis. As particles originating from the IP traverse the drift region in the TPC, they ionize the gas molecules, upon which the electric field will cause the electrons to drift towards the end-caps. The z-coordinate of the primary ionization may be found by measureing the drift time from when the ionization occured, until the signal is produced by the MWPCs. With the measured drift time Δt and with knowledge of the drift velocity of the electrons, one may calculate the distance that the electron traveled, thereby yielding the z-coordinate of the track. To assure an accurate calculation of the z-coordinate, it is vital that the drift velocity of the particles remains constant along the drift path of the TPC. As the drift velocity is directly proportional to the strength of the electric field, one must maintian a constant electric field throughout the drift region to gaurantee such a constant drift velocity, see equation (4.10), where $v_{\vec{e_{drift}}}$ is the velocity of the electron, μ is there mobility, and $\vec{E}$ is the electric field.

$$\vec{v}_{e_{drift}} = \mu\vec{E} \tag{4.10}$$

Due to the potential large drift distances in the TPC, a decrease in spatial resolution is expected as a result of diffusion of the drifting electrons. However, a magnetic field (with a magnitude of 0.5 T in ALICE) in the direction parallel to the electric field serves as a partial remedy. Since the magnetic field is parallel to the electric field, there will be no transverse component of the Lorentz force acting on the electrons drifting in the direction of the field lines of the electric field, see (4.11). However, as the electrons start to diffuse, the magnetic field will cause the electrons to revolve around the magnetic field lines, thereby minimizing the diffusion and loss in resolution.

The magnetic field also serves another purpose in the TPC. As charged particles from the IP traverses the subdetectors of ALICE, the Lorentz force will cause the particles to curve their trajectory in the x-y plane. By calculating each particle's radius of curvature, with knowledge of the particle's mass, will then allow for the determination of its momentum, see (4.12), where q is the charge of the particle, $\vec{E}$ is the electric field, $\vec{v}$ is the particle's velocity, and $\vec{B}$ is the magnetic field.

$$\vec{F}_{lorentz} = q\left[\vec{E} + \left(\vec{v} \times \vec{B}\right)\right] \tag{4.11}$$

$$R_{curvature} = \frac{p}{qB} \tag{4.12}$$

4.3.2 Specifications and performance

The end-caps of the TPC are each divided into 18 trapezoidal sectors with each sector separated into 6 partions. The end-caps are lined with MWPCs, with anode wires in a grid formation and with cathode pad read-out. Due to the radial dependence of the particle densities, two types of MWPCs with different dimensions are utilized along the radial direction to ensure sufficient resolutions. The MWPCs with the highest spatial resolution and two-track separation are positioned closest to the ITS, where the particle densities are higher. In total, the TPC is read-out by ∼560 000 cathode pads. The TPC operates with an efficiency for track finding above 90% and an efficiency for track matching with the ITS in the range of 85–95%, depending on the transverse momentum of the track [35, 10]. Further, the TPC is capable of providing full length tracks for particles within a range of $\eta < |0.9|$. The choice of fill gas (Ne/CO_2 at a ratio of 90/10) was based on the needs for a gas with low diffusion characteristics, stable drift speeds, durability against ageing, compatibility with high operating gains, and small cross sections for electron capture to ensure high efficiencies.

The central electrode is made of stretched aluminized Mylar foil with a thickness of 22μm operating at a potential of 100 kV above the anode wires. To ensure a constant drift speed, additional aluminized Mylar foils are wrapped around the support rods of the TPC near the inner and outer

Parameters	Specified values
Pseudo-rapidity coverage	$\eta < \|0.9\|$ for full radial track length
	$\eta < \|1.5\|$ for 1/3 radial track length
Radial position (active volume)	$848 < 2466\ mm$
Radial size of TPC (outer dimensions)	$606.5 < 2780\ mm$
Radial size of TPC (inner dimensions)	$788 < 2580\ mm$
Length (active volume)	$2 \times 2500\ mm$
Detector gas	$Ne/CO_2/N_2$ (90/10/5)
Drift field	$400\ V/cm$
Operating potential of central electrode	$100\ kV$
MWPC's anode-to-cathode spacing	2–3 mm (inner–outer MWPCs)
Total number of readout pads-channels	557 568
Spatial resolution in $r\phi$	1100–800 μm (inner–outer radii)
Spatial resolution in z	1250–1100 μm (inner–outer radii)

Table 4.3: Specifications of the ALICE TPC. The table was adapted from [20]

radii. These Mylar foils are operated at different electric potentials, ensuring a homogeneous electric field in the drift region of the TPC. The mobility of the electrons in a gas is strongly dependent on the operating temperature, and the drift speed is directly proportional to the mobility, see equation (4.10). To maintain a constant drift velocity, ALICE will operate the TPC with a constant temperature within an interval of $\Delta T \leq 0.1$ K [20].

A grid wire gate is positioned between the MWPCs and the drift region. The gate is opened on the arrival of a L1 trigger signal from the CTP, and subsequently closed after one drift cycle of $\sim$88 μs. The gate is designed to prevent the ions produced in the avalanches from drifting back into the active region of the TPC, which would in turn disrupt the electric field causing an unwanted change in the drift velocity. The TPC has incorporated a built-in laser and mirror system that can produce straight tracks in the active region through a two-photon absorption process [20]. These straight tracks may then be used for alignment and calibration purposes of the TPC. The TPC has a spatial resolution in $r\phi$ of 1100–800 μm from inner to outer radii and 1250–1100μm in z. See table 4.3 for further specifications of the operating characteristics pertaining to the TPC.

Chapter 5

Software environment

As has been described in the previous chapters, photon detection is an important aspect of studying ultra-relativistic collisions. The goal of the work leading to this thesis has been to analyze the potential of a high p_t photon trigger to be used with the HLT. This chapter will focus on the software frameworks and environments encountered in this analysis.

5.1 Software packages

The different software packages encountered during the analysis will be briefly described in the present section. Further, all of the software packages were run on a Unix-based operating system.

5.1.1 Root

Root is an object-oriented programming and library framework developed at CERN and written in C++. It was designed to aid in the analysis of particle physics, and has since been adopted by many other fields as well. The Root framework is organized in a hierarchical layer of classes, where one of the goals were to limit the need for the programmer to reproduce the same portion of code for every application, such as the detector geometry. The Root framework allows for simulating data through the Monte Carlo method and has embedded a number of mathematical and visual tools needed for the analysis of both real and simulated data. Some of the tools include the mathematical and statistical libraries and functions needed in many scientific experiments. It also provides GUI based graphical displays and various different histogram classes, such as an event display and 2-D contour and scatter plots, to name a few.

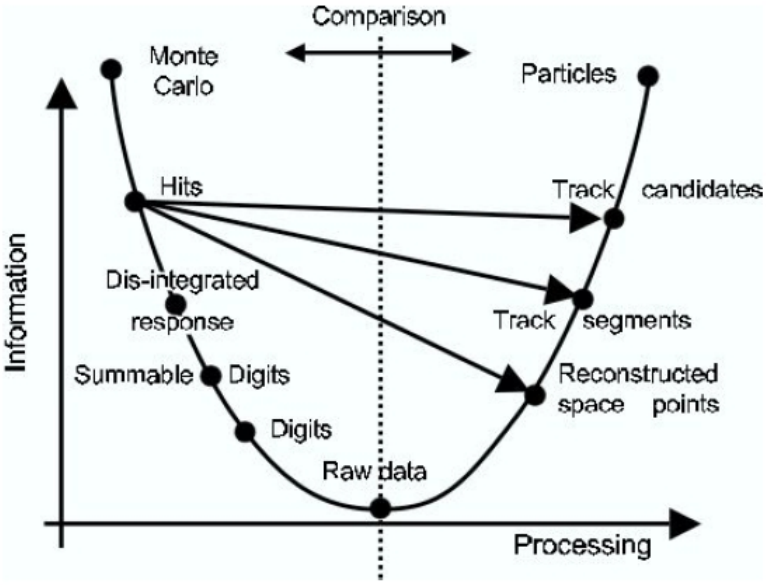

Figure 5.1: Figure showing data processing scheme of Aliroot event reconstruction. The figure was taken from [47].

5.1.2 Geant

Geant is a FORTRAN based software package enabling the transport of simulated particles through the specified detector modules. Geant performs the transportation of the particles through Monte Carlo simulations in conjunction with the loaded libraries of the detector geometry, along with the specified decay channels provided by the event generator. Geant versions up to and including Geant3 are written in FORTRAN. However, the most recent version has been entirely rewritten in C++.

5.1.3 Aliroot

Aliroot is an ALICE specific object-oriented software framework written in C++ and developed with Root as its foundation. It incorporates the simulation, reconstruction, and analysis frameworks pertaining to the ALICE experiment, such as the detector geometry and response, the trigger configurations, the HLT framework, and the analysis classes. Aliroot is utilized in the reconstruction of real and simulated events within the ALICE detectors. It was developed with focus on modularity allowing the framework to evolve along side its requirements, without the need for timely and drastic changes to the bulk code of the framework, and with simultaneous focus on the backward compatibility of new additions and changes in the already existing code.

A basic illustration of the Aliroot data processing scheme is shown in

figure 5.1. After the event generators have produced a set of particles, the transport framework propagates them through the detector while simulating energy depositions along their path. The localized energy deposits are called *hits*. They contain, in addition to the energy deposited, the information about the particle which produced them, such as momentum and PID. In the next step the tracks are dis-integrated leaving only the hits which carry the Monte Carlo information. The detector response is simulated with the hits as input and produce the digits. The are two types of digits, summable digits (sdigits) and digits. The sdigits are additive and utilized for event merging, where a signal event is embedded in an underlying event. The digits are produced either from the sdigits, in the case of event merging, or directly from the hits in the detector. They are produced with the real threshold levels and include the simulated noise in the detector. The digits may then optionally be converted into raw data where the data is stored in binary format, equivalent to the data format produced by real events. The digits, however, store the Monte Carlo information of the original simulated particles, whereas the raw format does not. The reconstruction of the event may take the digits or raw files as input, both real or simulated, depending on the users needs and specifications [47].

5.2 The Aliroot simulation framework

The Aliroot simulation framework allows for the simulation of particle and nuclei collisions at various energies. One may simulate realistic events based on the current understanding of physics, or one may simulate highly contrived events which allow for specialized tasks, such as testing new tracking algorithms or determining the sources of inefficiencies. A general overview of the simulation framework will be outlined in the present section.

5.2.1 Event generators

Event generators produce the particles in a simulated event that are propagated through the detectors by the transport Monte Carlo, e.g., Geant. There are a number of different event generators compatible with the Aliroot framework, where the choice of generator is governed by the needs of the user. Some generators may produce particle spectra equal to the expected spectra produced in real events, such as in p-p or Pb-Pb collisions, and others allow for the explicit production of rare signals and processes. However, this section will only focus on the generators used in the simulations relevant to the results presented in this thesis.

The event generators allow the user to specify a number of different characteristics pertaining to the produced particles, such as the position of the production vertex, their range in momenta, and their spatial distribution

(ϕ, η, θ). The *GenBox* and *GenFixed* generators also let the user explicitly specify the number and type of particles to produce for every event. The *GenFixed* generator produces the particles with a fixed momentum, where the momentum may be directly specified, or if a range in momentum is given, the generator will randomly pick one value within the range and produce all particles with that specific momentum. The *GenBox* generator produces the particles with momentum randomly distributed within a specified momentum range.

Pythia

PYTHIA is an event generator developed to simulate p-p collisions. It has been designed to produce a realistic particle spectra comparable to that produced in real events, within the boundary of the current understanding of physics. It also includes a number of features allowing the user to produce highly customized events. The user may set the basic variables as the generators above, such as collision energy, vertex position, momenta and spatial distributions. However, PYTHIA also allows the user to specify and alter the decay channels, either enhancing the probability of interactions or removing them completely. PYTHIA is often used in the simulation of minimum bias events and event merging of underlying events, for instance, jet production with a specified range of transverse energy merged with underlying minimum bias p-p collisions [48]. It should be noted that the other generators listed above use the PYTHIA decayer and may therefore also force decays during the simulation.

Cocktails

Cocktail generators like the *GenCocktail* allow for the simulation of highly customized events through the combination of different generators. This lets the user simulate rare events at higher rates than in the realistic generators. This is often utilized to simulate rare signals over realistic underlying events. It thereby reduces the time and computer resources required in simulating the rare events and their subsequent analysis, while maintaining sufficient statistics.

5.2.2 Configuring the simulation

The configuration macro, often called *Config.C*, is written in C++ and must be processed before the actual simulation may start. The configuration creates the specified Monte Carlo object, the event generators, and the detector geometry. It also creates a virtual Monte Carlo object that interfaces to the transport code, which translates the FORTRAN user code of Geant 3 into C++. Further in the configuration file, the user may set the magnetic field map of the detectors and which event generator, or Cocktail of generators,

that should be incorporated in the simulation, including the option to force decays or remove decay channels in their entirety. The user may also specify the type and energy of the colliding particles, the centrality range of the collisions, the specific particle species produced, and in addition, the particles' spatial distribution, their momentum range, and their mutual production vertex within a given sigma. It also allows the user to specify which of the subdetectors that should partake in the reconstruction. Thereby, speeding up the reconstruction process if only interested in the response of a few detectors.

5.2.3 Running the simulation

The simulation macro initiates the configuration and runs the actually simulation through the creation of an *AliSimulation* object. The user must specify the number of events to simulate and may optionally merge them with other signal or underlying events, stored in a different directory through the *AliSimulation* function *MergeWith("location of underlying events","Number of signal events per underlying event")*. Further, the user may specify which detectors should produce *sdigits* and which should produce the *digits* directly from the *hits*. This is done with two different *AliSimulation* functions where the arguments signal the detectors, namely *SetMakeSdigits("A space separated list of detectors")* and *SetMakeDigitsFromHits("A space separated list of detectors")*. The user may also specify the creation of raw data form the digits through the method *SetWriteRawData()*, which accepts three arguments, the first specifies which detectors it should create the raw data for by calling the method *Digits2Raw()* on each of the specified detectors, the second argument specifies the file name in which the raw data should be stored, and the last argument signals whether the intermediate files produced in the conversion should be deleted. An example of creating raw data for all of the detectors during a simulation could be *SetWriteRawData("ALL","raw.root","kFALSE")*. Finally, the simulation process itself must be initiated by the *AliSimualtion* function *Run("Number of events")*, which takes as arguments the number of events to simulate.

5.3 The Aliroot reconstruction framework

The Aliroot reconstruction framework allows for the reconstruction of both real and simulated data, utilizing digits or raw data as inputs. The general layout of the event reconstruction procedure will be briefly outlined below.

5.3.1 Running the reconstruction

The reconstruction macro initiates the event reconstruction through the creation of an object of the class *AliReconstruction*, and the subsequent calling

of its *Run("Number of events")* function. The default input is the digit format, however, the user may specify raw data as input through the function *SetInput("raw data root type file name")*. The user may also specify a subrange of events to reconstruct through the function *SetEventRange("first event, last event")*. If a range is not specified, the reconstruction will reconstruct every event. The local reconstruction may be controlled through the function *SetRunLocalReconstruction("A space separated list of detectors")*, where the user can specify which detectors should partake in the reconstruction.

5.3.2 Event reconstruction

To aid in the discussion of event reconstruction one may typically define some relevant terminology, where we define the following terms as described in [47]:

- **Digits:** A digit is the digitized signal produced by the detector from the energy deposition of a particle traversing the active region, at a specific location in space and time.
- **Clusters:** A cluster is a collection of adjacent digits that are thought to have been produced by the same particle.
- **Space points:** A space point may be determined by the center of gravity method on the induced read-out signals. The space point reflects the estimated point at which the particle passed through the sensitive region of the detector.
- **Tracks:** The track represents the reconstructed trajectory of the particle that traversed the detector.

The reconstruction process typically starts with local clusterization of the hits in each of the subdetectors independently. The primary vertex is subsequently estimated utilizing the two inner layers of the ITS (SPD). After which the tracks are reconstructed, and in conjunction with the combined response of the detectors; the PID, the energy, the momentum, and other valuable characteristics are determined and stored. The tracking procedure is handled differently in the off-line and on-line reconstruction due to their different timing requirements. The tracking efficiencies and processing time needed for the different tracking procedures are given in table 5.1. The different methods will be outlined below.

5.3.3 Off-line - tracking

The off-line tracking procedure utilizes an Kalman filter approach, where the tracking starts at the outer radius of the TPC where the tracklet seed

p-p collisions at $\sqrt{s} = 14\ TeV$		
	Time	Efficiency
Offline	66.0 μs	99.94 %
HLT	19.6 μs	99.86 %

Pb-Pb collisions at $\sqrt{s} = 5\ TeV$		
	Time	Efficiency
Offline	160.1 s	95.84 %
HLT	17.6 s	98.15 %

Table 5.1: Performance of the Offline and the HLT trackers on simulated p-p and Pb-Pb events at $\sqrt{s} = 14\ TeV$ and $\sqrt{s} = 5\ TeV$ per nucleon pair respectively. The tables are comprised of data acquired from [49].

densities are low. A seed is a small combination of clusters that pose as promising track candidates. Not all clusters are viable candidates as some may have been produced from noise in the detector or inefficiencies in the cluster finder algorithm. The tracks are prolonged inwards towards the inner radius of the TPC by appending the additional clusters to the tracklet through the Kalman filter algorithm. Further, the TPC track is propagated to the outer radius of the ITS and further to the preliminary primary vertex. The next loop starts at the primary vertex and follows the track radially outwards removing the cluster-outliers with large χ^2, and for proposed primary tracks estimating their PID for the ITS and TPC tracks. At the outer radius of the TPC the tracks are propagated to the TRD, where it further continues appending clusters, and undertakes a propagation to TOF, PHOS, and the HMPID. The third step starts from the detectors furthest away from the beam axis, in the case where all of the detectors are selected for the reconstruction this will be the HMPID. It then follows the tracks radially inwards towards the primary vertex and calculates their impact parameters. A correction to the primary vertex is now performed with the proposed primary tracks, where secondary tracks originating from the decays of secondary interactions are excluded, leading to a more accurate determination of the primary vertex.

5.3.4 On-line HLT - tracking

The HLT's on-line tracking algorithm combines a Cellular Automaton method (CA) and a Kalman filter method [50]. The Cellular Automaton method is reminiscent of the principles of John Conway's Game Of Life (GOL). If one envisions the detector volume as partitioned into 3-dimensional cells, in which a *hit* at the position of the cell is equivalent to the cell being alive. The principles used in the CA tracking method are presented in [51] and listed below, where here a cluster represents a collection of cells.

- **Starvation:** A cluster that doesn't have any living cells immediately above it dies.
- **Overpopulation 1:** A cluster in the immediate vicinity of a number of *clusters* outside the predetermined threshold dies.

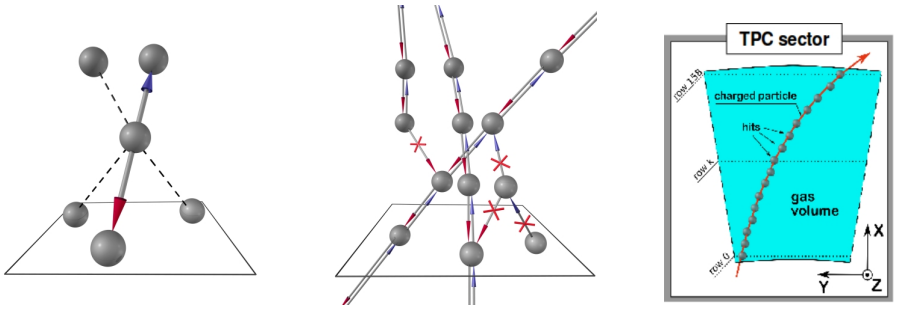

(a) Step.1 (b) Step.2 (c) Step.3

Figure 5.2: Figures depicting the on-line tracking procedure. (a) For each TPC cluster, one cluster in the rows above and below are combined to from the best line, (b) cluster-line segments are combined and non-reciprocal links are removed, (c) clusters are combined to form track-segments in the sector and looks for missing hits. The figures were taken from [49].

- **Overpopulation 2:** A cluster in the immediate vicinity of a number of *cells* outside the predetermined threshold dies.
- **Survival:** All of the other living cells remain alive.
- **Birth:** No new cells are created, contrary to GOL.

The CA method was chosen due to its compatibility with the high level of parallel processing required for HLT, allowing for a time efficient on-line event reconstruction. In addition, the CA method is suitable to be run with GPU hardware accelerators, which will further decrease the processing time by approximately an order of magnitude [50, 49]. The TPC end-plates are divided into 36 sectors, where each sector is further partitioned radially into 6 partitions. The cluster finder of the HLT tracker uses the CA method to find and combine clusters within a single partition and all 216 partitions are processed in parallel. The clusters from the six partitions belonging to one sector are then combined into track-segments within the sector. The *Global-Merger* subsequently merges all of the 36 sectors resulting in complete tracks within TPC volume. The next step merges the TPC and ITS tracks, upon which a Kalman filter track fitting procedure is implemented improving the fit by removing the outliers from the track. A general illustration of the CA method is depicted in figure 5.2.

5.3.5 ESDs and AODs

The output of the event reconstruction is stored in Event Summary Data files (ESDs) where the data is stored in a ROOT tree format of ESD objects. The ESD stores the information from both the off-line and the on-line

HLT reconstruction in their respective esd trees, namely the *esdTree* and *HLTesdTree*. The ESD files contain all the relevant information that could be needed for the subsequent analysis, such as track multiplicities, V0s, PID, momentum, cascade decays, and the number of participants. Further, the ESDs may be processed and filtered into Analysis Oriented Data files (AODs), where analysis specific cuts are implemented on the ESDs, such as p_t, multiplicity, etc. Thereby, limiting the resources needed to process and analyze the data not relevant to the user's analysis.

Chapter 6

Analysis

The operating scheme of the γ conversion trigger for HLT intended on using the *V0-Finder* component to search for eligible conversion candidates. Up until the beginning of 2011, the *V0-Finder* and the primary vertex finder were incorporated in a single component called the *Global-Vertexer*. In January of 2011, they were separated into two components, namely the *Primary-Vertex-Finder* and the *V0-Finder*. As a result, a portion of the work leading to this thesis entailed thoroughly testing and aiding in the debugging process of the new *V0-Finder* component, ensuring that it gave the same results as the old V0-finder housed in the *Global-Vertexer*. All results and distributions obtained with the *Global-Vertexer* prior to the incorporation of the *V0-Finder* component have been reproduced using the *V0-Finder*. All results pertaining to HLT's γ reconstruction through the conversion method and displayed in this thesis have been produced with the *V0-Finder* component.

The analysis of the *V0-Finder* was performed through the simulation and reconstruction of different types of events. The utilization of the Monte Carlo information allowed for the optimization of the V0-cuts, and the determination of the *V0-Finder's* respective efficiency and purity of the accepted sample of V0s. The software versions used in the event production and subsequent analysis were Root version v5-27-06b, Geant3 version 1.11, PYTHIA version 6.4.21 and Aliroot versions: v4-19-revision-12, v4-20-revision-04, and a continuously updated trunk version.

This chapter will outline the operating algorithm of the *V0-Finder*, the C++ macros developed to perform the data analysis, and the different types of events simulated, along with the obtained results and distributions. A V0 is generally defined as a secondary vertex, originating from a decay, or conversion, of a neutral particle into two charged daughter particles, i.e., $X^0 \rightarrow y^- + y^+$.

6.1 The V0-finder for the HLT

The *V0-Finder* is processed during the event reconstruction after the primary vertex is determined and the tracking is complete. The *V0-Finder* may take as input the ITS tracks, the TPC tracks from the *Global-Merger*, and the ESD tracks. The *V0-Finder* retrieves the primary vertex, and with the aid of their respective p_t, determined from their radius of curvature, the tracks are propagated back towards the primary vertex in order to calculate their respective impact parameters.

The *V0-Finder* checks that the primary vertex has at least 3 contributors before further processing the event. A contributor is defined as a reconstructed track, that has sufficient characteristics so that it may be used to determine the position of primary vertex. If less than three contributors, the *V0-Finder* ceases to process the event and no V0s are filled in the ESD. If the primary vertex has more than the two contributors, it initiates a nested loop processing the tracks in an attempt to find the two daughter tracks that originated from a γ conversion. The outer-loop, loops over all of the tracks looking for negatively charged tracks, and for every negatively charged track found, it checks that its impact parameter with respect to the primary vertex is larger than the predefined value. It then enters the inner-loop and loops over all of the tracks looking for positively charge tracks, and for every positively charged track found it ensures that its impact parameter is larger than the specified value. Further, it calculates the *Distance of Closest Approach* (DCA) between the two tracks and ensures that it is smaller than the set value.

In the next step, it creates a particle representing the V0 from the two tracks with an assumption on their respective particle type, in this case an electron and a positron. Further, a boolean flag is required in the creation of the V0 indicating if it should be created as a γ or not, since the γ requires its own specific constructor due to its zero mass. Next, the *V0-Finder* checks that the χ^2 of the V0 particle is larger than zero and smaller than a preset value. The maximum allowable value in the χ^2-cut is computed by multiplying the square of the DCA-cut value and the number of degrees of freedom of the V0. It is thus an implicit cut determined by the user specified value of the maximum DCA [1].

Next, a copy of the primary vertex is created and it checks if the negative and positive tracks were used in the determination of the primary vertex. If they were used, they are removed from the copy of the primary vertex, given that the remaining number of contributors are larger than one. Then, the V0 particle is propagated back towards the copy of the primary vertex

[1] It should be note that when comparing with χ^2 values for the off-line *V0-Finder* the χ^2 values from HLT may require a division by a factor four, as the χ^2 value is occasionally presented as χ^2/NDF, where NDF represents the number of the number of degrees of freedom used in the calculation.

and its impact parameter is calculated. If the impact parameter is below the specified value, the V0 is added to the copy of the primary vertex, which results in a more accurate determination of the primary vertex. The production vertex of the V0 is then subsequently set to the position of the modified primary vertex replica. Note however, that the original primary vertex remains unaltered through this process.

The last cut in the *V0-Finder* entails calculating the decay length, and error in the decay length, of the V0 particle. If the decay length is smaller than the error multiplied by a predefined value, the V0 will be rejected. Finally, if the tracks and the constructed V0-particle have passed all of the cuts, the V0 is filled to the ESD and the nested-loop continues until every possible negative and positive track combination has been explored by the *V0-Finder*.

6.2 Macros

The two main macros developed to aid in the analysis of the *V0-Finder's* capabilities are a partial reconstruction macro and an analysis macro. The partial reconstruction macro was developed to speed up the process of observing the effects of applying a different set of cuts to the *V0-Finder* for the reconstruction of the simulated events. The analysis macro was developed to further process and analyze the accepted V0s stored in the ESDs. A general overview of the macros will be given in the current section. The complete C++ code may be viewed at 'https://it.uib.no/ tso043'.

6.2.1 Reconstruction macro

As mentioned above, the partial reconstruction macro was developed to speed up the reconstruction of the events after a new set of cuts were implemented in the *V0-Finder*. The macro was developed with significant help and guidance from Ph.D. Matthias Richter and Ph.D. Kalliopi Kanaki. The macro utilizes the *AliHLTSystem* which allows for a partial reconstruction of the events through specifying which components that should process the input data. This is done through the creation of *AliHLTConfiguration* objects, which are linked together in a reconstruction chain. It was then possible to speed up the reconstruction process, by for instance skipping the tracking procedure, as the tracks would be unaltered by implementing a different set of cuts in the *V0-Finder*.

The reconstruction macro specifies the name of the ESD root file that should be used as input, along with either the off-line or the HLT *esdtree*. The specified components load the ESD file and removes the primary vertex and V0s from the events, before publishing the data to the *Primary-Vertex-Finder component*, where the information required by the *V0-Finder* is determined, such as the primary vertex. Further, the output from the

Primary-Vertex-Finder is merged with the data read from the ESD file, with the original vertex and V0s removed. This is then fed as the input to the *V0-Finder* component where the V0 candidates are determined, as described in section 6.1. The output from the *V0-Finder* component is then merged with the data from the original ESD file and the output of *Primary-Vertex-Finder*, and further converted and written to a new ESD file stored in the same working directory, leaving the original ESD file unmodified.

In order to avoid the need for hard-coding the cuts in the C++ code of the *V0-Finder* and the subsequent recompilation of Aliroot, the cuts were set utilizing the *makeComponentConfigurationObject.C* macro that stores the values of the cuts in an *Online Configuration Database* (OCDB) object, where the configuration object is loaded by the *V0-Finder* component during the event reconstruction.

6.2.2 Analysis macro

The analysis macro analyzes the V0s stored in the ESD files for the various sets of cuts used in the *V0-Finder*. The macro loads and reads the ESD files along with the MC information needed to perform the analysis. In order to speed up the simulation process, simultaneous simulations were performed in different directories, and a dedicated function in the macro handles the directory navigation ensuring that the correct events are processed.

The ultimate goal of the analysis macro was to map and optimize the performance of HLT's *V0-Finder* for the γ conversions application. This is represented by a set of plots for the efficiency and purity of the *V0-Finder* representing its capabilities in locating γ conversions within the ITS and TPC. In order to do so, it was necessary to define the constraints of a *detectable* γ *conversion*. Whether a γ conversion is detectable or not is determined by processing the Monte Carlo information utilizing the PDG codes of the particles and a set of geometrical cuts, as described below.

The Monte Carlo information from each event is processed in a separate function in the analysis macro, and those events with less than three contributors used to determine the primary vertex are skipped in accordance with the conditions of the *V0-Finder*. Next, a nested-loop is performed over every particle produced in the simulation. The outer-loop looks for electrons and checks that the electron is a secondary particle that was created by a γ conversion. In the inner-loop, it looks for positrons that are also secondary particles originating from a pair production process. Further it checks that the electron and positron originate from the same mother particle, where the mother must be a γ. It ensures that the production vertex of the γs' daughter particles are within the geometrical acceptance of the ITS and TPC detectors, namely $|x| < 250\ cm$, $|y| < 250\ cm$, $|z| < 250\ cm$, and $|\eta| < 0.9$. The η-range was chosen in accordance with the potential full track length requirement of the TPC, as described in section 4.3.2. In addition,

it ensures the radial distance from the beam axis is smaller than 180 *cm*, as a conversion occurring further out will result in the track lengths of the daughter leptons to be insufficient to be considered *good* tracks, due to their low number of clusters. If a γ conversion upholds all the aforementioned conditions, it is labeled a *detectable γ conversion*.

The V0s are processed in another stand-alone function operating with the same conditions as that of the Monte Carlo processing function. It too ensures that the number of contributors to the determination of the primary vertex are at least 3, before processing the V0s stored for the event. It loops over all the V0s in the ESD file for each event and creates two particles from the Monte Carlo labels retrieved from the daughter tracks of the V0. All the particles produced in the simulation are stored in an array, the Monte Carlo labels of a track represent the array index of the particle that produced the track. Further, it ensures that both particles are secondary and that they originated from the same mother, where the mother must be a γ. It retrieves the Monte Carlo label of the mother particle and checks it against the respective labels of all previously processed V0s, ensuring that the same γ conversion isn't counted twice. Due to a feature known as *track-splitting*, where one original track is reconstructed as multiple track segments, multiple V0s representing the same γ conversion may potentially be accepted by the *V0-Finder* and filled in the ESD file. Track-splitting most often due to inefficiencies of the cluster finder along intersections between two TPC sectors, or a track passing through the central electrode. This feature, if not accounted for would bias the accurate determination of the efficiency of the *V0-Finder*, along with the purity of the produced sample. Next, it checks that the mother has exactly two daughters, which must be an electron and a positron that were both produced from a γ conversion. Finally, it ensures that the production vertex of the daughters uphold the same geometrical limitations as that of the Monte Carlo processing function outlined above. If the V0 upholds all of the aforementioned conditions, the V0 is labeled a *detected γ conversion*.

The macro also includes other functions to aid in the analysis, such as its own V0 finder function for observing the trend of the efficiency and purity with a different set of cuts, without the necessity for running a full- or partial event reconstruction. However, all results and plots obtained from this analysis, and depicted in this thesis, were produced with the event reconstruction using the *V0-Finder* component, and not its replica in the analysis macro.

Further, a function dedicated to the determination of the energy and momentum resolutions of both the HLT-tracks and the V0s are incorporated in the macro. In addition, an attempt to observe how much the results of the *V0-Finder* analysis are biased by embedding γs to the underlying events is performed in the same function. This is done by plotting the charged multiplicities determined from the reconstruction of individual events with

and without γs embedded. Finally, a series of different plotting functions are called which display the efficiency, purity, and various different distributions, which will be presented in the following sections.

The efficiency of the *V0-Finder* may be defined as the total number of *detectable γ conversions* found, divided by the total number of *detectable γ conversions* produced in the event, see equation (6.1). The purity is defined as the number of V0s accepted by the *V0-Finder* ,after the addition of the geometric cuts, that are *detectable γ conversions*, where the contribution due to *track-splitting* has been subtracted, divided by the total number of V0s accepted by the same cuts, see equation (6.2).

$$\text{Efficiency} = \frac{\text{Number of detectable } \gamma \text{ conversions found}}{\text{Number of detectable } \gamma \text{ conversions produced}} \tag{6.1}$$

$$\text{Purity} = \frac{\text{Number of V0s accepted that are detectable } \gamma \text{ conversions}}{\text{Total number of V0s accepted}} \tag{6.2}$$

6.3 Pure γ and $\pi^{\pm}$ events

One of the first steps in the analysis of the *V0-Finder's* performance, was to determine whether it could in fact detect a γ conversion at all. In order to test this, a set of non-realistic events were simulated containing only γs. However, this resulted in a poor determination of the primary vertex, as all of its contributors were secondary particles. As a remedy, a few $\pi^{\pm}$ were added to aid in the determination of the primary vertex and an attempt to maintain the number of contributors in each event above two, in accordance with the conditions of the *V0-Finder*. The event parameters and results pertaining to these simulations will be outlined in the present section.

6.3.1 Event parameters

The simulation was performed with the *GenCocktail* particle generator, utilizing the *GenBox* and *GenFixed* generators for the production of the γs and $\pi^{\pm}$s respectively. One-thousand events were simulated and the decays were carried out by the PYTHIA decayer, with all decay channels open and at their respective default branching ratios, as provided by PYTHIA.

The position, along with the uncertainty in the position, of the production vertex was set to [0,0,0] for [x,y,z] respectively. A total of fifty γs were produced in each event in a momentum range of [0.5–20] GeV/c. The γs were randomly distributed within the ranges of $\eta < |0.9|$ and $0 < \phi < 2\pi$.[2]

[2] η is related to the θ angle by the formula: $\eta = -ln[tan(\theta/2)]$, where ϕ is the angle between the particles trajectory and the z-axis.

In addition to the γs, three π^{-}s and three π^{+}s were produced in each event in a momentum range of [0.5–10] GeV/c, and with the same range in η and ϕ as that of the γs. Further, only the ITS and the TPC detectors were initiated for event reconstruction, and the magnitude of the magnetic field was set to 0.5 T.

6.3.2 Results of analysis

The *detectable γ conversion* yield produced by Geant was obtained from processing the Monte Carlo information and was plotted against η, ϕ, and p_t, and is shown in figure 6.1. The η, ϕ, and p_t values of the HLT reconstructed tracks are also shown in figure 6.1. The plots in figure 6.1 have all been normalized by the total number of events in the processed data sample. Various sets of cuts for the *V0-Finder* were used in the reconstruction of the events. A selection of the cuts are given in table 6.1 and the average efficiency and purity of the *V0-Finder* pertaining to these cuts, determined in a p_t range for the γs of [0, 20] GeV/c, are listed in table 6.2.

Cut set Nr.1 corresponds to the initial default values set in the *V0-Finder* when this work began, and its efficiency in detecting the *detectable γ conversions*, along with the purity of the V0s accepted, is shown in figure 6.2 for η, ϕ, and p_t. The efficiency and purity distributions against η and ϕ were found to remain approximately flat throughout the aforementioned ranges for the different cuts applied to the data sample. Subsequently, the η and ϕ distributions will only be presented for cut set Nr.1. In order to obtain the value for the maximum achievable efficiency of the *V0-Finder* for these events, the reconstruction was run without the cuts implemented in the *V0-Finder*, and this cut set corresponds to cut set Nr.2 in tables 6.1 and 6.2. The efficiency and purity of cut set Nr.2 are shown in figure 6.4 (a) and (b), for p_t.

As every track combination of negative and positive tracks would be combined in the *V0-Finder* with cut set Nr.2 implemented, this allowed for the plotting of the distributions for the different cuts in the *V0-Finder*. By utilizing the Monte Carlo labels, the distributions could be produced in such a way that one histogram would represent the cut-values of the V0-candidate for the real *detectable γ conversions*, and one histogram would represent the values obtained from the combination of the tracks that do not originate from the same *detectable γ conversion*. The distributions are shown in figure 6.3, where the blue histograms correspond to the real conversions and the red histograms represent the fake conversions. With these distributions at hand, it was then possible to determine a more appropriate set of values for the cuts in the *V0-Finder*, for the γ conversion application. The goal was to maximize the acceptance of real conversions while minimizing the acceptance of the fake combinations.

The decay length cut is a remnant from the *V0-Finder's* application for

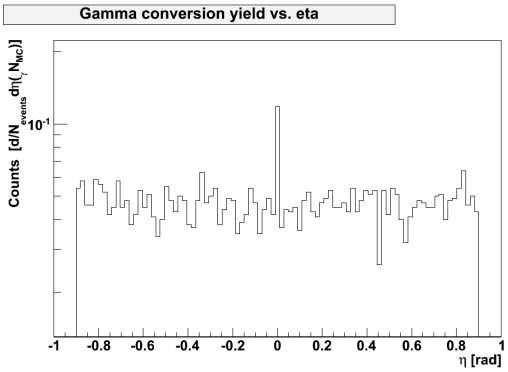

(a) Geant: γ conversion yields vs. η

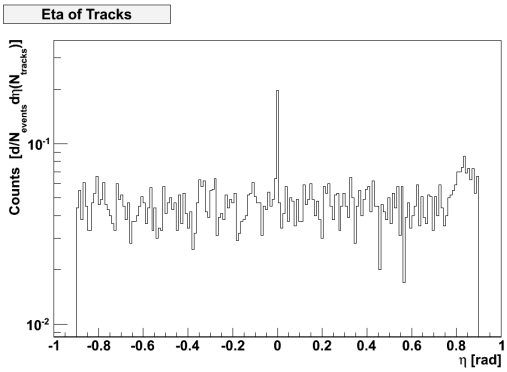

(b) HLT: Track multiplicity vs. η

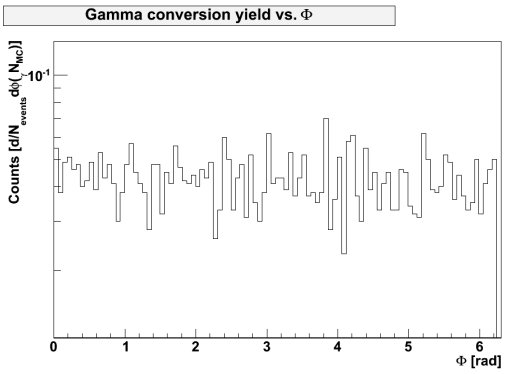

(c) Geant: γ conversion yields vs. ϕ

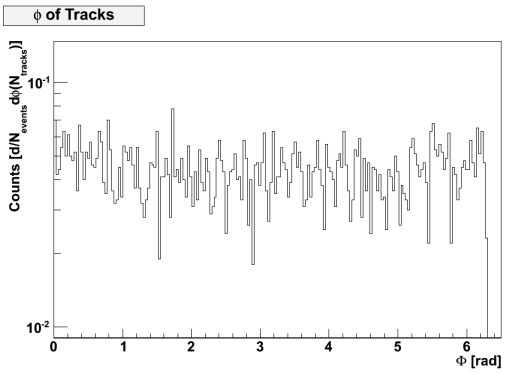

(d) HLT: Track multiplicity vs. ϕ

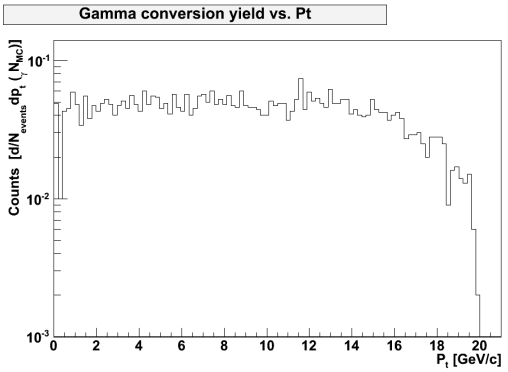

(e) Geant: γ conversion yields vs. p_t

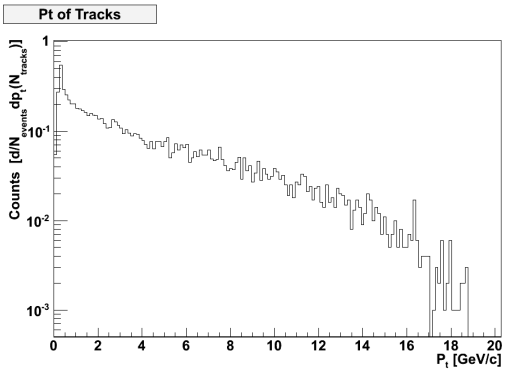

(f) HLT: Track multiplicity vs. p_t

Figure 6.1: Plots show the normalized **Geant** produced γ conversion yields and **HLT** reconstructed track distributions from one-thousand pure γ and $\pi^{\pm}$ events. Figures [a, c, e] show the respective conversion yields plotted against [η, ϕ, p_t], and figures [b, d, f] show the track distributions plotted against η, ϕ, and p_t respectively.

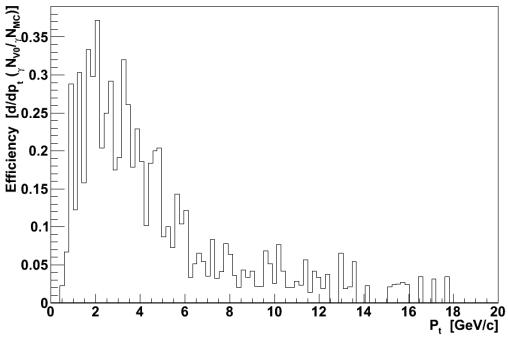

(a) Efficiency vs. p_t

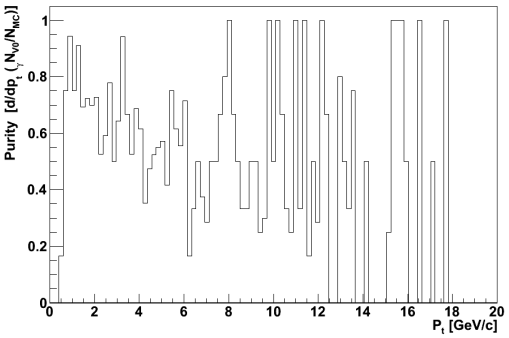

(b) Purity vs. p_t

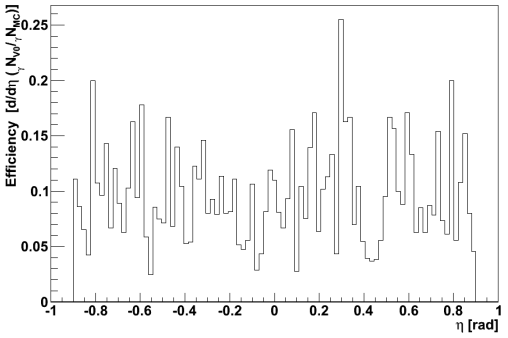

(c) Efficiency vs. η

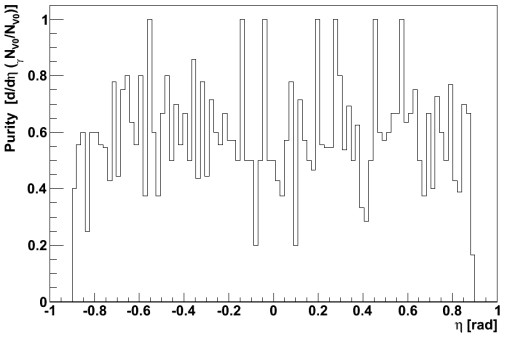

(d) Purity vs. η

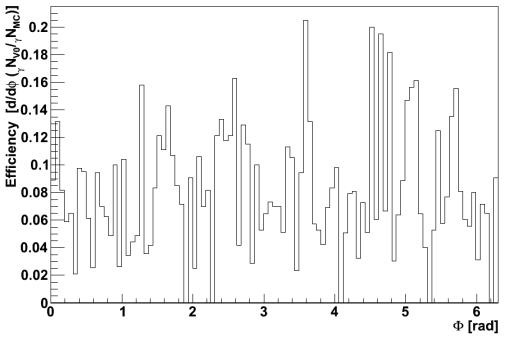

(e) Efficiency vs. ϕ

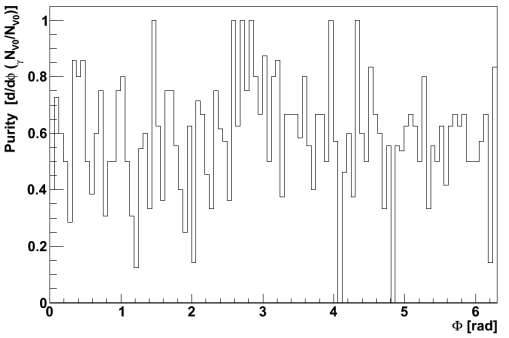

(f) Purity vs. ϕ

Figure 6.2: Figures show the efficiency and purity of the *V0-Finder* with cut set Nr.1, with **HLT** tracks as input, for one-thousand pure γ and $\pi^{\pm}$ events. Figures show: (a) Efficiency plotted against p_t of the γ, (b) Purity plotted against p_t of the γ, (c) Efficiency plotted against η of the γ, (d) Purity plotted against η of the γ, (e) Efficiency plotted against ϕ of the γ, (f) Purity plotted against ϕ of the γ.

Selected *V0-Finder* cut sets: Pure γ and $\pi^{\pm}$ events				
Cut set	Imp. Par.: Tracks	DCA	Imp. Par.: V0s	$L_{Decay}/\sigma_{L_{Decay}}$
Nr.1	2.5	3.5	3.5	3.0
Nr.2	—	—	—	—
Nr.3	0.04	20.0	60.0	0.1
Nr.4	0.01	5.0	15.0	0.0

Table 6.1: A selection of the cut sets used in the analysis of the γ conversion detection capabilities, of HLT's *V0-Finder* for the pure γ and $\pi^{\pm}$ events.

V0-Finder efficiency and purity for selected cut sets: *Pure γ and $\pi^{\pm}$ events*		
Cut set	Average efficiency	Average purity
Nr.1	7 %	45 %
Nr.2	55 %	14 %
Nr.3	45 %	17 %
Nr.4	50 %	81 %

Table 6.2: Table showing the average efficiency and purity values for the different sets of cuts for the HLT *V0-finder*, from the the pure γ and $\pi^{\pm}$ events.

other neutral decays which have characteristic decay lengths and lifetimes, such as the K^0_S. However, this cuts does not apply to the γ conversion application as a γ may convert anywhere in the vicinity of an electric field and is not governed by a characteristic lifetime. This was confirmed by the distribution plots, as can be seen from figure 6.3 (i) and figure 6.3 (j).

In an attempt to maintain a sufficient purity, and accept more of the real conversions, the decay length cut was set to 0.1 for cut set Nr.3. To ensure that a large portion of the real conversions were accepted by *V0-Finder*, relatively broad values were chosen for the impact parameter of the V0 cut and the DCA of the two tracks, and set to 60 *cm* and 20 *cm* respectively. A value of 0.04 *cm* for the impact parameter of the track was chosen to maintain a large acceptance of the signal, while simultaneously removing a portion of the peak from the fake contribution. The values of cut set Nr.3 are shown in table 6.1, and corresponding values for the efficiency and purity, as that of cut set Nr.1 and Nr.2, are shown in table 6.2 and figure 6.4 (c) and (d), for p_t.

The purity corresponding to cut set Nr.3 at ∼17 % was clearly too low to be deemed adequate for the γ conversion application, upon which further adjustments of the cuts were performed. The decay length cuts was set to zero as it removed too many of the real conversions. The values for the impact parameter of the V0 cut and DCA of the tracks were reduced, as

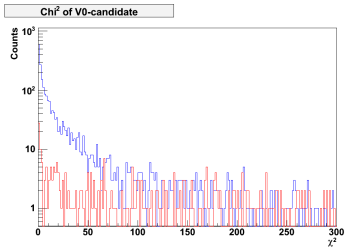

(a) χ^2 distribution

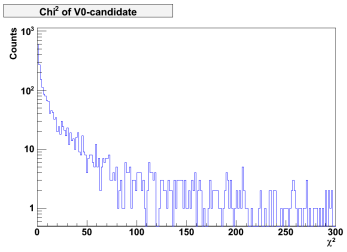

(b) χ^2 distribution

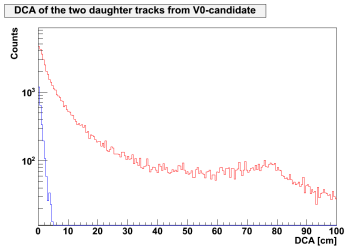

(c) DCA distribution

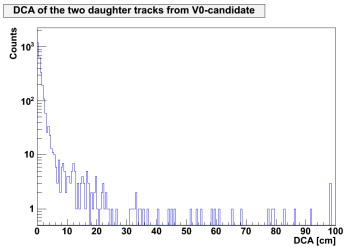

(d) DCA distribution

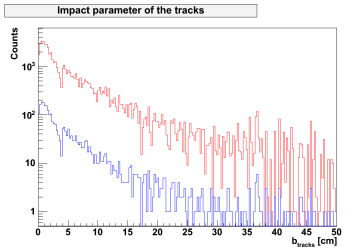

(e) Impact parameter of tracks

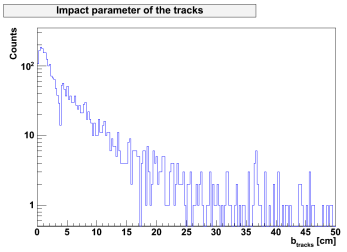

(f) Impact parameter of tracks

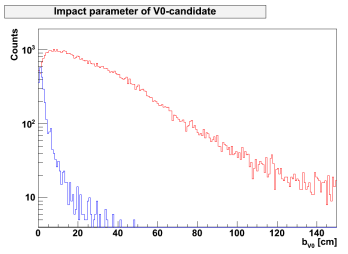

(g) Impact parameter of V0s

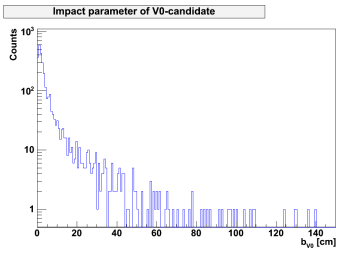

(h) Impact parameter of V0s

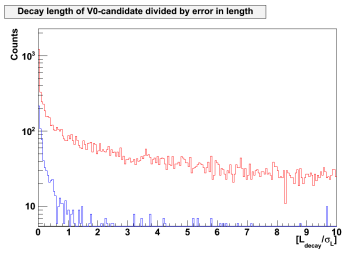

(i) Decay length cut

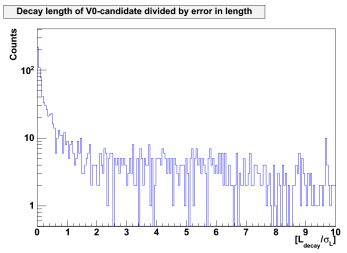

(j) Decay length cut

Figure 6.3: The figures show the cut distributions of every V0-candidate obtainable from the **HLT** tracks, for one-thousand γ and $\pi^{\pm}$ events. The blue histograms represent the real conversions, whereas the red histograms represent the fake conversions. Figures show (a, b) χ^2 distribution, (c, d) DCA between the two tracks, (e, f) impact parameter of the tracks (g, h) impact parameter of the V0-candidate, and (i, j) show the decay length divided by the error in the decay length.

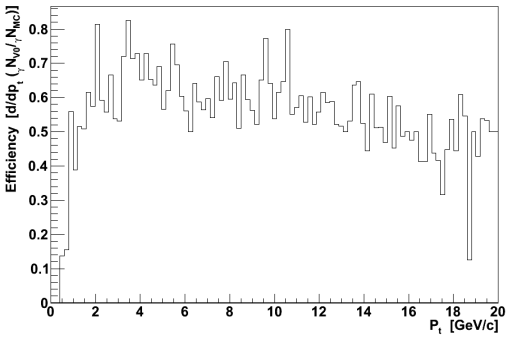

(a) Efficiency vs. p_t

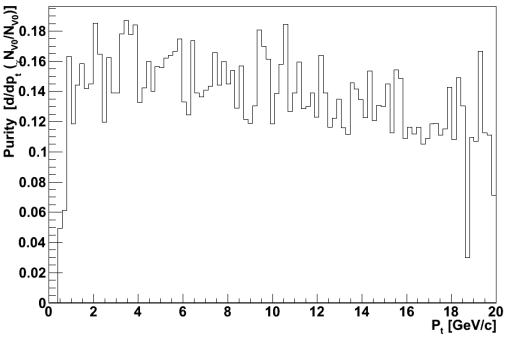

(b) Purity vs. p_t

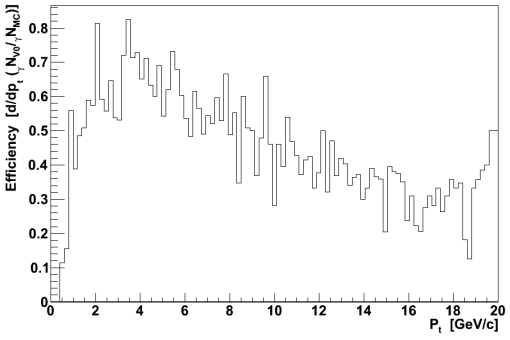

(c) Efficiency vs. p_t

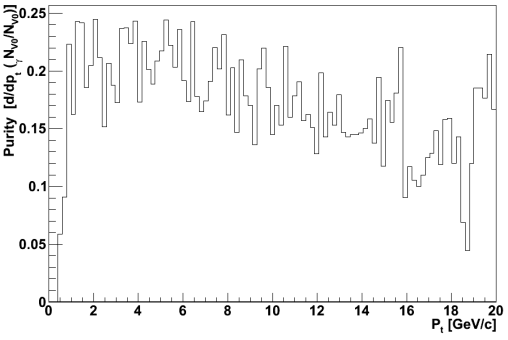

(d) Purity vs. p_t

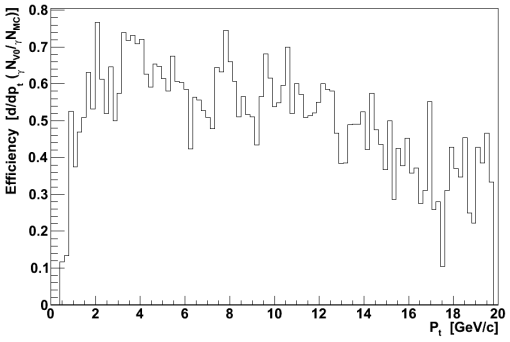

(e) Efficiency vs. p_t

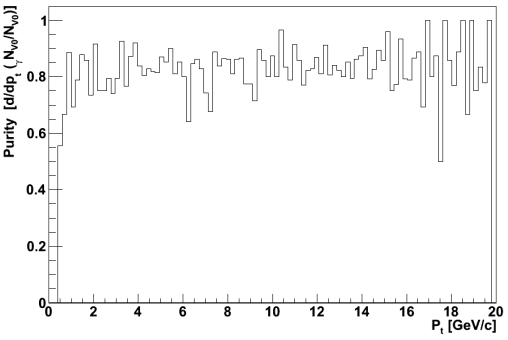

(f) Purity vs. p_t

Figure 6.4: Figures show the efficiency and purity of the *V0-Finder* with **HLT** tracks as input, for one-thousand pure γ and $\pi^{\pm}$ events. Figures show: (a) Cut set Nr.2: Efficiency plotted against p_t of the γ, (b) Cut set Nr.2: Purity plotted against p_t of the γ, (c) Cut set Nr.3: Efficiency plotted against p_t of the γ, (d) Cut set Nr.3: Purity plotted against p_t of the γ, (e) Cut set Nr.4: Efficiency plotted against p_t of the γ, (f) Cut set Nr.4: Purity plotted against p_t of the γ.

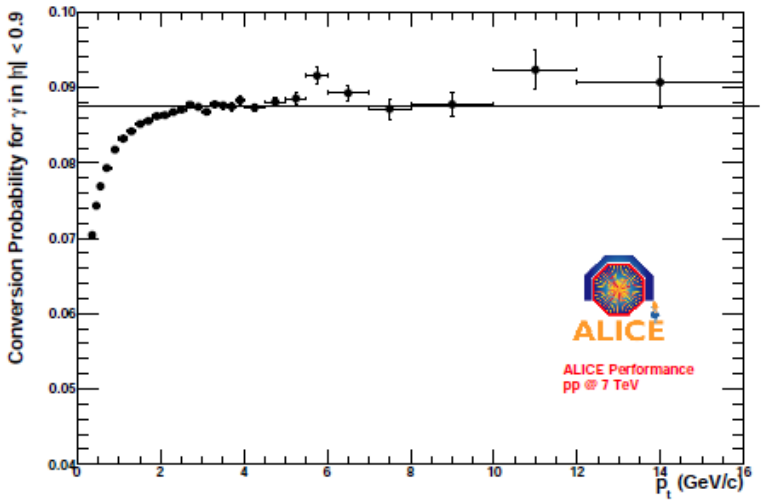

Figure 6.5: The measured photon conversion probability, plotted against p_t, from simulated p-p collisions at $\sqrt{s} = 7\ TeV$ per nucleon pair. The figure was taken from [52].

they accepted too many fake conversions. In addition, the value of the cut on the impact parameter of the track was reduced to accept more of the real conversions. Though many systematic adjustments of the cuts were performed during the analysis of these events, only the results from the final and optimal values have been incorporated in this section of the thesis. The optimal cuts are displayed in table 6.1 as cut set Nr.4. See table 6.2 for the average efficiency and purity, determined in a p_t range of [0, 20] GeV/c, and figure 6.4 (e) and (f), for the efficiency and purity plotted against the p_t of the γ, for the optimized cut set Nr.4.

6.4 Minimum bias p-p events doped with high p_t γs

From the pure γ and $\pi^{\pm}$ events, one could deduce that the *V0-Finder* was capable of locating γ conversions. However, since the pure events were highly contrived, the next step entailed the simulation of minimum bias p-p events embedded with a number of γs, providing a more realistic background to further analyze the *V0-Finder's* performance. This also allowed for further adjustments of the cuts in the *V0-Finder*, leaving the *V0-Finder* optimized for the γ conversion application for p-p collisions. The event parameters and results from the analysis of the events will be outlined in the current section.

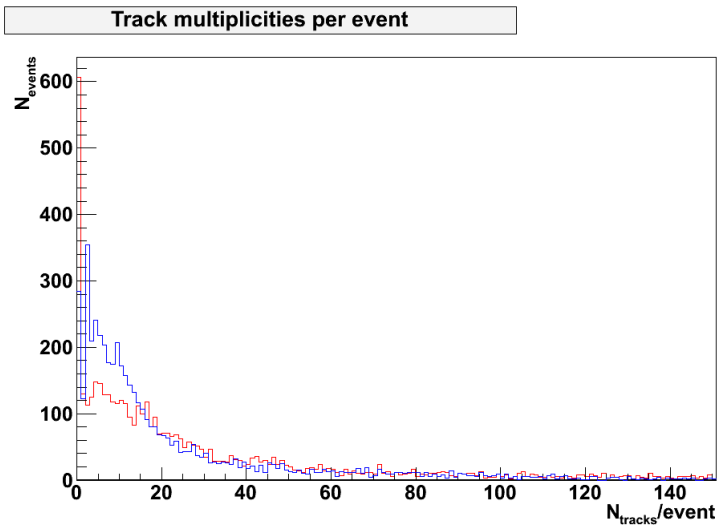

Figure 6.6: The figure shows the track multiplicity of five-thousand γ embedded and five-thousand non-embedded minimum bias p-p events at $\sqrt{s} = 14$ TeV per nucleon pair. The blue histogram corresponds to the charged multiplicities observed for five-thousand γ embedded p-p events, per event. The red histogram represents the charged multiplicities observed in five-thousand non-embedded events.

6.4.1 Event parameters

The simulation was performed utilizing the *GenCocktail* generator, combining the *GenPythia* and *GenBox* generators used for simulating the minimum bias p-p collisions and γs respectively. The event sample entailed the simulation of five-thousand minimum bias p-p collisions at $\sqrt{s} = 14$ TeV per nucleon-pair, embedded with ten γs per event. The conversion ratio of the γs in the specified momentum range has been found to be ∼7–10 %, see figure 6.5 [52]. After which, the number of γs were chosen in order to approximately embed one γ conversion per event. The decays of the particles were carried out by the pythia decayer, with all decay channels open and at their default branching ratios.

The production vertex was set to [0, 0, 0] for [x, y, z], with an uncertainty of [0, 0, 5.3 cm] for the respective coordinates. The p-p collisions were simulated in accordance with the minimum bias process and ranges of the *GenPythia* generator at $\sqrt{s} = 14$ TeV per nucleon pair. Ten γs were embedded into every event with a randomly distributed momentum in the range of [0.5–20] GeV/c, and within a range of $|\eta| < 0.9$ and $0 < \phi < 2\pi$. As with the pure events, only the ITS and TPC detectors were initiated for event reconstruction, and the magnitude of the magnetic field was set to 0.5 T.

In addition, five-thousand minimum bias p-p events were simulated with the same event parameters as that outlined above, however, without γs embedded. These additional events were simulated to see the how the embedding effected the track multiplicity of the events. Some change is expected as the interaction of γs will lead to additional tracks being produced in the detectors. The track multiplicity in both the five-thousand embedded and non-embedded events are shown in figure 6.6, where the blue histogram represent the events with additional γs embedded, and the red represents the charged multiplicity from the events without γs embedded. Different track distributions could lead to different results for the efficiency and purity, as the *V0-Finder* creates V0-candidates from track combinations. This must be kept in mind when comparing the acquired results to non-embedded or real events.

The ten γs may, to first order, introduce a maximum of twenty tracks to the event through the pair-production process, at these high energies the contribution from Compton scattering and the photoelectric effect may be ignored due to their small contributions. Although unlikely in comparison, it is possible that secondary processes of the conversion-produced electrons and positrons could result in additional tracks, e.g., the positron annihilates with an electron in the detector and produces two more γs, which in turn may further convert to an electron and positron. From figure 6.6 one sees that the low multiplicity events are suppressed by the addition of the conversion-produced tracks, however, they both approximately follow the same distribution for the events with a multiplicity above 20 per event.

6.4.2 Results of analysis

The yields of the *detectable γ conversions* produced by Geant were determined utilizing the Monte Carlo information and is shown in figure 6.7 for η, ϕ, and p_t. The values of η, ϕ, and p_t of the reconstructed HLT tracks in the events are also shown in figure 6.7. All plots in figure 6.7 have been normalized by the total number of events processed in the data sample. Further adjustments were made to the cuts in the *V0-Finder* in order to optimize the efficiency of the γ detection and purity of the accepted V0s for the γ embedded p-p events. An additional cut was introduced, namely a cut on the opening angle of the two daughter tracks of the V0. A selection of the various cut sets are given in table 6.3 and the average efficiency and purity, determined in a p_t range of [0, 20] GeV/c, are listed in table 6.4. The results of introducing a p_t cut on the reconstructed γ was also examined and will be presented later in this section.

Cut set Nr.5 corresponds to the original default set of cuts present in the *V0-Finder* when this work began. The efficiency of the *V0-Finder* in locating the *detectable γ conversions*, and the purity of the accepted sample are shown in figure 6.8. The average values determined in a p_t range of [0,

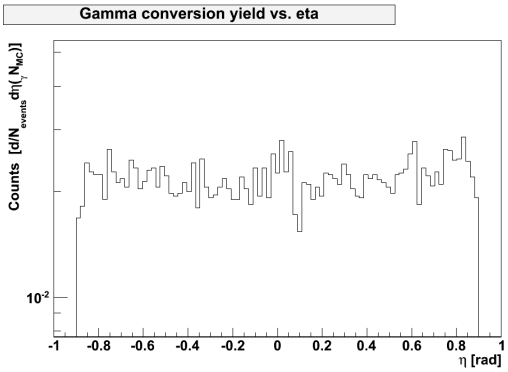

(a) Geant: γ conversion yields vs. η

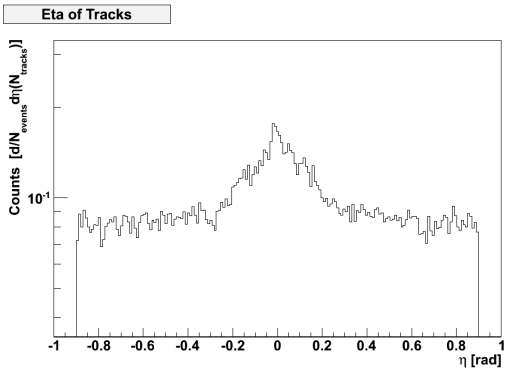

(b) HLT: Track multiplicity vs. η

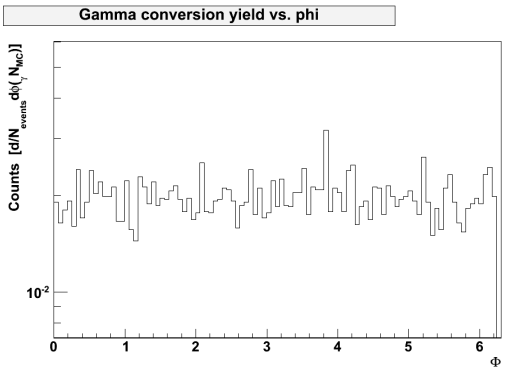

(c) Geant: γ conversion yields vs. ϕ

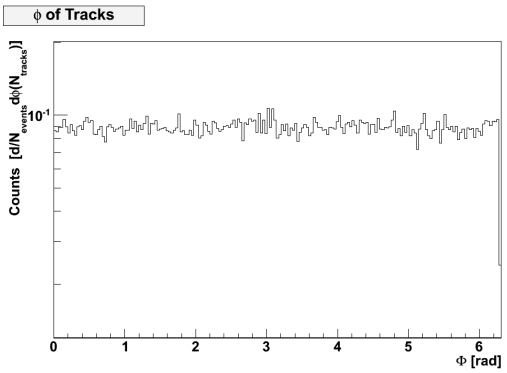

(d) HLT: Track multiplicity vs. ϕ

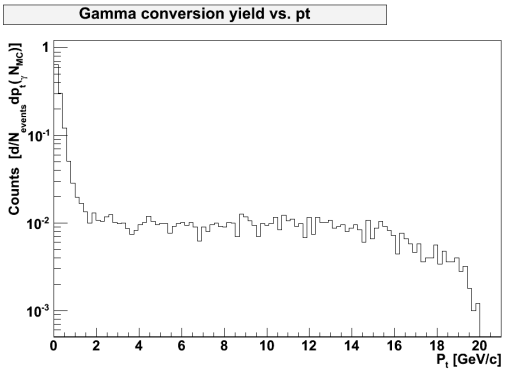

(e) Geant: γ conversion yields vs. p_t

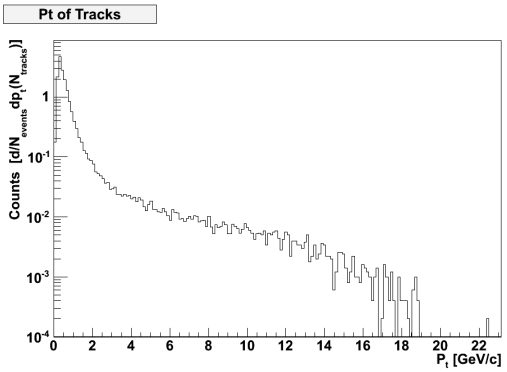

(f) HLT: Track multiplicity vs. p_t

Figure 6.7: Plots show the normalized **Geant** produced γ conversion yields and **HLT** track distributions from five-thousand γ embedded min. bias p-p events at $\sqrt{s} = 14\ TeV$ per nucleon-pair. Figures [a, c, e] show the respective conversion yields plotted against [η, ϕ, p_t], and figures [b, d, f] show the track distributions plotted against [η, ϕ, p_t] respectively.

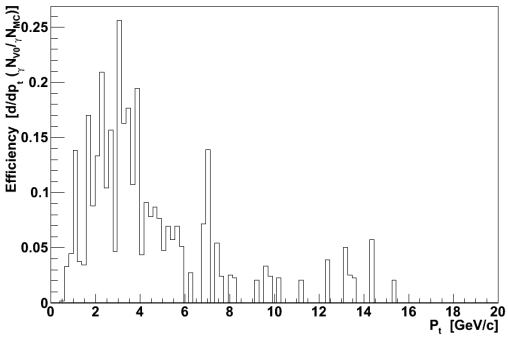

(a) Efficiency vs. p_t

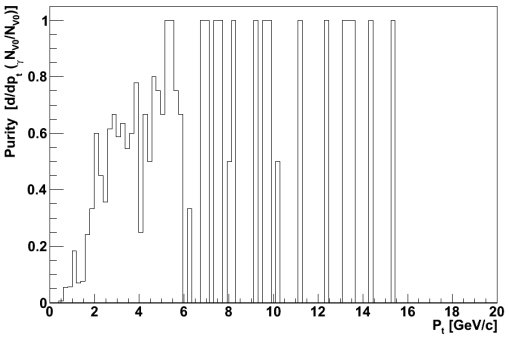

(b) Purity vs. p_t

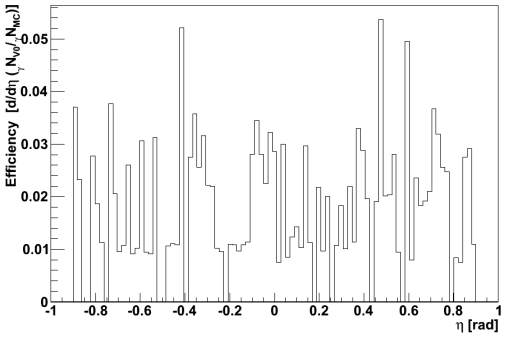

(c) Efficiency vs. η

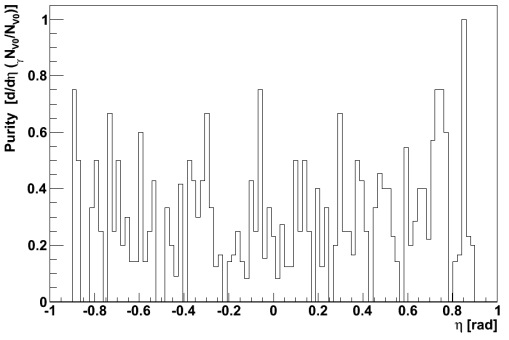

(d) Purity vs. η

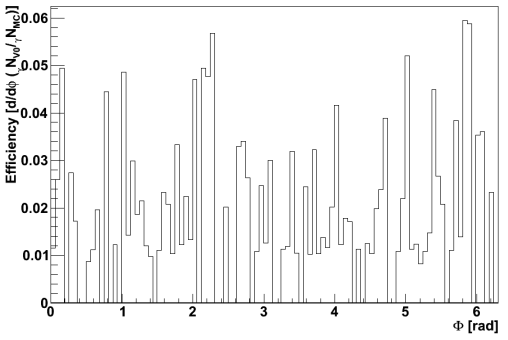

(e) Efficiency vs. ϕ

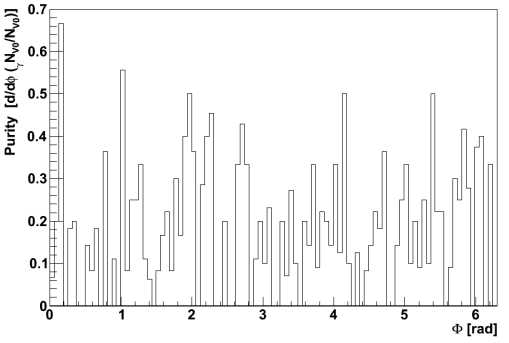

(f) Purity vs. ϕ

Figure 6.8: Figures show the efficiency and purity of the *V0-Finder* with cut set Nr.5, with **HLT** tracks as input, for five-thousand γ embedded min. bias. p-p events at $\sqrt{s} = 14\ TeV$ per nucleon pair. Figures show: (a) Efficiency plotted against p_t of the γ, (b) Purity plotted against p_t of the γ, (c) Efficiency plotted against η of the γ, (d) Purity plotted against η of the γ, (e) Efficiency plotted against ϕ of the γ, (f) Purity plotted against ϕ of the γ.

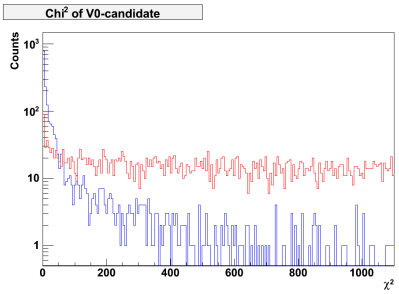

(a) χ^2 distribution

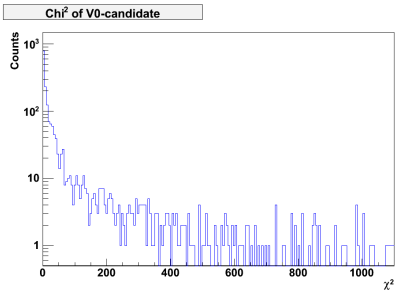

(b) χ^2 distribution

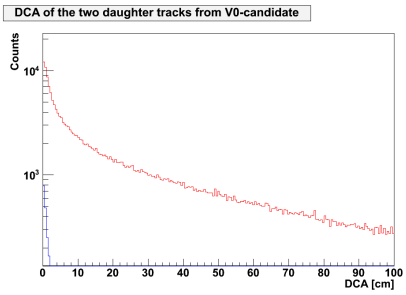

(c) DCA distribution

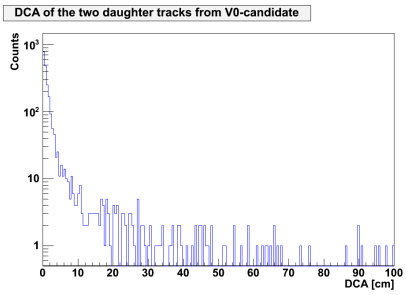

(d) DCA distribution

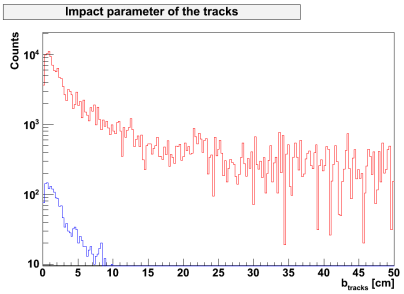

(e) Impact parameter of tracks

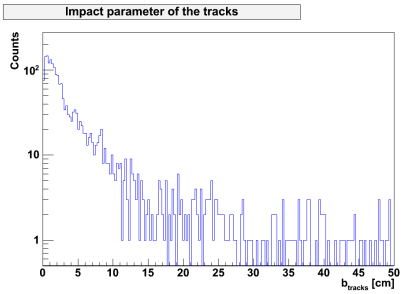

(f) Impact parameter of tracks

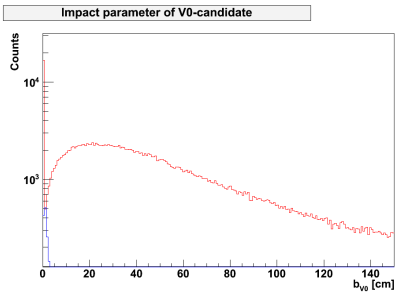

(g) Impact parameter of V0s

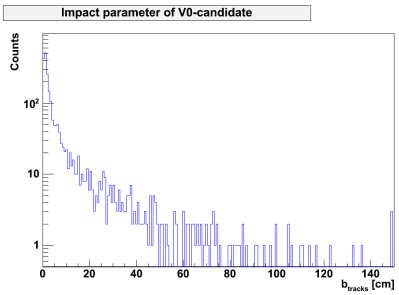

(h) Impact parameter of V0s

Figure 6.9: Figures show the cut distributions of every V0-candidate obtainable from the **HLT** tracks, for the five-thousand γ embedded p-p minimum bias events at $\sqrt{s} = 14\ TeV$ per nucleon pair. The blue histograms represent the real conversions, whereas the red histograms represent the fake conversions. Figures (a, b) show the χ^2 distribution, (c, d) show the DCA between the two tracks, (e, f) show the impact parameter of the tracks with respect to the primary vertex, and (g, h) show the impact parameter of the V0 candidate with respect to the primary vertex.

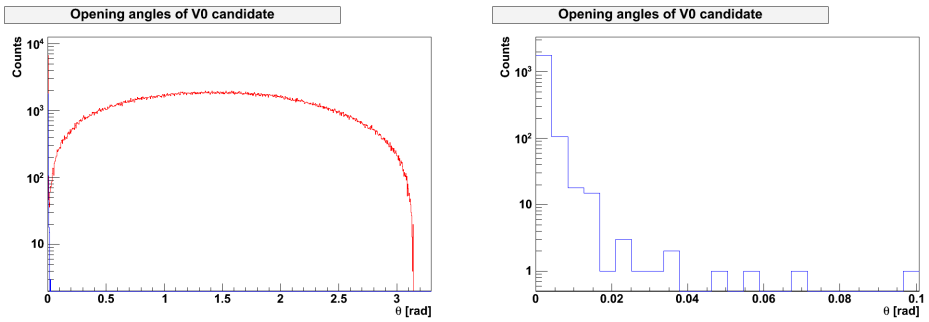

(a) (b)

Figure 6.10: Figures showing the opening angles of the daughter tracks from the HLT V0-candidate. The blue histograms correspond to the opening angles from the real *detectable* γ *conversions*, and the red histogram represents the fake conversion candidates. Figure (a) shows the opening angles of both real and fake conversions, whereas figure (b) only shows a close up of the opening angles from the real conversions. The figures were produced using the Monte Carlo labels of the V0's daughter tracks.

20] GeV/c are given in table 6.4. Analogous to the one-thousand pure events previously described, the efficiency and purity distributions were found to be approximately independent on η and ϕ, and will therefore only be shown for cut set Nr.5.

The distribution in the opening angles of the V0s are shown in figure 6.10, where the blue histogram represents the V0s that correspond to real *detectable* γ *conversions* and the red histogram represents the V0s that are not. The more energetic a photon is, the more probable it is that the produced electron and positron will be created in a direction close to that of the original direction of the γ. This effect may be seen from figure 6.10, where the real conversions have small opening angles. Therefore, a large portion of the fake conversions may be removed by the appropriate implementation of a cut on the opening angle of the conversion candidates. After examination of the distribution, the value of the cut was conservatively set to 0.05 radians, to avoid any substantial loss of real conversions. The addition of this cut, along with optimal values from the pure γ and $\pi^{\pm}$ events, correspond to cut set Nr.6 and the results are shown in figure 6.11 (a) and (b), and table 6.4. The value of the angle was ultimately lowered to improve the purity, but was maintained sufficiently large as not to remove too many of the real conversions. The improvement may be seen as cut set Nr.7 in table 6.3 and its efficiency and purity are displayed in figure 6.11 (c) and (d), and table 6.4.

As was done with the pure γ and $\pi^{\pm}$ events outlined in the previous section, the cuts were removed from the *V0-Finder*. The *V0-Finder* could

Selected *V0-Finder* cut sets: Min. bias. p-p embedded γs events					
Cut set	Imp. Par.: Tracks	DCA	Imp. Par.: V0s	$L_{Decay}/\sigma_{L_{Decay}}$	$\Theta_{Opening}$
Nr.5	2.5	3.5	3.5	3.0	—
Nr.6	0.01	5.0	15.0	0.0	0.050
Nr.7	0.01	5.0	15.0	0.0	0.035
Nr.8	—	—	—	—	0.035
Nr.9	0.08	12.5	24.5	0.0	0.035

Table 6.3: A selection of the cut sets used in the analysis of the γ conversion detection capabilities, of HLT's *V0-Finder* for the γ embedded minimum bias p-p events at $\sqrt{s} = 14\ TeV$ per nucleon pair.

then process every possible combination of the negative and positive tracks, allowing for the determination of the cut distributions. These are shown in figure 6.9, where again the blue histograms represent the real *detectable* γ *conversions* and the red histogram correspond to the track combinations that don't originate from the same γ conversion. The maximum efficiency of the *V0-Finder* was determined after the removal of the cuts, corresponding to cut set Nr.8 in table 6.3 and table 6.4, where the corresponding efficiency and purity are shown in figure 6.11 (e) and (f).

The distribution of the decay length cut was produced to ensure that its validity, in the detection of γ conversions, was unaltered from that observed in the pure γ and $\pi^{\pm}$ events. Its value was thereafter kept at zero for the subsequent sets of cuts examined in the analysis of the *V0-Finder*.

Further, numerous adjustments on the cuts were made on the basis of the plotted distributions shown in figure 6.9. However, analogous to the pure γ and $\pi^{\pm}$ events, only the results of the final optimized set will be further included in this thesis. As can be seen from the cut distributions in figure 6.9 (d) a DCA cut-off of 5.0 *cm* removed too many of the real conversions and was necessarily increased. In the same fashion, the value of the impact parameter of the V0 candidate cut was also raised to accept more real conversions. The impact parameter on the tracks with respect to the primary vertex was slightly increased to improve the purity of the sample, without removing a significant portion of the real *detectable* γ *conversions*. The optimal cut set is labeled as Nr.9 in table 6.3 and its corresponding efficiency and purity are shown in figure 6.11. The average efficiency and purity related to cut set Nr.9, determined against the transverse momentum of the detected γ, are listed in table 6.4.

After optimization of the cuts in the *V0-Finder*, the effect of a cut on the transverse momentum of the reconstructed γ was examined. The results of the p_t cut are shown in table 6.5. Though currently not implemented in the *V0-Finder* as a default cut, the results of the p_t cut have been included in this paper as a reference for future applications.

V0-Finder efficiency and purity for selected cut sets:		
Min. bias. p-p embedded γs events		
Cut set	Average efficiency	Average purity
Nr.5	0.04 %	30.0 %
Nr.6	37.0 %	76.6 %
Nr.7	37.0 %	78.4 %
Nr.8	46.3 %	56.6 %
Nr.9	42.0 %	72.5 %

Table 6.4: Table showing the average efficiency and purity values for the different sets of cuts for the HLT *V0-finder*, from the γ embedded minimum bias p-p events at $\sqrt{s} = 14\ TeV$ per nucleon pair, with HLT tracks as input.

Effects of introducing a p_t on the photon for cut set Nr.9		
5 000 simulated p-p events embedded with 10 γs per event.		
p_{tcut} $[GeV/c]$	Average efficiency	Average purity
—	(42.00 ± 0.71) %	(72.54 ± 1.62) %
0.2	(42.43 ± 0.71) %	(73.27 ± 1.62) %
0.4	(42.86 ± 0.71) %	(74.02 ± 1.62) %
0.6	(43.25 ± 1.12) %	(74.63 ± 1.95) %
0.8	(43.53 ± 1.22) %	(75.12 ± 2.13) %
1.0	(43.80 ± 1.28) %	(75.68 ± 2.34) %
2.0	(44.30 ± 1.37) %	(77.34 ± 2.64) %
3.0	(44.07 ± 1.41) %	(77.96 ± 2.79) %
4.0	(43.27 ± 1.44) %	(78.12 ± 2.91) %
5.0	(43.02 ± 1.50) %	(78.02 ± 3.04) %

Table 6.5: Table showing the values for the average efficiency and purity plotted against p_t of the γ, for different p_t cuts in HLT's *V0-Finder*, from five-thousand γ embedded p-p events at $\sqrt{s} = 14\ TeV$ per nucleon pair, with HLT tracks as input.

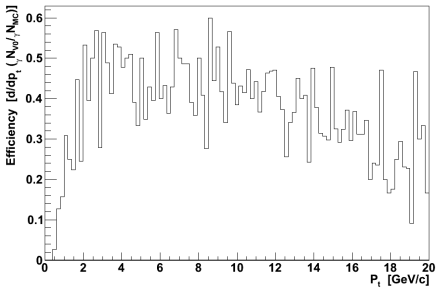

(a) Efficiency vs. p_t

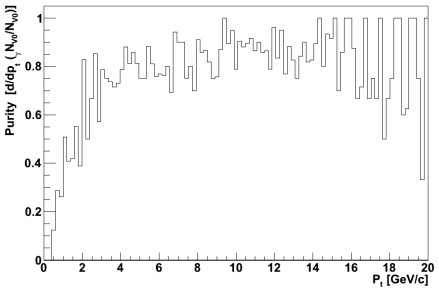

(b) Purity vs. p_t

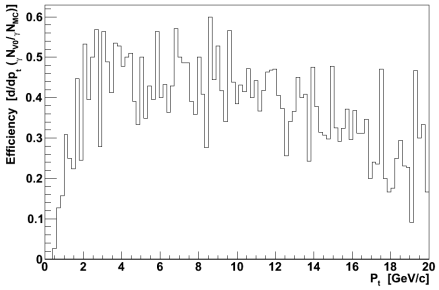

(c) Efficiency vs. p_t

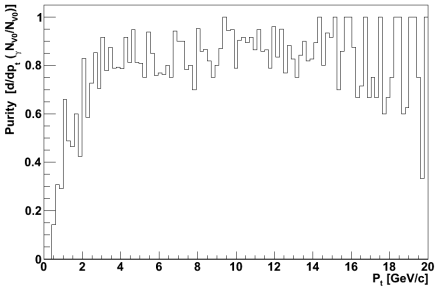

(d) Purity vs. p_t

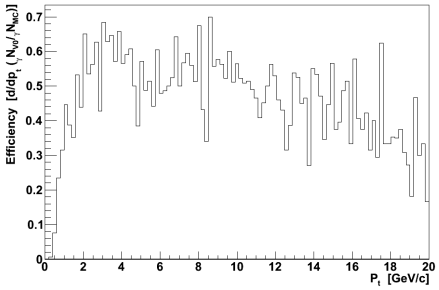

(e) Efficiency vs. p_t

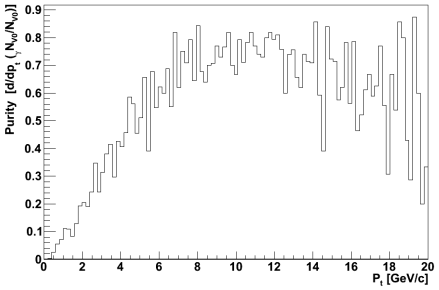

(f) Purity vs. p_t

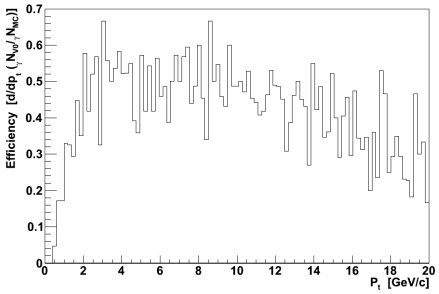

(g) Efficiency vs. p_t

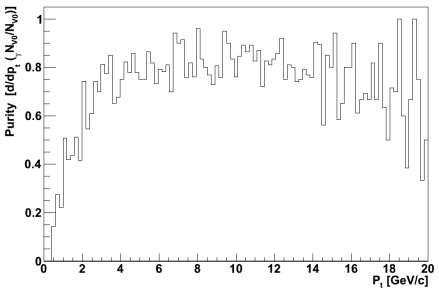

(h) Purity vs. p_t

Figure 6.11: Figures show the efficiency and purity of the *V0-Finder* with **HLT** tracks as input, for five-thousand γ embedded min. bias. p-p events at $\sqrt{s} = 14\ TeV$ per nucleon pair. Figures show: (a) Cut Set Nr.6: Efficiency against p_t of the γ, (b) Cut Set Nr.6: Purity against p_t of the γ, (c) Cut Set Nr.7: Efficiency against p_t of the γ, (d) Cut Set Nr.7: Purity against p_t of the γ, (e) Cut Set Nr.8: Efficiency against p_t of the γ, (f) Cut Set Nr.8: Purity against p_t of the γ, (g) Cut Set Nr.9: Efficiency against p_t of the γ, (h) Cut Set Nr.9: Purity against p_t of the γ.

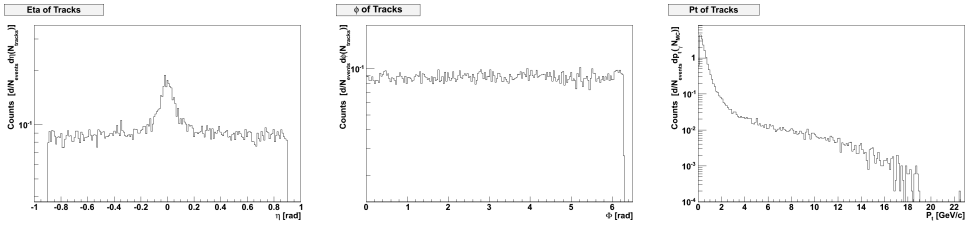

(a) Track multiplicity vs. η (b) Track multiplicity vs. ϕ (c) Track multiplicity vs. p_t

Figure 6.12: Plots show the **off-line** track distributions from five-thousand γ embedded minimum bias p-p events at $\sqrt{s} = 14\ TeV$ per nucleon-pair. Figures [a, b, c] show the track distributions plotted against η, ϕ, and p_t respectively.

V0-Finder efficiency and purity for selected cut sets:		
Min. bias. p-p embedded γs events: **Off-line** *tracks*		
Cut set	Average efficiency	Average purity
Nr.9	61.80 %	83.78 %

Table 6.6: Table showing the average efficiency and purity values of cut set Nr.9 for the HLT *V0-finder* using the **off-line** tracks as input, from the five-thousand γ embedded minimum bias p-p events at $\sqrt{s} = 14\ TeV$ per nucleon pair.

V0-Finder processing events with *off-line* tracks

The five-thousand γ embedded events were also reconstructed by the *V0-Finder* while using the *off-line* tracks as input. The cut set used for processing the *off-line* tracks was cut set Nr.9, which resulted in an average efficiency of 61.80 % and a purity of 83.78 %, in the p_t range of [0, 20] GeV/c, as listed in table 6.6. The efficiency and purity was plotted against p_t, and are shown in figure 6.14. The multiplicities of the off-line tracks plotted against η, ϕ, and p_t are shown in figure 6.12. The cut distributions for the *off-line* tracks were produced in a similar fashion as that of the HLT-tracks described above, and are shown in figure 6.13.

The efficiency of the *V0-Finder* in locating *detectable γ conversions* and the respective purity of the produced sample of V0s, are higher when using the *off-line* tracks as input, compared to using the *HLT* tracks. A significant contribution to the difference is due to the different tracking methods. One contribution from the tracking may be that the HLT reconstruction doesn't use the SDD detectors in the reconstruction, whereas the *off-line* reconstruction does. In addition, the *off-line* reconstruction has more time at its disposal to improve the track-fitting, which is also reflected in the χ^2 distribution of the *off-line* tracks in figure 6.13 (a) and 6.13 (b), compared

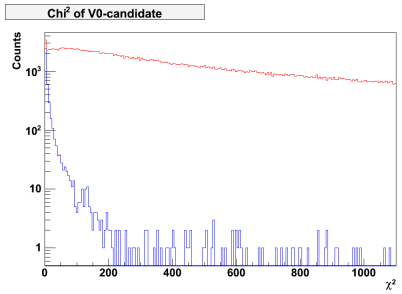

(a) χ^2 distribution

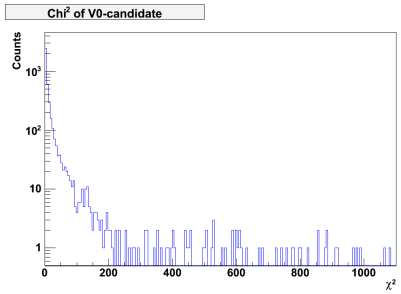

(b) χ^2 distribution

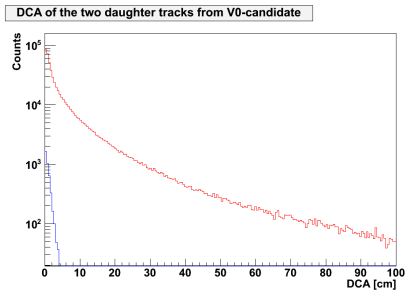

(c) DCA distribution

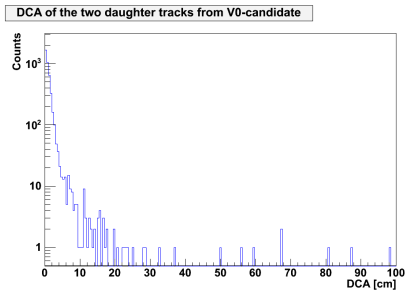

(d) DCA distribution

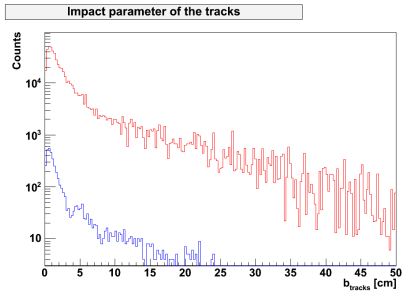

(e) Impact parameter of tracks

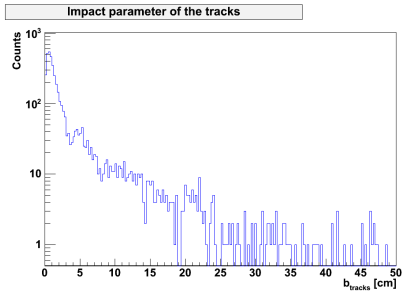

(f) Impact parameter of tracks

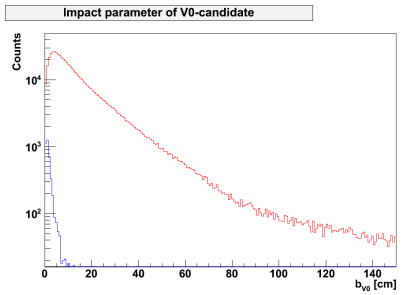

(g) Impact parameter of V0s

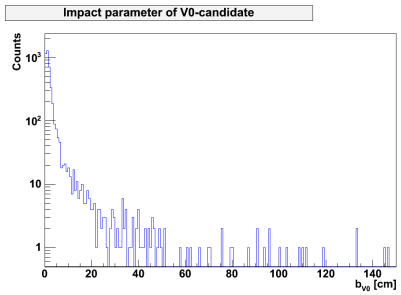

(h) Impact parameter of V0s

Figure 6.13: Figures show the cut distributions of every V0-candidate obtainable in the **HLT** *V0-Finder* with **off-line** tracks as input, for five-thousand γ embedded p-p minimum bias collisions at $\sqrt{s} = 14\ TeV$. The blue histograms represent the real conversions, whereas the red histograms represent the fake conversions. Figures (a, b) show the χ^2 distribution, (c, d) show the DCA between the two tracks, (e, f) show the impact parameter of the tracks with respect to the primary vertex, and (g, h) show the impact parameter of the V0 candidate with respect to the primary vertex.

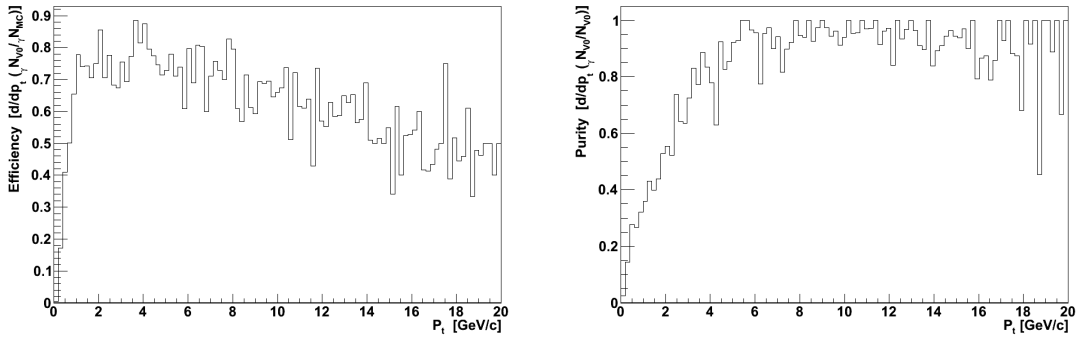

(a) Efficiency vs. p_t (b) Purity vs. p_t

Figure 6.14: Figures show the efficiency and purity of the *V0-Finder* with cut set Nr.9 with **off-line** tracks as input, for five-thousand γ embedded min. bias. p-p events at $\sqrt{s} = 14\ TeV$ per nucleon pair. Figures show: (a) Efficiency plotted against p_t of the γ, (b) Purity plotted against p_t of the γ.

to the HLT χ^2 values shown in figure 6.9 (a) and (b). The improved tracking may also lead to an improved determination of the primary vertex position, where the improvement may be propagated to the efficiency, and purity, through the impact parameter cuts in the *V0-Finder*.

Also, as can be seen from the *off-line* distributions, cut set Nr.9 is most likely not the optimal set of cuts for the *off-line* tracks, and the optimal values for the efficiency and purity may most likely be improved.

6.5 Large scale simulation of p-p events embedded with γs

In order to obtain a value for the *V0-Finder's* efficiency in locating *detectable* γ *conversions*, and the purity of the produced conversion candidates, a large scale simulation was carried out to provide sufficient statistics. A simulation of *one-hundred-thousand* γ embedded minimum bias p-p collision events were produced with identical event parameters as that described in section 6.4.1. The final results obtained for HLT's *V0-Finder* with its optimal cut set with HLT tracks as input, will be presented in the current section, along with a comparison of the optimized results from *off-line's* own *V0-Finder* processing real events, as presented in [52, 53, 54].

6.5.1 Results

An additional radial cut was added to the *V0-Finder* in an attempt to improve the purity. The cut removed the V0-candidates that had a recon-

structed secondary vertex within 1 *cm* of the primary vertex. This cut was added on the basis that it could potentially remove a portion of the contamination in the sample due to Dalitz decays occurring near the IP. A Dalitz decay represents a π^0 directly decaying to two leptons and a γ, e.g., $\pi^0 \rightarrow e^- e^+ \gamma$. The value of the cut was set based on the radial distribution of the γ conversions, and was chosen to remove a minimal portion of the real conversions. A higher value for the cut would improve the purity further, however, it will also diminish the efficiency. For the remainder of this thesis, cut set Nr.9 will entail the cut set as described in section 6.4.2 with the addition of the radial cut mentioned above.

The γ conversion yield produced by Geant was plotted against η, ϕ, and p_t is shown in figure (6.15). Also shown in figure (6.15), is the η, ϕ, and p_t distributions of the HLT reconstructed tracks from all of the events, where again all plots have been normalized by the total number of events in the reconstructed data sample. The *V0-Finder's* efficiency in locating a γ conversion, and the purity of the accepted conversion candidates, are shown in figure (6.17) for p_t, η, and ϕ. The average values for the efficiency and purity, in a p_t range of [0, 20] GeV/c, are given in table 6.7.

The track and conversion distributions are important to keep in mind when observing the efficiency and purity distributions of the *V0-Finder*. This is especially visible in the drop around $|\eta| < 0.3$ in the purity versus η distribution shown in figure 6.17 (d). The drop in purity is most likely the result of the additional tracks in the mid-pseudo-rapidity range, relative to that in the range $|\eta| > 0.3$. The conversion yield, however, illustrates a relatively minor increase around $\eta \sim 0$ and $|\eta| \sim 0.9$. Additional conversions may, potentially, lead to a lower purity as for every N number of γ conversions, there are N^2 possible negative and positive track combinations that are processed by the *V0-Finder*, potentially more if track-splitting occurs.

From the conversion yield in figure 6.15 (a) we see an approximate 10 % increase in the yield around $\eta \approx 0$, compared to the minimum at $|\eta| \approx 0.2$. This increase will effectively lead to an 21 % increase in the number of possible negative and positive track combinations, as shown in equations (6.3) and (6.4), where ${}_{\gamma}N_{\eta}$ represents the number of *detectable* γ *conversions*

V0-Finder efficiency and purity for selected cut sets:		
100 000 Min. bias. p-p embedded γ*s events*		
Cut set	Average efficiency	Average purity
Nr.9	(41.71 ± 0.01) %	(74.02 ± 0.09) %

Table 6.7: Table showing the average efficiency and purity values of cut set Nr.9 for the HLT *V0-finder* with **HLT** tracks as input, from one-hundred-thousand γ embedded minimum bias p-p events at $\sqrt{s} = 14\,TeV$ per nucleon pair.

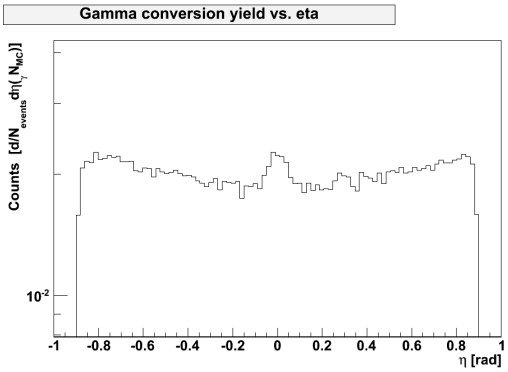

(a) Geant: γ conversion yields vs. η

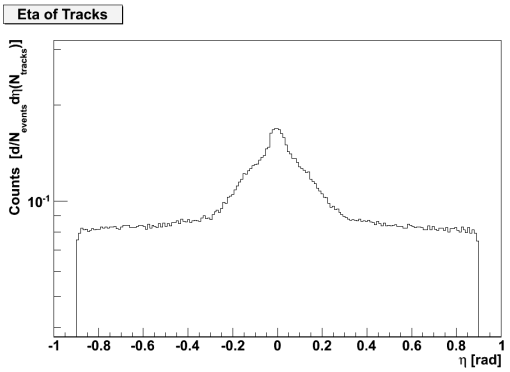

(b) HLT: Track multiplicity vs. η

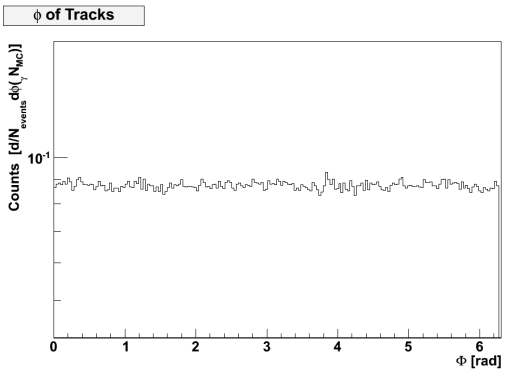

(c) Geant: γ conversion yields vs. ϕ

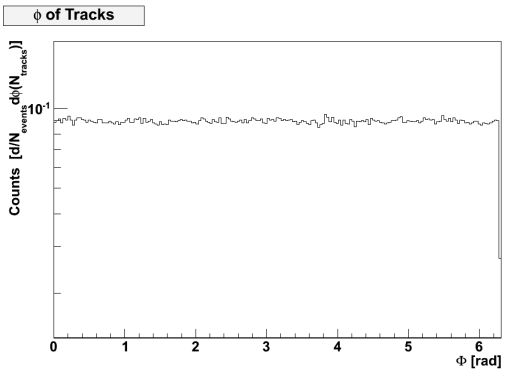

(d) HLT: Track multiplicity vs. ϕ

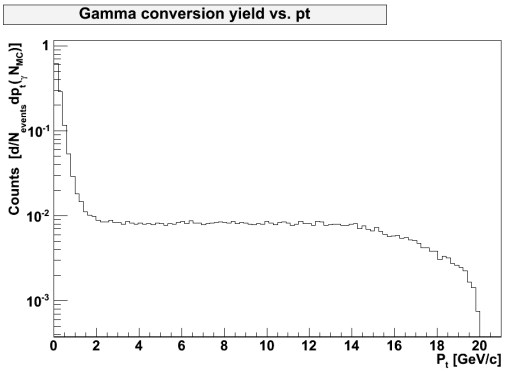

(e) Geant: γ conversion yields vs. p_t

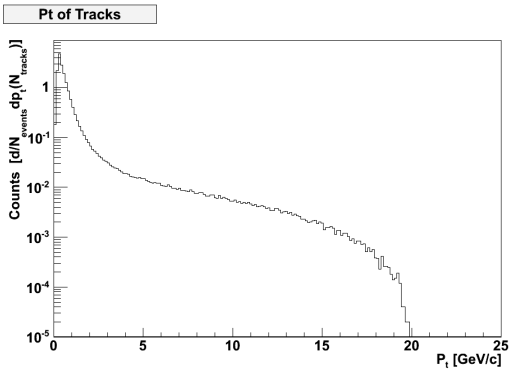

(f) HLT: Track multiplicity vs. p_t

Figure 6.15: Plots show the normalized **Geant** produced γ conversion yields and **HLT** track distributions from one-hundred-thousand γ embedded min. bias p-p events at $\sqrt{s} = 14\ TeV$ per nucleon-pair. Figures [a, c, e] show the respective conversion yields plotted against [η, ϕ, p_t], and figures [b, d, f] show the track distributions plotted against [η, ϕ, p_t] respectively.

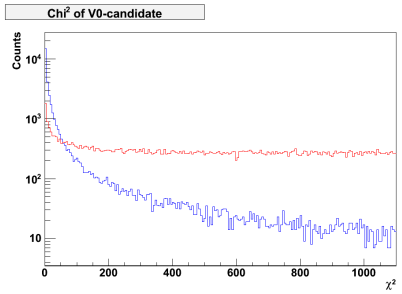

(a) χ^2 distribution

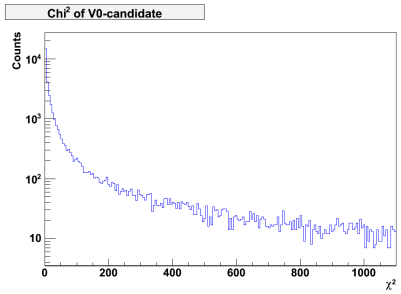

(b) χ^2 distribution

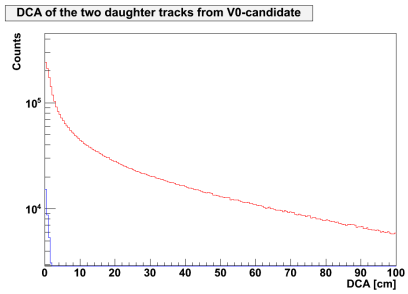

(c) DCA distribution

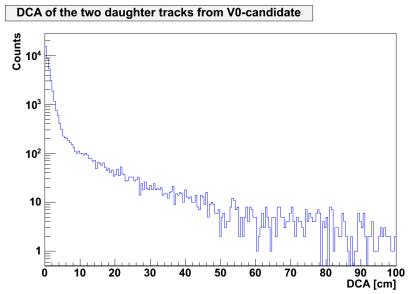

(d) DCA distribution

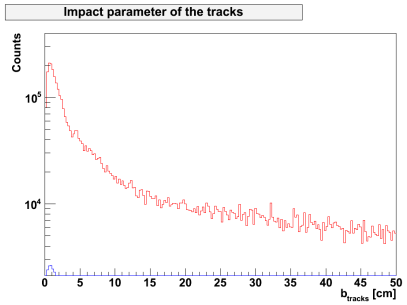

(e) Impact parameter of tracks

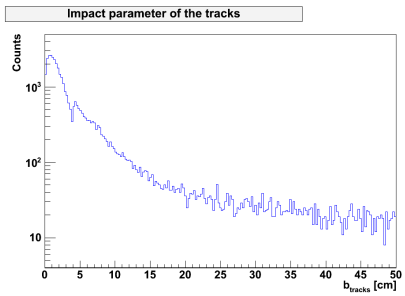

(f) Impact parameter of tracks

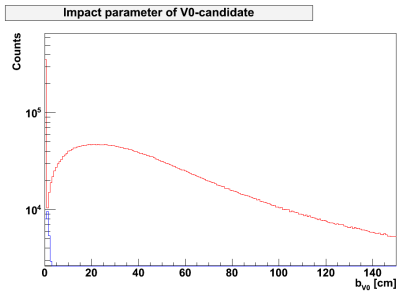

(g) Impact parameter of V0s

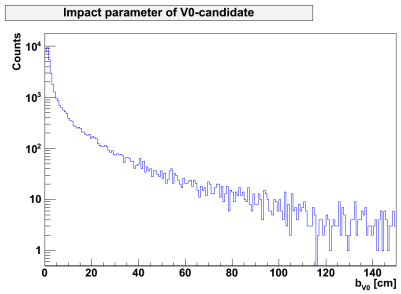

(h) Impact parameter of V0s

Figure 6.16: Figures show the cut distributions of every V0-candidate obtainable from the **HLT**, from the simulation of one-hundred-thousand γ embedded min. bias p-p collisions at $\sqrt{s} = 14\ TeV$ per nucleon pair. The blue histograms represent the real conversions, whereas the red histograms represent the fake conversions. Figures (a, b) show the χ^2 distribution, (c, d) show the DCA between the two tracks, (e, f) show the impact parameter of the tracks with respect to the primary vertex, (g, h) show the impact parameter of the V0 candidate with respect to the primary vertex.

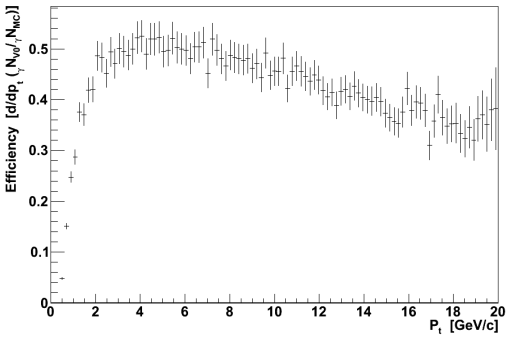

(a) Efficiency vs. p_t

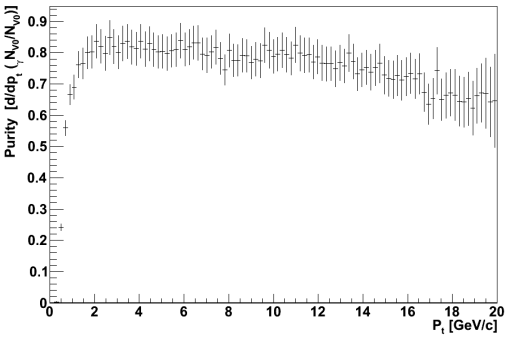

(b) Purity vs. p_t

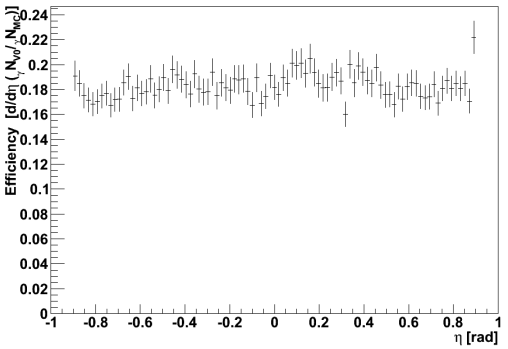

(c) Efficiency vs. η

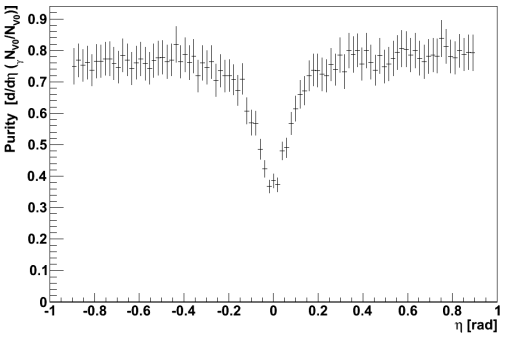

(d) Purity vs. η

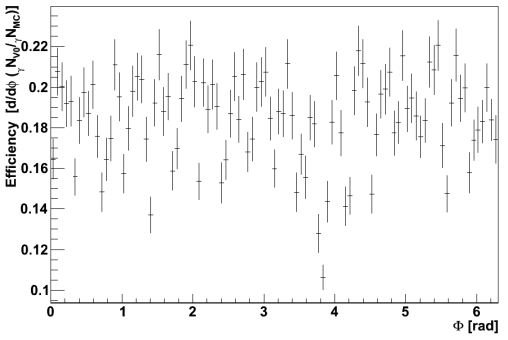

(e) Efficiency vs. ϕ

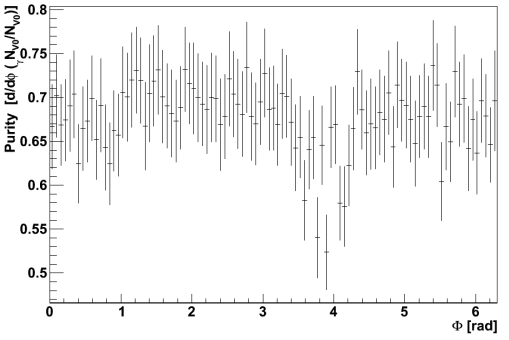

(f) Purity vs. ϕ

Figure 6.17: Figures show the efficiency and purity of the *V0-Finder* with cut set Nr.9 with **HLT** tracks as input, for one-hundred-thousand γ embedded min. bias. p-p events at $\sqrt{s} = 14\ TeV$ per nucleon pair. Figures show: (a) Efficiency plotted against p_t of the γ, (b) Purity plotted against p_t of the γ, (c) Efficiency plotted against η of the γ, (d) Purity plotted against η of the γ, (e) Efficiency plotted against ϕ of the γ, (f) Purity plotted against ϕ of the γ.

for the indicated η value, and ${}_cN_\eta$ represents the number of negative and positive track combinations from the tracks produced from the γ conversions for the indicated η value. If we consider the increase in the track multiplicity in figure 6.15 (b), we see that the multiplicities are approximately $N_{tracks} \approx 8 \times 10^{-4}$ at $|\eta| \approx 0.9$, and $N_{tracks} \approx 2 \times 10^{-3}$ at an $\eta \approx 0$. If we further crudely assume an equal number of positive and negative tracks, resulting in the possible number of track combinations to be $N_{combinations} = N_{tracks}/2$. This will correspond to an increase in possible track combinations processed by the *V0-Finder* of 225 %.

$$ {}_\gamma N_{0.0} \approx 1.10 \cdot_\gamma N_{0.9} \tag{6.3} $$

$$ {}_C N_{0.0} =_\gamma N_{0.0}^2 = (1.10 \cdot_\gamma N_{0.9})^2 \approx 1.21 \cdot_C N_{0.9} \tag{6.4} $$

Clearly, the observed increase in the charged particle multiplicity can not solely originate from the additional γ conversions around $\eta \approx 0$. If we divide the approximate purity at $|\eta| \approx 0.9$ by the increase in charged particle multiplicity, we obtain a similar value for the purity at $\eta \approx 0$, as what is shown in figure 6.17 (d), the calculation is shown in equation (6.5). Though this calculation doesn't necessarily prove that the reduced purity observed for $|\eta| < 0.3$ is entirely due to the increased track multiplicity, but it lends confidence to the assumption that it may be one of the main contributors to the observed purity reduction.

$$ P_{0.0} \approx \frac{P_{0.9}}{2.25} \approx \frac{0.76}{2.25} \approx 0.34 \tag{6.5} $$

The increase of the charged multiplicity around in the region $|\eta| < 0.3$ is unexpected, as the charged multiplicity distribution obtained from the real events are found to be approximately flat, if anything a slight decrease in the multiplicity is expected around $|\eta| \approx 0$. The source of the increase was traced back to the Monte Carlo simulation, specifically the minimum bias p-p generation, as can be seen from the Monte Carlo tracks produced during the particle transport of the simulation shown in figure 6.18, for η and ϕ. The plots in figure 6.18 were obtained from the simulation of minimum bias events without the γs embedded to ensure that our embedding wasn't the cause of the multiplicity increase. However, as of this writing the direct cause of the feature is not understood, though it is certain that it is a feature of the generation of the minimum bias p-p events.

In addition, we also see a feature in the purity versus ϕ distribution in the range of $3.5 < \triangle\phi < 4$. This is currently not understood, though it could be caused by the spike in the Geant produced multiplicity at $\phi \approx 3.2$. It may appear that there is dip in the efficiency around $\phi \approx 3.2$ as well. The underlying cause is currently not understood, and requires further investigation.

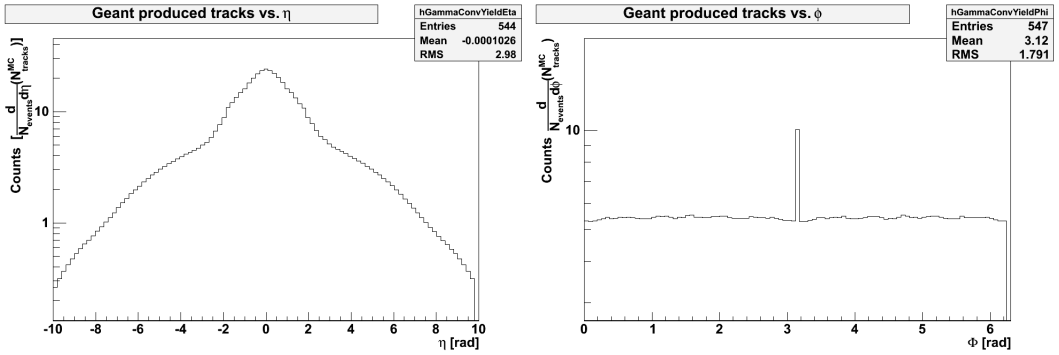

(a) Geant: $\frac{1}{N_{events}} \frac{dN}{d\eta}$ (b) Geant: $\frac{1}{N_{events}} \frac{dN}{d\eta}$

Figure 6.18: **Geant** produced track multiplicity for η and ϕ, normalized by the number of simulated events, from the simulation of minimum bias p-p collisions at $\sqrt{s} = 14\ TeV$ per nucleon pair. The cause of the increase in figure (a) around $|\eta| < 0.3$, and the spike at $\phi \approx 3.2$ in figure (b) is currently not understood and requires further investigation

The spatial distribution of the *detected* γ *conversions* found by the *V0-Finder* with cut set Nr.9 are shown in figure 6.19. In figure 6.19 (a) the ITS layers and TPC components are clearly visible, such as the TPC inner-field-cage vessel. The ITS layers are also visible in the radial distribution of the conversions, when compared to table 4.1 in section 4.2.2. From the figure, one can see that most of the γ conversions took place in the ITS. This is due to the fact that the cross section of the pair-production process scales linearly with the inverse of the density of the traversed material. Solid-state materials have a substantially higher density than gaseous compounds, which is why most of the conversions happen in the ITS and only a relatively small number of conversions are observed in the drift region of the TPC.

The effects of implementing a cut on the p_t of the γ was reexamined, to provide high statistics and lower stochastic uncertainties in the obtained average efficiency and purity values, compared to that observed from the five-thousand event data sample. The obtained results are listed in table 6.8. However, additional effects must be considered before implementing such a cut, such as the size and bandwidth of the data-storage allocated for the γ conversion application. Also the end goal of the γ conversion must be attributed to an adequate p_t range of the measured quantity, for instance π^0 reconstruction through the two photon decay process, $\pi \rightarrow \gamma\gamma$, is most frequently observed in a p_t-range of a few hundred MeV/c to a few GeV/c.

The addition of γs to the events lead to an overall increase in the charged track multiplicity. The efficiency and purity calculations may therefore not reflect the true efficiency and purity that it would have for non-embedded or real events. As has been described above, an increase in tracks may result in

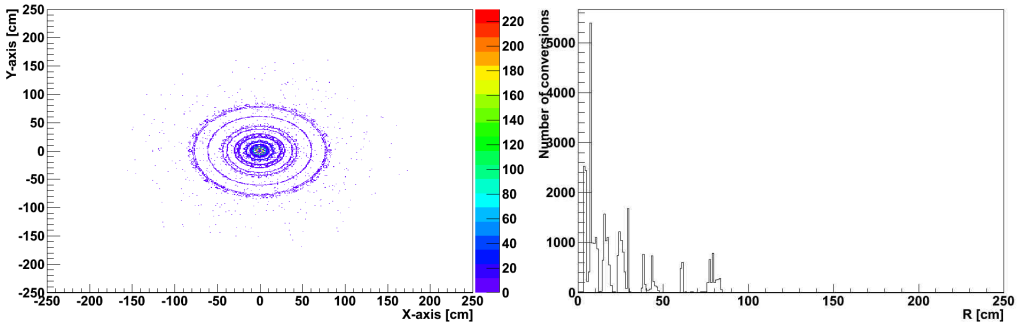

(a) *Detected γ conversions in the X-Y plane* (b) Radial distance of detected γ conversion

Figure 6.19: Figure showing the *detectable γ conversions* found by the *V0-Finder* with cut set Nr.9 with **HLT** tracks as input, from the γ embedded p-p events at $sqrts = 14\ TeV$ per nucleon pair. Figure (a) shows the γ conversions found, plotted for their $x-$ and $y-coordinates$. Figure (b) shows the radial distance of the conversion from the IP.

Effects of introducing a p_t on the γ for cut set Nr.9:		
100 000 simulated p-p events embedded with 10 γs per event.		
$p_{t_{cut}}$ $[GeV/c]$	Average efficiency	Average purity
—	(41.71 ± 0.01) %	(74.02 ± 0.09) %
0.2	(42.13 ± 0.01) %	(74.77 ± 0.09) %
0.4	(42.56 ± 0.16) %	(75.53 ± 0.50) %
0.6	(42.95 ± 0.25) %	(76.06 ± 0.56) %
0.8	(43.24 ± 0.28) %	(76.27 ± 0.58) %
1.0	(43.44 ± 0.30) %	(76.37 ± 0.58) %
2.0	(43.76 ± 0.31) %	(76.36 ± 0.61) %
3.0	(43.53 ± 0.33) %	(76.00 ± 0.63) %
4.0	(43.12 ± 0.34) %	(75.63 ± 0.65) %
5.0	(42.56 ± 0.35) %	(75.22 ± 0.67) %

Table 6.8: The table shows the values for the average efficiency and purity found for p_t of the γ, for the different p_t cuts in HLT's *V0-Finder* with **HLT** tracks as input, from one-hundred-thousand γ embedded p-p events at $\sqrt{s} = 14\ TeV$ per nucleon pair.

a reduction of the purity. Further, the efficiency may also be altered through addition of γ conversions, as the ratio of conversions to tracks will be larger than in non-embedded or real events, however, the ratio of split-tracks to full length tracks will remain the same as this is a feature of the tracking algorithm. This effect may lead to a higher number of conversions not correctly reconstructed by the *V0-Finder* due to the splitting feature, which will in turn result in a lower efficiency. However, the shape of the efficiency and purity distributions plotted against η, ϕ, and p_t should maintain the approximate same shape, as the respective values of the embedded γs were evenly and randomly produced in these ranges, apart from the in the region of $|\eta| < 0.3$ due to the flaw Monte Carlo simulation.

6.5.2 Calculating the uncertainties

Due to the inherent uncertainties in nature and the act of performing a measurement, experimental results will always be inhabited by uncertainties. Depending on the different processes the experimenter examines or measures, the data will be governed by different statistical distributions.

The number of observed γ conversions may be described by a Poisson distribution. The expectation value, $E[X]$, of a Poisson distributed variable is defined in equation (6.6), where X represents the number of *detectable* γ *conversions* in the sample, μ is the probability of a γ converting to an electron-positron-pair, t represents the number of γs in the sample, and $\epsilon_{detectable}$ represents the ratio of the number of *detectable* γ *conversions* to the total number of γ conversions in the sample. The variance of the expectation value for the number of Poisson distributed γ conversions is also given in equation (6.6).

$$E[X] = \mu \cdot t \cdot \epsilon_{geo} = \lambda \quad , \quad \sigma_X = \sqrt{\lambda} \tag{6.6}$$

The expectation value of the number of *detectable* γ *conversions* found from processing the Monte Carlo information is shown in equation (6.7), where ϵ_{MC} represents the ratio of the number of *detectable* γ *conversions* to the total number of *detectable* γ *conversions*, and N_{MC} is the total number of *detectable* γ *conversions* found from processing the Monte Carlo information. Since all the information from the simulation is available in the Monte Carlo information, this necessarily means that ϵ_{MC} must equal one. The expectation value of the number of *detectable* γ *conversions* found by the *V0-Finder* is found in a similar fashion, where the efficiency factor is now for the *V0-Finder* represented by ϵ_{V0}, and shown in equation (6.8).

$$E[X_{MC}] = \mu \cdot t \cdot \epsilon_{geo} \cdot \epsilon_{MC} = \lambda = \lambda_{MC} = N_{MC} \tag{6.7}$$

$$E[X_{V0}] = \mu \cdot t \cdot \epsilon_{geo} \cdot \epsilon_{V0} = \epsilon_{V0} \cdot \lambda = \lambda_{V0} = N_{V0} \tag{6.8}$$

If equation (6.8) is solved for the efficiency of the *V0-Finder*, ϵ_{V0}, we see from the resulting equation (6.9) that the efficiency may be found by dividing the number of *detectable* γ *conversions* found by the *V0-Finder* and that found from the Monte Carlo information, which is precisely what we defined in equation (6.1). As the measurement of the number of conversions found by the respective methods are independent, the variance of the efficiency may be determined by the use of equation (6.10).

$$\epsilon_{V0} = \frac{E\left[X_{V0}\right]}{E\left[X_{MC}\right]} = \frac{\lambda_{V0}}{\lambda_{MC}} = \frac{N_{V0}}{N_{MC}} \tag{6.9}$$

$$\sigma_{\epsilon_{V0}} = \sqrt{\lambda_{MC}} + \sqrt{\lambda_{V0}} = \sqrt{N_{MC}} + \sqrt{N_{V0}} \tag{6.10}$$

Further, one can calculate the mean efficiency of the different samples, as was done for the average efficiency in a p_t range of [0, 20] GeV/c. The equation for the mean efficiency is given in equation (6.11) and the variance is shown in equation (6.12), where ϵ_i corresponds to mean efficiency of sample i, and σ_i corresponds to variance in the mean efficiency ϵ_i of sample i.

$$\bar{\epsilon_{V0}} = \frac{\sum_{i=1}^{i=n} \epsilon_i}{n} \tag{6.11}$$

$$\frac{1}{\bar{\sigma_{\epsilon_{V0}}}^2} = \sum_{i=1}^{i=n} \left(\frac{1}{\sigma_{\epsilon_i}^2} \right) \tag{6.12}$$

The uncertainties outlined above were obtained with knowledge of the statistical nature of a repeated observation, or measurement, of the number of γ conversions. However, these stochastic uncertainties may not be the only contributors to obtaining inaccurate values for the efficiency and purity of the *V0-Finder*. Other contributions to an inaccuracy may arise from systematic uncertainties, as the already mentioned flawed Monte Carlo simulation, and from the momentum and spatial resolutions of the reconstructed tracks.

6.5.3 Momentum resolutions of the reconstructed HLT data

In addition to determining the efficiency of the *V0-Finder's* ability in locating a γ conversion, and the purity of the respectively accepted sample of V0-candidates, the momentum resolutions were determined for the tracks and V0s produced in the HLT event reconstruction. The momentum resolutions were determined using equation 6.13.

$$P_{res} = \frac{|\Delta P|}{P} = \frac{|P_{reconstructed} - P_{MC}|}{P_{MC}} \tag{6.13}$$

Due to the fact that only the ITS and TPC detectors were initiated for the event reconstruction, an accurate PID wasn't available for the reconstructed tracks and their respective particle masses were by default assumed to be πs. This feature effectively represents a systematic uncertainty introduced in the determination of the resolutions. This systematic effect was corrected for by using the Monte Carlo label of the track to acquire its true particle type, after which the PID of the track was set to its Monte Carlo value. If comparing the presented results with measured results from real data, it is important to keep in mind that this corresponds to an PID efficiency of 100 %, which is unlikely unobtainable in real events with similar characteristics.

The momentum resolution of the reconstructed *detectable γ conversions* from the HLT *V0-Finder*, with cut set Nr.9, using HLT tracks as input, running over the *one-hundred-thousand* event data sample is shown in figure 6.20 (a). The momentum resolution of the negative tracks of all of the accepted V0-candidates is shown in 6.20 (b). The distributions follow the approximate expected trend, though additional work is required to provide a thorough analysis of the presented resolutions. They have been included in this thesis to indicate the current status of the HLT reconstructed momentum resolutions, though we note, that improvements are expected to occur and that the presented resolutions are in no way the final and optimal values.

Poor resolutions may be the result of systematic errors, such as erroneously assigning a PID to a track, and inefficiencies in the cluster finder algorithm. For instance, if some of the clusters that actually belong to a track are removed, this could cause a false determination of the track's momentum. Further, if track-splitting occurs in the reconstruction in a track, then this track may potentially not be eligible as a contributor to the primary vertex, whereas if it was reconstructed as the full-length track it may have been accepted as a contributor, due to its longer track-length and higher number of clusters. A higher number of contributors will result in more accurate determination of the primary vertex, where its benefits will propagate to the *V0-Finder*, as many of the cuts are directly related to the primary vertex.

6.5.4 Comparison with the Off-line V0-Finder

The off-line reconstruction has a separate and different V0-finder, used to locate γ conversions. The off-line V0-finder has been optimized for π^0 reconstruction, through the two-photon decay process, $\pi^0 \rightarrow \gamma\gamma$. Its efficiency in locating γ conversions, along with the purity of the produced sample of V0-candidates, are shown in figure 6.21 (a) and (b) respectively. The off-line results were obtained from processing large samples of real p-p collisions at $\sqrt{s} = 7\ TeV$ per nucleon pair, recorded by ALICE at the LHC, and

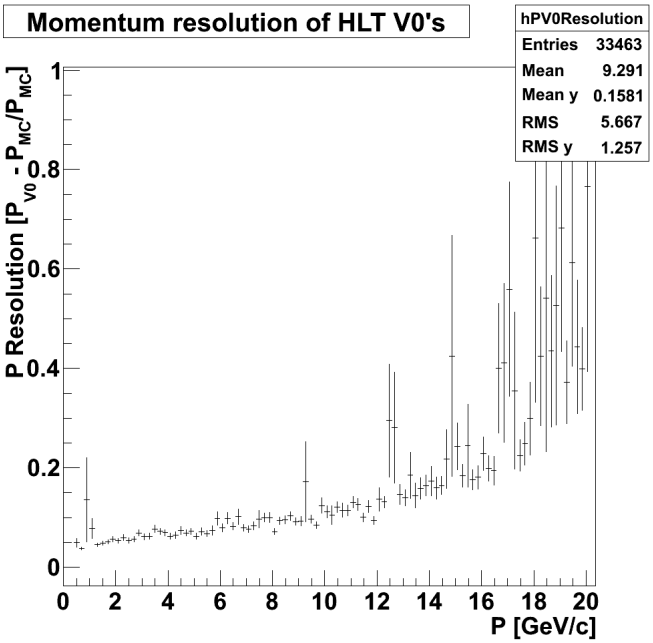

(a) P resolution of reconstructed γ

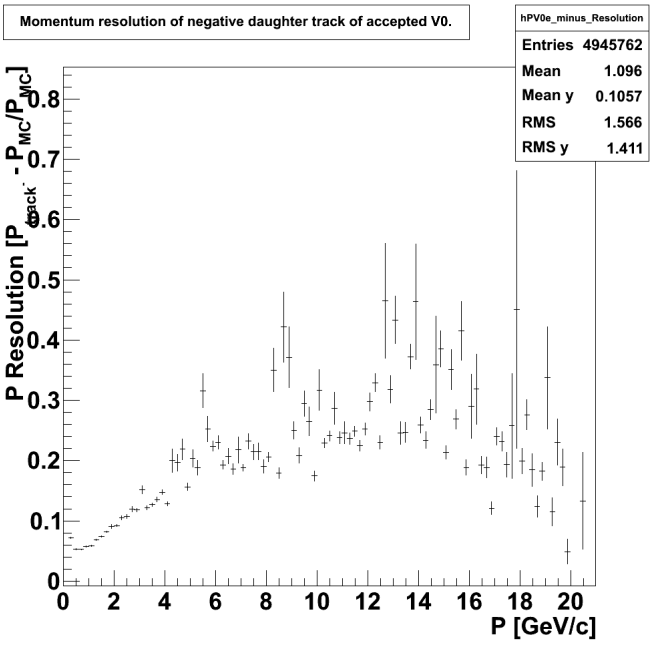

(b) P resolution of negative tracks from V0s

Figure 6.20: Figures show the momentum resolutions of the reconstructed γs from the **HLT** tracks, produced with **HLT's** *V0-Finder*, with cut set Nr.9, along with the negative tracks from all of the accepted V0-candidates, from one-hundred-thousand γ embedded min. bias p-p events at $\sqrt{s} = 14$ TeV per nucleon-pair. In figures: (a) P resolution of the reconstructed γ, with **HLT's** *V0-Finder* (b) P resolution of the **HLT** reconstructed negative track from all of the accepted V0-candiadtes.

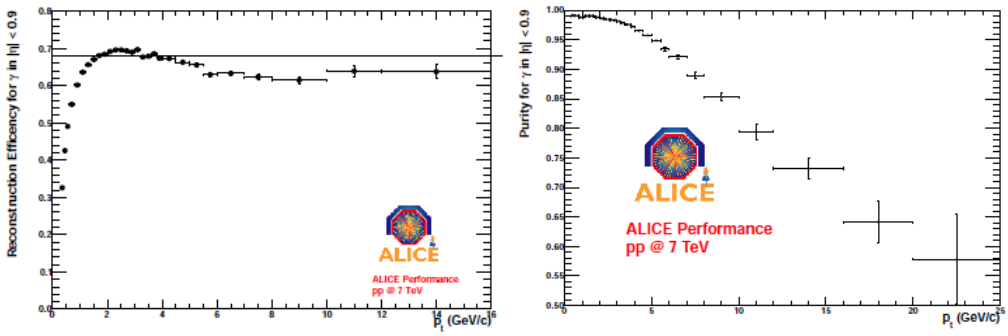

(a) (b)

Figure 6.21: Figure shows the efficiency and purity of **off-line's** V0-finder with **off-line** tracks as input, plotted against p_t. The results were obtain from processing real p-p collisions at $\sqrt{s} = 7\ TeV$ per nucleon pair, recorded by ALICE. The figure was taken from [52].

presented in [52, 53, 54].

The values of the efficiency and purity for the *off-line* V0-finder are substantially higher than that observed for the *on-line V0-Finder*. The reasons for the lower efficiency and purity in HLT's *on-line V0-Finder* may be many. As mentioned in the previous section, the act of embedding γs to the events may result in lower values for the efficiency and purity, as the γ conversions will directly increase the number of track combinations in the event. In addition, when comparing the results from the different V0-finders, it is important to note that the collision energies are different, $\sqrt{s} = 7\ TeV$ per nucleon pair for *off-line* and $\sqrt{s} = 14\ TeV$ per nucleon pair for *on-line*. The multiplicity has been found to approximately scale as the logarithm of the square root of the collisions energy, $ln\sqrt{s}$. Therefore, the events that were simulated for the analysis of HLT's *V0-Finder* are expected to have higher multiplicities, which in turn may result in lower values for the efficiency and purity. It is also important to keep in mind that the HLT data samples were simulated, contrary to the real events processed by the off-line V0-finder. Although all of these effects may contribute to the observed differences, the main contributor is most likely something else, directly related to the timing constraints of the on-line reconstruction, such as the tracking and number of cuts implemented in the *V0-Finder*.

The track finding efficiency for the off-line and on-line reconstruction was shown in [49] to be approximately the same for simulated p-p collisions at $\sqrt{s} = 14\ TeV$ per nucleon pair, see table 5.1. However, since off-line doesn't suffer from the same time constraint as on-line, it may reconstruct tracks with higher resolutions through a more timely and better track-fitting procedure. In addition, the off-line reconstruction takes advantage of the

SDD and TRD detectors for tracking, where the on-line reconstruction does not. The SDD has been deemed to slow to be incorporated in the on-line tracking, and the TRD is currently not fully commissioned for HLT. As mentioned in the previous section, the improvement of the tracks allow for a more accurate determination of the primary vertex. The improvement in the tracks and primary vertex will propagate through the respective *V0-Finder* algorithms, resulting in an improved values for the efficiency and purity.

Further, the off-line V0-finder has a number of additional cuts implemented to process the V0-candidates. Although, additional cuts may result in a higher purity and efficiency, it may still not be advantageous to add them to HLT's *V0-Finder*, as adding cuts to the algorithm could result in substantially longer processing times. However, the addition of some cuts, if sequenced properly, could in fact reduce the overall processing time. Sequencing, as it is referred to in this context, refers to the processing order and priority of the various cuts. For instance, the first cut in HLT's *V0-Finder* is a charge cut that removes all the positive tracks, thereby lowering the number of computations HLT's *V0-Finder* must perform, compared to if it had been rearranged to be the last cut. Therefore, intelligent sequencing of the cuts could reduce the processing time of the *V0-Finder*, and before adding a cut, one must consider its impact on the processing time, and not only on the observed efficiency and purity. A selection of the additional *off-line* cuts are listed below and described in [53].

- Low transverse momentum cut on both tracks
- Ratio of number of space-points to number of findable space-points
- Electron selection using the particles' energy loss
- Pion rejection using the particles' energy loss
- Geometrical cut in the space point location
- Photon selection using q_t from Armenteros-Podolanski plots

One of the additional *off-line* cuts that have posed particular interest during this analysis is the dE/dx cut. This cut proved to substantially improve the purity of the V0-sample produced by the *off-line V0-Finder*. If a dE/dx cut on the tracks were added to HLT's *V0-Finder*, this would allow for the selection of electrons and positrons, and the potential rejecting of other particle types, most notably the πs. This would then necessarily increase the purity as the combinatorial background will be reduced. Another contributor to the contamination arises from the presence of other neutral particle decays in the events. Even though the other neutral decays may be reconstructed correctly by HLT's *V0-Finder*, they will be labeled a false conversion and contribute to the contamination of the sample. A dE/dx cut

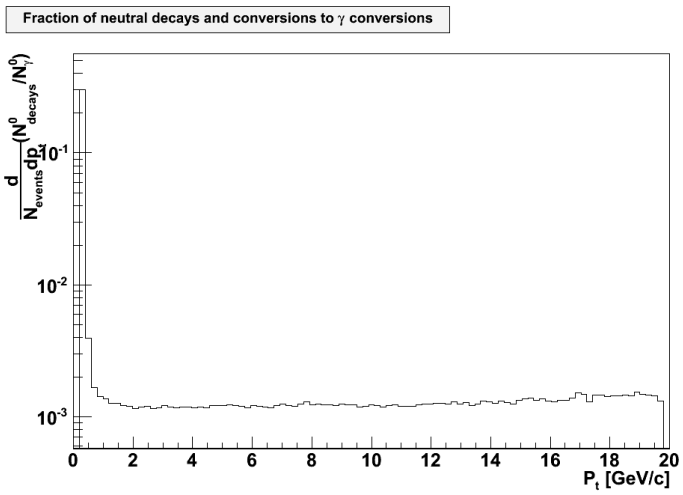

Figure 6.22: Figure showing the average ratio of all neutral particle decays to all *detectable* γ *conversions*, found by the *V0-Finder* with cut set Nr.9 with **HLT** tracks as input, for one-hundred-thousand γ embedded minimum bias p-p events at $\sqrt{s} = 14\ TeV$ per nucleon pair. A neutral particle decay is here defined as a neutral particle that decays to two oppositely charged particles, i.e., $X \rightarrow y^- + y^+$.

could potentially help eliminate portions of this contribution as well. The neutral decays that are most significant with respect to the contamination are $K^0_S \rightarrow \pi^+\pi^-$, $\Lambda \rightarrow p\pi^-$, and $\bar{\Lambda} \rightarrow \bar{p}\pi^+$ [53]. A dE/dx measurement performed with the TPC during off-line reconstruction, and obtained from [55], is shown in figure 6.23 (a).

The possibilities of an on-line dE/dx calculation is currently being investigated by MS.c. Per Ivar Lønne (UiB, Norway) and Ph.D Alexander Kalweit (GSI, Germany). However, the speed of the algorithm is currently deemed insufficient to be efficiently run *on-line* during data-taking. Efforts, largely performed by the aforementioned persons, are currently underway to increase the speed of the dE/dx algorithm, and as it progresses its addition to HLT's *V0-Finder* should be considered as a possible upgrade, provided sufficient processing times. The observed ratio of all neutral particle decays, correctly reconstructed by HLT's *V0-Finder* with cut set Nr.9, to the number of *detectable* γ *conversions* found by the *V0-Finder* is shown in figure 6.22.

In addition, an investigation into the prospects of including a q_t cut to HLT's *V0-Finder* analogous to the Armenteros-Podolanski cuts used by off-line could be performed. However, *off-line* analysis of *off-line's V0-Finder* found that a cut on q_t could effectively cut away the high-p_t γs if the cut-value was based purely on the Armenteros-Podolanski plots, where the currently use a cut off at $q_t \approx 1\ GeV/c$. Care should be taken to ensure

that a minimal amount of high-p_t photons are removed from the V0-sample, if this cut is to be added to HLT's *V0-Finder*. The Armenteros-Podolanski plots for the off-line V0 sample, before and after the off-line V0-cuts, are shown in figures 6.23 (b) and (c). As always, the benefits of additional cuts should to be weighed against its possible drawbacks, either in a reduced efficiency or purity, or a resulting inadequate processing time.

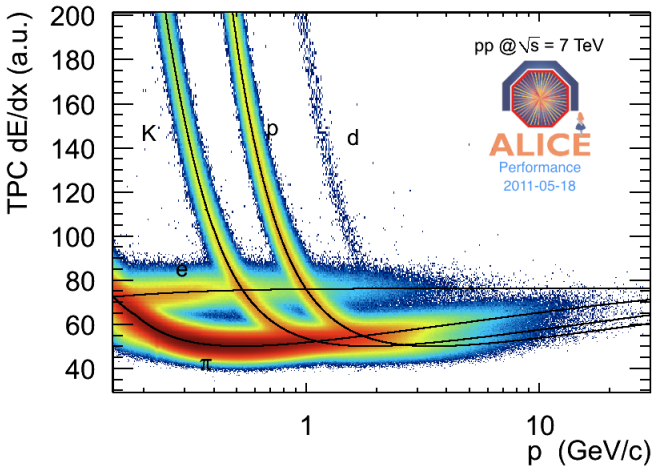

(a) TPC Offline dE/dx

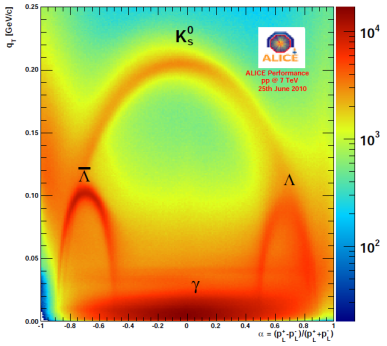

(b) Before application of cuts

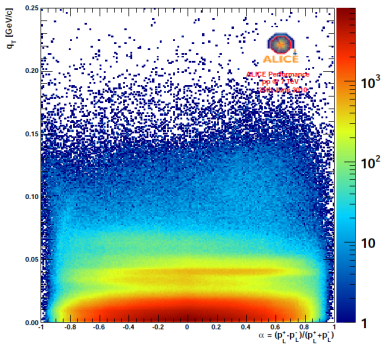

(c) After application of cuts

Figure 6.23: The figures show TPC dE/dx measurement and the Armenteros-Podolanski plots of the off-line V0 sample from real p-p collisions at $\sqrt{s} = 7\ TeV$ per nucleon pair. From the figure we can see that different particles occupy the different regions in the p_t-α plot. Figures show: (c) dE/dx from TPC off-line, figure was taken from [55] (b) The Armenteros-Podolanski plot of the V0-sample before any cuts are applied, (c) The Armenteros-Podolanski plot of the V0-sample after the cuts have been applied, where we see a large contribution from the non-γs has been reduced. The figure were taken from [53].

V0-Finder efficiency and purity for cut set Nr.9: **HLT tracks**		
100 000 Min. bias. p-p embedded γs events		
Cut set	Average efficiency	Average purity
Nr.9	(41.71 ± 0.01) %	(74.02 ± 0.09) %

(a)

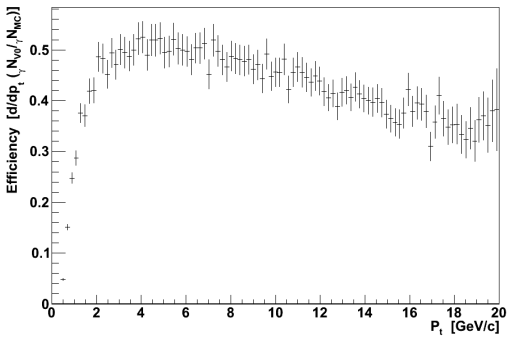

(b) Efficiency vs. p_t

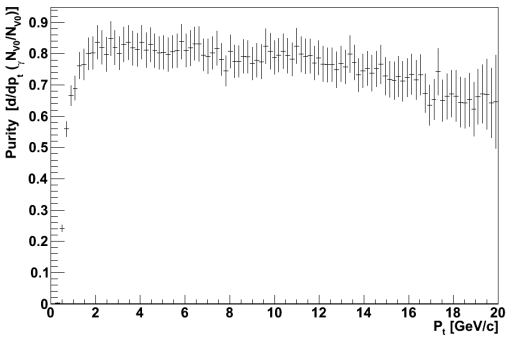

(c) Purity vs. p_t

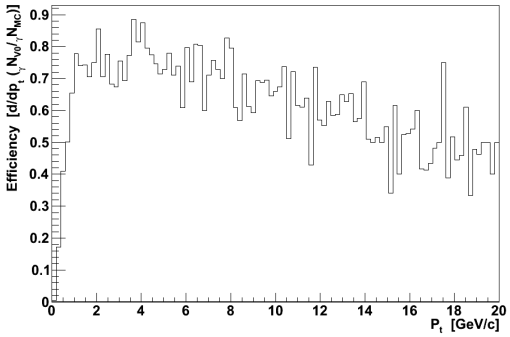

(d) Efficiency vs. p_t

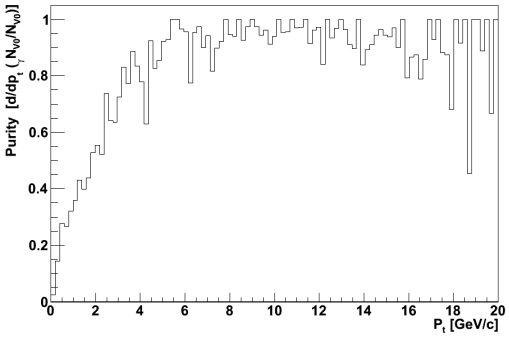

(e) Purity vs. p_t

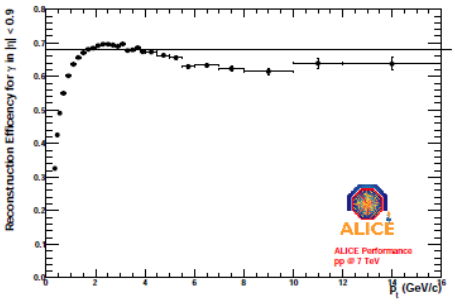

(f) Efficiency vs. p_t

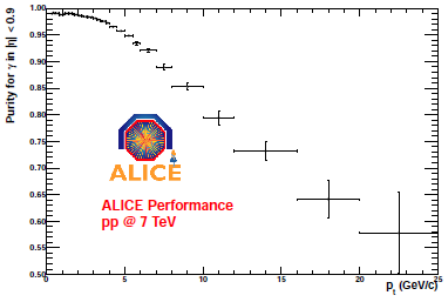

(g) Purity vs. p_t

Figure 6.24: The figure summarize the results obtained with HLT's *V0-Finder* compared along side the results of off-lines V0-Finder after processing real events. Table (a) lists the optimal average efficiency and purity, in p_t range of [0, 20] GeV/c, with HLT tracks as input, figures (b) and (c) show the efficiency and purity for HLT's *V0-Finder* using HLT tracks as input, (d) and (e) depict the result from processing off-line tracks with the HLT *V0-Finder*, (f) and (g) show the optimal efficiency and purity of the off-line *V0-Finder* using off-line tracks as input.

Chapter 7

Summary and outlook

The LHC is designed to collide particles and nuclei at record high C.M. energies, $\sqrt{s} = 5.5\ TeV$ per nucleon pair for Pb-Pb and $\sqrt{s} = 14\ TeV$ per nucleon pair for p-p. ALICE, one of the experiments operating in conjunction with the LHC, is concerned with studying the characteristics of the state of nuclear matter formed at these ultra-relativistic energies. As described in section 2.1, photons may be used as probes to indicate the formation of a QGP after equilibrium, as the mean free path of the γs are substantially larger than the diameter of the medium. However, since the measured inclusive γ spectra is comprised of both the direct γ yield along with a substantial background produced from neutral meson decays, it is important to map the contribution from the mesons in order to subtract it from the inclusive yield.

The goal of this work and analysis was to map the capabilities of the ALICE HLT *V0-Finder*, in the application for the detection and reconstruction of γ conversions within the ITS and TPC. Further, the existing cuts were optimized, and additional cuts were added in order to produce a sample of γ conversion candidates with a high efficiency and purity.

All of the result pertaining to HLT's V0-Finder presented in this thesis were obtained from processing simulated events, with the use of the Monte Carlo information. We observed an average efficiency and purity, determined in a p_t range of [0, 20] GeV/c, of 41.70 % and 74.02 % respectively, for a data set of one-hundred-thousand γ embedded minimum bias p-p collisions at $\sqrt{s} = 14\ TeV$ per nucleon pair. The effects of a potential p_t cut has been explored, though currently not included in the *V0-Finder*, and the resulting average values for the efficiency and purity, determined in a range of [p_t-*cut*, 20] GeV/c has been displayed in section 6.5.1. As described in section 6.5.4, a future improvement to the *V0-Finder* could be the addition of a dE/dx cut, which should result in a higher purity. Though, the addition of such a cut is contingent on the obtainable speed of the dE/dx algorithm for HLT.

As noted, the act of embedding γs could lead to a measurement of the

efficiency and purity reflecting a falsely low number, compared to what it may have in non-embedded or real events at the same energy. Therefore, the next step in mapping the capabilities of the *V0-Finder* should be to run over a large sample of real data recorded by ALICE. Preparation has begun in the process of running the *V0-Finder* with real data.

The on-line γ conversion trigger will link to the CTP through an instance of the *V0-Finder*, which will load the values of the optimized cuts through an OCDB object. A conditional *if-statement* has been added to the *V0-Finder* around the decay length cut. This allows the *V0-Finder* to skip the calculation of the decay length, if configured for the γ conversion application, and thereby reduces the processing time of the *V0-Finder*. The use of OCDB objects allows the CTP to configure the *V0-Finder* according to its trigger menu without the need to alter or recompile the C++ code for the potential various applications, e.g., $\gamma \to e^- e^+$, $K^0_S \to \pi^+\pi^-$, $\Lambda \to p\pi^-$, and $\bar{\Lambda} \to \bar{p}\pi^+$. In addition, the γ trigger will enrich the high-p_t π^0 sample, needed for the subtraction of background from the measured inclusive photon spectra.

Bibliography

[1] K. Nakamura and S. T. Petco. Neutrino mass, mixing, and oscillations. `http://pdg.lbl.gov/2010/reviews/rpp2010-rev-neutrino-mixing.pdf`, 2010. [Online, accesed 01-February-2011].

[2] `http://pdg.lbl.gov`, 2010. [Online; accessed 04-February-2011].

[3] K. Yagi, T. Hatsuda, and Y. Miake. *Quark-Gluon Plasma*. Cambridge University Press, 1st edition, 2008.

[4] The CBM Experiment. The CBM Experiment. `http://www.gsi.de/forschung/fair_experiments/CBM/1intro_e.html`, 2010. [Online; accessed 31-January-2011].

[5] B. Müller and J. L. Nagle. Results from the Relativistic Heavy Ion Collider. *Ann. Rev. Nucl. Part. Sci., 56:93–135*, 2006. [Online, accesed 08-March-2011].

[6] K. Aamodt et al. Elliptic Flow of Charged Particles in Pb-Pb Collisions at $\sqrt{s_{NN}} = 2.76\ TeV$. *Phys. Rev. Lett.*, 105:252302, 2010. [Online; accessed 8-March-2011].

[7] K. Aamodt et al. Suppression of charged particle production at large transverse momentum in central Pb-Pb collisions at $\sqrt{S_{NN}} = 2.76\,TeV$. *Phys. Lett. B*, 696:30–39, 2011.

[8] B. I. Abelev et al. Enhanced strange baryon production in Au+Au collisions compared to $p + p$ at $\sqrt{s_{NN}} = 200$ GeV. *Phys. Rev. C*, 77:044908, 2008.

[9] J. Adams et al. Evidence from d + Au Measurements for Final-State Suppression of High-p_T Hadrons in Au + Au Collisions at RHIC. *Phys. Rev. Lett.*, 91:072304, 2003. [Online; accessed 8-March-2011].

[10] F. Carminati et. al. ALICE: Physics Performance Report, Volume I. *J. Phys. G: Nucl. Part. Phys., 30:1517-1763*, 2004.

[11] T. Peitzmann and M. H. Thoma. Direct photons from relativistic heavy-ion collisions. *Physics Reports*, 2002. 364:175-246.

[12] S. T. R. Rapp and C. Gale. Hadronic production of thermal photons. *Phys. Rev. C*, 69:014903, 2004. [Online; accessed 8-March-2011].

[13] G. Cones et al. Direct photon detection in PbPb collisions in the ALICE experiment at LHC. *Nucl. Phys. A*, 782:356c–361c, 2007.

[14] P. Stankus. Direct Photon Production in Realativistic Heavy-Ion Collisions. *Ann. Rev. Nucl. Part. Sci.*, 55:517–554, 2005.

[15] M. M. Aggarwal. Direct Photon Production in 158 A GeV ^{208}Pb+^{208}Pb collisions. *arXiv:nucl-ex/0006007v2*, 2000. [Online; accessed 23-March-2011].

[16] S. Adler et al. Centrality Dependence of Direct Photon Production in $\sqrt{S_{NN}} = 200\ GeV$ Au+Au Collisions. *Phys. Rev. Lett.*, 94:232301, 2005.

[17] J. Frantz. Illuminating RHIC matter with the multi-pupose direct photon. *J. Phys. G: Nucl. Part. Phys.*, 34:S389–S396, 2007.

[18] W. R. Leo. *Techniques for nuclear and particle physics experiments.* Springer-Verlag, 2nd edition, 1997.

[19] J. J. Hubbel et al. Pair, Triplet, and Total Atomic Cross Sections (and Mass Attenuation Coefficients) for 1 MeV–100 GeV Photons in Elements Z = 1 to 100. *J. Phys. Chem. Ref. Data*, vol 9, No.4, 1980.

[20] K. Aamodt et. al. The ALICE experiment at the CERN LHC. *JINST 3 S08002*, 2008.

[21] ATLAS detector and physics performance : Technical Design Report. Technical report, 1999. CERN-LHCC-99-015, vol.2.

[22] The CMS muon project : Technical Design Report. Technical report, 1997. CERN-LHCC-97-032.

[23] P. Perret. Status and expected performance of the LHCb experiment. *Nucl. Phys. B, 142:442-447*, 2005.

[24] The LHCf collaboration. LHCf experiment : Technical Design Report. Technical report, 2006. CERN-LHCC-2006-004.

[25] F. Ferro. TOTEM physics. *Nucl. Phys. B - Proc. Suppl., 146:39-43*, 2005.

[26] Syracuse University Experimental High Energy Physics. How a particle accelerator and detector work. `http://hepoutreach.syr.edu/Index/accelerator_science/accel_overview.html`, 2007. [Online; accessed 17-March-2011].

[27] R. Assmann et. al. Measurement of the relative luminosity at the LHC, 2003. [Online; accessed 21-February-2011].

[28] J. M. Jowett, R. Bruce, and S. Gilardoni. Luminosity Limit from bound-free pair production in the LHC, 2005. [Online; accessed 21-February-2011].

[29] LHC Programme Coordination web pages : LHC lumi plots. `http://lpc.web.cern.ch/lpc/`, 2011. [Online; accessed 28-May-2011].

[30] K. Aamodt et. al. Charged-Particle Multiplicity Density at Midrapidity in Central Pb-Pb Collisions at $\sqrt{S_{NN}} = 2.76$ TeV. *Phys. Rev. Lett.*, 105(25):252301, 2010.

[31] G. De Cataldo. Performance of the High Momentum Particle Identification Detector in ALICE at LHC. [Online; accessed 21-February-2011].

[32] The ALICE Collaboration. ALICE inner tracking system : Technical Design Report. Technical report, 1999. CERN-LHCC-99-12.

[33] The ALICE collaboration. ALICE time projection chamber : Technical Design Report. Technical report, 2000. CERN-LHCC-2000-001.

[34] `http://blogs.uslhc.us/tag/alice`, 2010. [Online; accessed 01-February-2011].

[35] J. Baechler. The ALICE TPC. `http://villaolmo.mib.infn.it/ICATPP9th_2005/Advanced,%20Miniaturized%20Detectors%20and%20Particle%20Identification/`. [Online; accessed 7-April-2011].

[36] T. Anticic et. al. Commissioning of the ALICE Data Acquisition system. *J. Phys.: Conf. Ser., 119, 022006*, 2008.

[37] F. Costa et. al. Readout upgrade, hardware and software, for the ALICE Data Acquisition program. *Nucl. Instr. Meth. Phys. Res. A, 617:258-259*, 2010.

[38] M. Richter. DAQ bandwidth capabilities. Stated in the HLT-workshop held at Oslo,Norway, in February-2011.

[39] M. Richter. HLT hardware inventory. Personal correspondence.

[40] The ALICE Technical design report of the Trigger, Data Acquistion, High-Level Trigger and Control System. Technical report, 2004. CERN-LHCC-2003-062.

[41] http://g4education.kek.jp/pages/viewpage.action?pageId=1605905&showComments=true&showCommentArea=true, 2009. [Online; accessed 04-February-2011].

[42] K. Kleinknecht. *Detectors for particle radiation.* Cambridge university press, 2nd edition, 1998.

[43] N. W. Ashcroft and N. D. Mermin. *Solid State Physics.* Brooks/Cole, Cengage Learning, 1st edition, 1976.

[44] CMS inner tacker. http://www.hephy.at/index.php?id=750&L=1. [Online; accessed 10-April-2011].

[45] Double-sided silicon strip detector for x-ray imaging. http://spie.org/x20060.xml?ArticleID=x20060. [Online; accessed 10-April-2011].

[46] A. Breskin et al. High-accuracy, bidimensional read-out of proportional chambers with short resolution times. *Nuclear Instruments and Methods, Vol 143 nr.1, pages 29–39*, 1977.

[47] The ALICE Offline Bible. http://aliceinfo.cern.ch/Offline/AliRoot/Manual.html, 2007. [Online; accessed 18-April-2011].

[48] T. Sjöstrand, S. Mrenna, and P. Skands. PYTHIA 6.4 physics and manual. *JHEP*, 2006(05):026, 2006.

[49] S. Gorbunov. ALICE HLT High Speed Tracking and Vertexing. Presentation at Real-time 2010 Conference, Lisboa, May.25 2010.

[50] S. Gorbunov, M. Kretz, and D. Rohr. Fast Cellular Automaton tracker for the ALICE High Level Trigger. *GSI Scientific Report 2009 (GSI Report 2010-1)*, 2010. [Online; accessed 20-April-2011].

[51] H. K. F. Bjerke. Technical report: Efficient parallel tracking. *CERN openlab*, 2009. [Online; accessed 20-April-2011].

[52] K. Aamodt et. al. Analysis Note: π^0 and η meson measurement with conversions in ALICE in proton-proton collisions at $\sqrt{s} = 7\ TeV$, $\sqrt{s} = 2.76\ TeV$ and at $\sqrt{s} = 900\ GeV$ at the CERN LHC. Accessed online May 27, 2011, direct link: https://twiki.cern.ch/twiki/pub/ALICE/PWG4PhotonsAndJets/aliceNoteMesonConv$_$v$1.1.$pdf.

[53] K. Aamodt. *Photon, π^0 and η measurements in proton-proton collisions at $\sqrt{s} = 7\ TeV$ with the ALICE TPC at the LHC.* PhD thesis, Institute for Physics and Technology, University in Bergen, Norway, April 2011.

[54] K. Aamodt et al. Analysis Note: Measurement of Direct Photons in pp Collisions at the LHC with ALICE at $\sqrt{s} = 7\ TeV$ via Conversions. Accessed online May 27, 2011, through figure note: `https://aliceinfo.cern.ch/Figure/node/1212`.

[55] ALICE Collaboration. Alice figure repository: Performance figures, 2011. `https://aliceinfo.cern.ch/Figure/`.